Seismic Source and Attenuation Studies in the Central and Eastern United States

Qimin Wu

Dissertation submitted to the Faculty of the
Virginia Polytechnic Institute and State University
in partial fulfillment of the requirements for the degree of

Doctor of Philosophy
in
Geosciences

Martin C. Chapman, Chair
John A. Hole
Erik C. Westman
Ying Zhou

May 1, 2017
Blacksburg, Virginia

Keywords: Virginia aftershocks, geometrical spreading, induced earthquakes, stress drop

Seismic Source and Attenuation Studies in the Central and Eastern United States

Qimin Wu

ABSTRACT

To better understand the ground motion and associated seismic hazard of earthquakes in the central and eastern United States (CEUS), this dissertation focuses on the source parameters and wave propagation characteristics of both tectonic earthquakes and induced earthquakes in the CEUS. The infrequent occurrence of significant earthquakes in the CEUS limits the necessary observations needed to understand earthquake processes and to reduce uncertainty in seismic-hazard maps. The well-recored aftershock sequence of the 2011 Mineral, Virginia, earthquake offers a rare opportunity to improve our understanding of earthquake processes and earthquake hazard in this populous region of the United States. Moreover, the rapid increase of seismicity in the CEUS since 2009 that has been linked to wastewater injection has raised concern regarding the potential hazard. In this dissertation, I first present a detailed study of the aftershock sequence of the 2011 Mw 5.7 Mineral, Virginia earthquake. It involves the hypocenter locations of ~3000 earthquakes, ~400 focal mechanism solutions, statistics of the aftershock sequence, and the Coulomb stress modeling that explains the triggering mechnanism of those aftershocks. Second, I examine the S-wave attenuation at critical short hypocentral distances (< 60 km) using the aftershock data. The observed S-wave amplitudes decay as a function of hypocenter distance R according to $\sim R^{-1.3} - R^{-1.5}$, which is substantially steeper than R^{-1} for a homogeneous whole space. Finally, I propose and apply a stable multi-window coda spectral ratio method to estimate corner frequencies and Brune-type stress drops for the 2011 Mineral, Virginia mainshock and aftershocks, as well as induced earthquakes in Oklahoma. The goal of this comparative study is to find out whether or not there are systematical differences in source parameters between tectonic earthquakes and induced earthquakes in the CEUS. I found generally much higher stress drops for the Mineral, Virginia sequence. However, the stress drops for those induced earthquakes in Oklahoma exhibit large varation among individual earthquake sequences, with the large mainshocks having high stress drops (20-30 MPa, Brune-type) except for the 2011 Mw 5.6 Prague, Oklahoma earthquake. And spatially varying stress drops indicates strong fault heterogeneity, which in the case of induced earthquakes may be influenced by the injection of fluids into the subsurface.

Seismic Source and Attenuation Studies in the Central and Eastern United States

Qimin Wu

GENERAL AUDIENCE ABSTRACT

This dissertation aims to improve our understanding of seismic hazard associated with both tectonic earthquakes and induced earthquakes in the central and eastern United States (CEUS) by studying the source parameters and wave propagation characteristics of earthquakes in the CEUS. The infrequent occurrence of significant earthquakes in the CEUS limits the necessary observations needed to understand earthquake processes and to reduce uncertainty in seismic-hazard maps. The well-recored aftershock sequence of the 2011 Mineral, Virginia, earthquake offers a rare opportunity to improve our understanding of earthquake processes and earthquake hazard in this populous region of the United States. Moreover, the rapid increase of seismicity in the CEUS since 2009 that has been linked to wastewater injection has raised concern regarding the potential hazard. In this dissertation, I first present a detailed study of the aftershock sequence of the 2011 Mw 5.7 Mineral, Virginia earthquake. It involves the estimation of various types of source parameters. Second, I examine the S-wave attenuation at critical short hypocentral distances (< 60 km) using the aftershock data. The oberved ground-motion amplitude decay with distance can be incorporated in ground motion prediction models for the region. Finally, I propose and apply a new method to estimate precise corner frequencies and Brune-type stress drops, which are two important source parameters, for the 2011 Mineral, Virginia mainshock and aftershocks, as well as induced earthquakes in Oklahoma. The goal of this comparative study is to find out whether or not there are systematical differences in source parameters between tectonic earthquakes and induced earthquakes in the CEUS. The results shed light on the associated seismic hazard as well as the triggering mechanism for both tectonic earthquakes and induced earthquakes in the CEUS.

Acknowledgments

First and foremost, I want to thank my advisor Dr. Martin Chapman. I am very grateful for the opportunity to work with him for my Ph.D. Martin is a very respectable mentor and friend who always has an open door for discussing research and for sharing his ideas on all kinds of problems, from science to culture, history and even politics. I probably spent more time in his office than in my own over the years. I very much appreciate all the opportunities Martin provided me to attend scientific conferences and establish myself in the seismological community. It has been such an enjoyable journey to work with you. Thanks for everything, Martin!

I am also grateful to the other members of my committee. I thank Dr. John Hole for all his interest and support in my research from the beginning. I thank Dr. Ying Zhou and Dr. Erik Westman for making time for me in their busy schedules and for teaching me how to critically challenge my research.

Special thanks go to Jake Beale and Arthur Snoke. Jake has always been a helpful collaborator and friend since I joined the Virginia Tech Seismological Observatory (VTSO) in spring, 2013. Arthur provided me with a lot of constructive comments and suggestions on my papers and presentations. And I benefit a lot from the package FOCMEC he developed in my research.

I feel fortunate for all the great people I have met here in the Department of Geosciences at Virginia Tech. I want to thank my fellow graduate students Roberto Marivela-Colmenarejo, Didem Beskardes, Amir Zainali and Kannikha Kolandaivelu for the great time we spent together and for all their emotional support. A big thanks goes to many other friends: Zhen Guo, Liang Han, Kui Liu, Wei Cheng, Xu Ma, Tahiry Rajaonarison, Joe Cochran, just to mention a few. You all made my time at Virginia Tech a delight!

I would also like to thank our administrative staffs Connie Lowe, Mary McMurray, Jo Thomason for their continuous help and support, and Mark Lemon and James Dunson for their technical support in the past years.

I would like to express my heart-felt gratitude to my family who have always been there for me, although we had such a long distance between us. My mom and dad always supported me in fulfilling my dreams. I thank my brother for taking care of our parents when I was away. Last, but far from least, I want to express my deep appreciation and love for my girlfriend, Junjun Liu. She has always been there with patience and support in difficult times. I cannot imagine that I could have completed this work without her support and love.

Contents

List of Figures

List of Tables

Chapter 1

Introduction

1.1 Background and Motivations

Seismic hazard is less well understood in the eastern United States (EUS) compared to the western United States (WUS) due to the fact that seismic activity is generally low, large earthquakes are infrequent and station coverage is sparse. However, earthquakes in the central United States (CUS) and EUS are typically felt, and cause damage over a much broader region than equivalent events in the United States west of the Rocky Mountains. Because of the lack of observational data for earthquakes in the EUS, most current ground motion prediction models for eastern North America (ENA) are based to some degree on the stochastic model (Boore, 1983; Atkinson and Boore, 1995; Boore, 2003, Atkinson and Boore, 2006). The target ground acceleration spectrum in the stochastic model is comprised of three main components: the source spectrum, the path effect, and the site response. The reliability of these simulation methods depends on the accuracy of the earthquake source model, wave propagation parameters, and the site effects. Therefore, it is critical to study those three aspects in the EUS to improve our understanding of seismic hazard in the region. The source parameters involve precise determinations of earthquake location, magnitude, focal mechanism and stress drop, etc. The path effect involves two physical processes: geometrical spreading of the S waves and the Lg group and frequency-dependent attenuation due to anelastic absorption and/or scattering. At near-source distances, the path effect is mostly dominated by geometrical spreading, whereas anelastic attenuation becomes important at larger distances and at higher frequencies. And the site effects, mainly attributed to the near-surface geological complexity, affect the ground motion significantly through amplification/deamplification.

The 23 August 2011 Mw 5.7 earthquake in central Virginia was felt over most of the eastern seaboard of the United States. It caused modified Mercalli intensity (MMI) VIII damage near the epicenter in Louisa County, Virginia. Instances of significant damage occurred as far away as Washington D.C. Taber (1913) noted a long history of seismicity in central Virginia. Bollinger (1969, 1973a,b) recognized a central Virginia seismic zone in the Virginia Piedmont geologic province lying within approximately 60 km of the James River, between Charlottesville on the west, and Richmond on the east. This earthquake distinguishes itself as one of the most widely felt earthquakes in United States history. The large felt area reported by the USGS Did You Feel It? (DYFI) system (Wald et al., 2011) is roughly 10 times the area of a similarly sized earthquake in the western United States (Horton and Williams, 2012). The felt area extends northsouth from central Georgia to southeast Canada and west to Detroit, Michigan, and Chicago, Illinois. Strong shaking from the earthquake caused significant damage to homes and permanently closed two schools in the epicentral area. In addition, the North Anna nuclear power station shut down due to high recorded accelerations at the plant and remained closed for 2.5 months. A strong-motion accelerometer at the North Anna nuclear power plant recorded the closest instrumental ground motions of the earthquake, in which the maximum horizontal acceleration reached 0.27g(Chapman, 2013). This is the first known case in which an operating nuclear power plant in the United States was closed in response to an earthquake (Horton and Williams, 2012).

The infrequent occurrence of significant earthquakes in the EUS limits the necessary observations needed to understand earthquake processes and to reduce uncertainty in seismic-hazard maps. For these reasons, characterizing the aftershock sequence of the 2011 Mineral, Virginia, earthquake offers a rare opportunity to improve our understanding of earthquake

processes and earthquake hazard in this populous region of the United States.

In the CUS, the sharp increase in seismicity over a broad region since 2009 has raised concern regarding the source of the activity and its potential hazard to local communities and energy industry infrastructure. Those earthquakes, involving 4 Mw 5+ earthquakes since 2011, have been linked to wastewater injection. During 2011, an Mw 5.6 earthquake near Prague, Oklahoma caused damage to several schools and other structures (Petersen et al., 2016). In Oklahoma, during 2016, the 13 February Mw 5.1 earthquake near Fairview, the 3 September Mw 5.8 earthquake near Pawnee, and the 7 November Mw 5.0 earthquake near Cushing caused damaging ground shaking. Those damaging events are thought to be the result of wastewater injection, and the potential for future large earthquakes causes concern for officials responsible for public safety and welfare.

To understand the ground motion and associated seismic hazard of those induced earthquakes, studies are currently focusing on the source parameters and wave propagation characteristics of those earthquakes. However, it remains difficult to discriminate between induced and natural earthquakes. Evidences such as proximity to injection wells, correlation between production/injection activities and seismicity are used for evaluating the likelihood of earthquakes being induced (David and Frohlich, 1993; Frohlich et al., 2016). Some previous studies suggest that source parameters, such as stress drops, may provide more direct evidence of induced earthquakes (Goertz-Allman et al., 2011; Chen and Shearer, 2011; 2013; Sumy et al., 2017).

1.2 Outline of Thesis Chapters

This dissertation is organized as follows:

- In Chapter 2, I present a comprehensive investigation of the aftershock sequence of the 2011 Mw 5.7 Mineral, Virginia earthquake. It involves the hypocenter locations of ~3000 earthquakes, hundreds of focal mechanism solutions, statistics of the aftershock sequence, and the Coulomb stress modeling that explains the triggering mechnanism of those aftershocks.

- In Chapter 3, I examine the S-wave attenuation at critical short hypocentral distances (< 60 km) in the CVSZ using the aftershocks of the 2011 Virginia earthquake. The coda-normalization method is applied to account for the earthquake source and recording site response.The observed S-wave amplitudes decay as a function of hypocenter distance R according to $R^{-1.51}$, $R^{-1.51}$, and $R^{-1.45}$ for radial, transverse and vertical component motion, respectively. Frequency-dependent attenuation effects are found to be marginally significant in the data examined. With assumed Q models, the apparent geometrical spreading coefficients γ are determined to be in the range of 1.37-1.46, 1.37-1.46 and 1.30-1.40 for radial, transverse and vertical component, respectively, which are substantially steeper than R^{-1} for a homogeneous whole space.

- In Chapters 4 and 5, I propose a multi-window coda spectral ratio method to estimate stable and reliable corner frequencies and stress drops for the 2011 Mineral, Virginia mainshock and aftershocks, as well as induced earthquakes in Oklahoma. The goal is to find out whether or not there are systematical differences in source parameters

between tectonic earthquakes and induced earthquakes in the CEUS. I found generally much higher stress drops for the Mineral, Virginia sequence. However, the stress drops for those induced earthquakes in Oklahoma exhibit large varation among individual earthquake sequences, with the large mainshocks having high stress drops (20-30 MPa) except for the 2011 Mw 5.6 Prague, Oklahoma earthquake. And spatially varying stress drops indicates strong fault heterogeneity, which in the case of induced earthquakes may be influenced by the injection of fluids into the subsurface.

References

Atkinson, G. M. and D. M. Boore (1995). New ground motion relations for eastern North America, *Bull. Seismol. Soc. Am.* **85**, 17-30.

Atkinson, G. M. and D. M. Boore (2006). Earthquake ground motion prediction equations for eastern North America, *Bull. Seismol. Soc. Am.* **96**, 2181-2205.

Bollinger, G. A. (1969). Seismicity of the central Appalachian states of Virginia, West Virginia, and Maryland 1758 through 1968, *Bull. Seismol. Soc. Am.* **59**, 2103-2111.

Bollinger, G. A. (1973a). Seismicity and crustal uplift in the southeastern United States, *Am. J. Sci.* **273-A**, 396-408.

Bollinger, G. A. (1973b). Seismicity of the southeastern United States, *Bull. Seismol. Soc. Am.* **63**, 1785-1808.

Boore, D. M. (1983). Stochastic simulation of high-frequency ground motions based on seismological models of the radiated spectra, *Bull. Seismol. Soc. Am.* **73**, 1865-1894.

Boore, D. M. (2003). Prediction of ground motion using the stochastic method, *Pure Appl. Geophys.* **160**, 635-676.

Chapman, M. C. (2013). On the rupture process of the 23 August 2011 Virginia earthquake, *Bull. Seismol. Soc. Am.* **103**, 613-628.

Horton, J. W., and R. A. Williams (2012). The 2011 Virginia earthquake: What are scientists learning? *Eos Trans. AGU* **93**, 33.

Taber, S. (1913). Earthquakes in Buckingham county, Virginia, *Bull. Seismol. Soc. Am.* **3**, 124-133.

Wald, D. J., V. Quitoriano, C. B. Worden, M. Hopper, and J. W. Dewey (2011). USGS Did You Feel It? Internet-based macroseismic inten- sity maps, *Ann. Geophys.* **54**, 6.

Chapter 2

The Aftershock Sequence of the 2011 Mineral, Virginia, Earthquake[†]

[†]**Citation: Wu, Q.**, M. C. Chapman and J. N. Beale (2015). The Aftershock Sequence of the 2011 Mineral, Virginia, Earthquake: Temporal and Spatial Distribution, Focal Mechanisms, Regional Stress and the Role of Coulomb Stress Transfer, *Bull. Seismol. Soc. Am.* **105**, 2521-2537.

Abstract

The aftershocks of the M_W 5.7, 23 August, 2011 Mineral, Virginia, earthquake were recorded by 36 temporary stations installed by several institutions. We located 3,960 aftershocks from 25 August, 2011 through 31 December, 2011. A subset of 1,666 aftershocks resolves details of the hypocenter distribution. We determined 393 focal mechanism solutions. Aftershocks near the mainshock define a previously recognized tabular cluster with orientation similar to a mainshock nodal plane; other aftershocks occurred 10-20 km to the northeast. A large percentage of the aftershocks occurred in regions of positive Coulomb static stress change and approximately 80% of the focal mechanism nodal planes were brought closer to failure. However, the aftershock distribution near the mainshock appears to have been influenced strongly by rupture directivity. Aftershocks at depths less than 4 km exhibit reverse mechanisms with N-NW trending nodal planes. Most focal mechanisms at depths greater than 6 km are similar to the mainshock, with N-NE trending nodal planes. A concentration of aftershocks in the 4-6 km depth range near the mainshock are mostly of reverse type, but display a 90-degree range of nodal plane trend. Those events appear to outline the periphery of mainshock rupture, where positive Coulomb stress transfer is largest. The focal mechanisms of aftershocks at depths less than 4 km and those at depths greater than 6, along with the mainshock, point to the possibility of a depth-dependent stress field prior to the occurrence of the mainshock. Analysis of earthquake occurrence using a new magnitude scale ($M_d{}^*$) indicates a Gutenberg-Richer law b-value of 0.864 and an Omori law p-value of 1.085, indicative of a typical aftershock sequence.

2.1 Introduction

The Mineral, Virginia, earthquake occurred at 17:51:3.9 UTC on 23 August, 2011, with epicenter at 37.905°N, 77.975°W and focal depth 8 km (Chapman, 2013). It caused structural damage consistent with level VIII of the modified Mercalli intensity scale near the epicenter in Louisa County, Virginia, and significant damage as far away as Washington, D.C. (Horton et al., 2015a; Heller and Carter, 2015; Wells et al., 2015). The USGS/St. Louis University moment tensor solution (Herrmann, 2011) indicates moment magnitude Mw 5.65, and a nodal plane with strike N28°E, dip 50°and rake 113°, in agreement with aftershock locations (Herrmann, 2011; Chapman, 2013; McNamara et al., 2014; Horton et al., 2015b). This reverse-fault earthquake occurred in an area known as the central Virginia seismic zone (CVSZ), which has a long history of moderate earthquake activity (Taber, 1913; Bollinger, 1969, 1973a, 1973b; Kim and Chapman, 2005; Chapman, 2013; Chapman, 2015; Horton et al., 2015a, and references therein). The earliest earthquake reported in the central Virginia seismic zone occurred on February 21, 1774. The earthquake displaced houses considerably off their foundations at Blandford and Petersburg, according to Stover and Coffman (1993).

The mainshock was a complex rupture comprised of multiple subevents in a small fault area centered at depths between approximately 6.0 and 8.0 km (Chapman, 2013; Hartzell et. al., 2013, Motazedian and Ma, 2014). Previous studies found that the early aftershocks occurred mostly within a tabular zone exhibiting strike and dip similar to a main shock focal mechanism nodal plane (Herrmann, 2011; Chapman, 2013; McNamara et al., 2014; Wu et al., 2014; Horton et al., 2015b). Previous studies also identified some aftershocks approximately 10-20 km to the east and northeast of the mainshock that were interpreted to be triggered by

stress transfer due to the mainshock (McNamara et al., 2014; Wu et al., 2014; Horton et al., 2015b). The previously determined regional moment tensor (RMT) solutions for 16 of the largest aftershocks show a diversity of nodal plane orientation, although most of them are of reverse type (Herrmann, 2011; McNamara et al., 2014). The geologic structure of the study area is dominated by low-angle thin-skinned thrusting during the late Paleozoic (Horton et al, 2015a). The earthquakes occur within allochthonous crystalline rocks of Paleozoic age, above the basal Appalachian detachment inferred at a depth of approximately 12 km from seismic reflection profiles in the area (Pratt et al., 1988, Pratt et al, 2015, Bollinger et al., 1991). The area was subjected to extensional tectonics during the early Mesozoic and there are several Mesozoic extensional basins in the central Virginia area (Culpeper, Farmville, Scottsville, and Richmond basins). The Mineral earthquake and its aftershocks do not appear to be simple reactivation of known Paleozoic thrust faults or a Mesozoic basin boundary faults (Pratt et al., 2015).

Here, we describe a study of the aftershock sequence of the Mineral earthquake using a larger data set than was used previously. The purpose was to better understand the nature of faulting in the area, in particular, the stress regime driving the still on-going (early 2015) aftershock activity. We focused on details of the hypocenter locations of thousands of aftershocks, focal mechanisms of several hundred aftershocks, and the dominant role that stress transfer appears to play in the aftershock process of the Mineral earthquake. Presumably, the aftershock process of this event is representative of other moderate to large shocks that have occurred and will occur in eastern North America, and a better understanding of the Mineral event could shed more light on the state of stress in intraplate North America.

The analysis steps involved first a thorough detection of the aftershocks using data recorded by the temporary stations deployed subsequent to the mainshock. Then we determined single-event hypocenter locations using both P- and S-wave arrival times. Subsequently, most of the events were relocated using the double-difference algorithm HypoDD (Waldhauser and Ellsworth, 2000). Next, 393 focal mechanism solutions were derived from high-frequency body-wave amplitudes and polarity measurements using program FOCMEC (Snoke et al., 1984). We inverted the focal mechanisms to determine a best-fitting stress regime, and found that the results depend on the location of the aftershocks with respect to the mainshock rupture. Finally, we performed a Coulomb stress transfer analysis and observed that there is a very strong correlation between static Coulomb stress increase caused by the mainshock and the aftershock hypocenter locations and focal mechanisms.

2.2 Data and Processing

2.2.1 Aftershock Locations

Shortly after the mainshock, teams from Virginia Tech, University of Memphis, Lehigh University, Incorporated Research Institutions for Seismology (IRIS) and the U. S. Geological Survey (USGS) deployed seismic instruments and recorded a dataset that is archived at the IRIS Data Management Center. Figure 2.1 shows the locations of the 32 temporary stations used in this study, network codes and station names. We used the entire available data set recorded from 25 August, 2011 through 31 December, 2011, when the seismicity rate was high and location capability was maximum and stable. We applied a detection

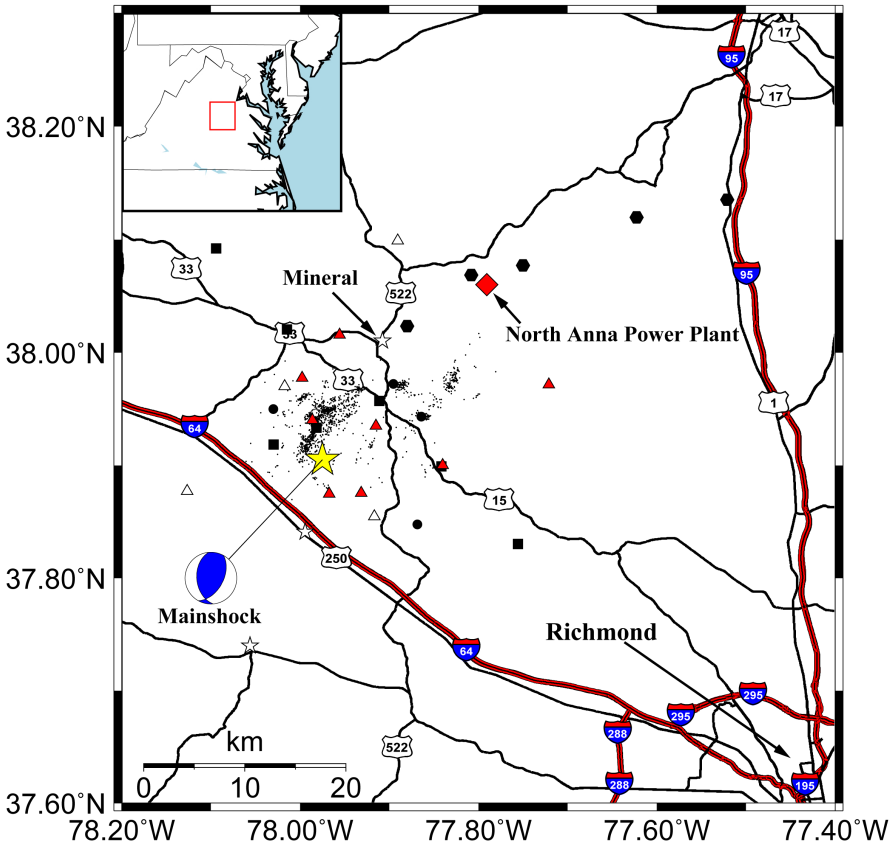

Figure 2.1: Stations used in this study. Symbols distinguish different network codes for data archived at the IRIS data management center: YC (filled squares); NQ (open triangles); GS (filled hexagons); NP (open stars); XY (filled triangles); ET(filled circles). The mainshock focal mechanism is from Herrmann (2011). The epicenters of three subevents comprising the mainshock are indicated by the filled star and crosses (Chapman, 2013).

algorithm that combined the short-term average and long-term average ratio (STA/LTA) method (Allen, 1982; Withers et al., 1998) with a cross-correlation method that scanned through the continuous waveform recordings with signal templates to detect as many events as possible. The cross-correlation method refined the STA/LTA detections by removing many false triggers and detected additional small events. The automatic detections were visually reviewed. This resulted in 3,960 aftershocks detected within the 129 day time range of our study.

Arrival times of P- and S-waves were manually picked from the detected event waveforms. A total of 3,018 earthquakes were located initially using the single-event location program HYPOELLIPSE (Lahr, 1999). The data set we used for further analysis involved 1,666 particularly well-constrained events with at least 10 arrival time picks and a root-mean-square (RMS) travel-time residual less than 0.1 s. The 1-D velocity model used here is based on the velocity model routinely used for hypocenter location in central Virginia by the Virginia Tech Seismological Observatory (Bollinger et al., 1980). That model was further refined by analyzing early aftershocks of the Mineral earthquake (Chapman, 2013). The velocity model consists of three layers. The upper crust is represented by a 15-km-thick layer with P- and S-wave velocities of 5.96 km/s and 3.53 km/s respectively. The lower crust has a P-wave velocity of 6.50 km/s, S-wave velocity of 3.79 km/s and a thickness of 21 km. Below the Moho, the half-space P-wave and S-wave velocities are 8.18 km/s and 4.73 km/s, respectively. Tomographic imaging using aftershock data recorded from a short-term deployment of instruments with very close station spacing indicates a near-homogenous velocity structure in the upper crust above the mainshock fault zone (Davenport et al., 2015).

Initial hypocenter locations in map and profile view are shown in Figure 2.2 along with the three subevents of the mainshock determined by Chapman (2013). In map view the aftershocks within 10 km of the mainshock lie in a northeast-trending cluster which, in 3-dimensions, forms a southeast-dipping tabular zone with general orientation closely similar to that of a mainshock focal mechanism nodal plane. Below, we refer to these events as the main cluster. However, many aftershocks occurred further to the east and northeast of the mainshock, in several small clusters, mostly located 10 - 20 kilometers from the main cluster. Below, we refer to the more distant 282 aftershocks to the east and northeast of the main

cluster as the northeastern aftershocks.

We applied the double-difference algorithm HypoDD (Waldhauser and Ellsworth, 2000; Waldhauser, 2001) using differential times from manual phase picks to better refine the spatial distribution of the aftershocks. The relative arrival times obtained from the waveform cross-correlation analysis could be used to determine the relative locations, however, our dataset from the dense local network generally has high signal-to-noise ratio (SNR) allowing for manual determination of impulsive P- and S-wave arrival times to a precision of 0.01 s. The initial locations had an average RMS travel time error of 0.036 s, average 68% confidence horizontal location error of 0.66 km, and an average 68% confidence vertical error of 2.01 km. Double difference aftershock relocations are shown in Figure 2.3 in map and profile views. The error estimates reported by HypoDD for both horizontal and vertical directions are tens of meters. The double difference locations do not significantly differ from the initial locations in terms of horizontal location. However, many events that were initially located near the surface were relocated to greater depth. The initial single-event locations have an average depth of 4.01 km (median 4.43 km); in comparison, the average depth determined by HypoDD is 4.42 km (median 4.50 km). The shallowest event was located 0.2 km and the deepest was 12.0 km.

Main Aftershock Cluster

A plane striking N33°E and dipping of 51°to the southeast was fit by least-squares to the hypocenters relocated using HypoDD in the main aftershock cluster. This is consistent with the strike and dip of a mainshock nodal plane and is essentially the same result reported in previous studies (Herrmann, 2011; Chapman, 2013; McNamara et al., 2014; Wu et al.,

2014; Horton et al., 2015b). However, the larger data set used here reveals an interesting spatial distribution of hypocenters. Figure 2.3c shows that the majority of the aftershocks at depths greater than 2 km in the main cluster are situated in a curious arcuate pattern that approximates a quarter-circle of radius 4 km in the plane of the aftershocks, centered on the point of mainshock rupture initiation determined by Chapman (2013). Previous investigators have reported a tendency for aftershocks to cluster mostly outside of or near the edges of the source areas experiencing major slip (Mendoza and Hartzell, 1988). Gomberg et al., (2003) argue that seismicity triggered dynamically by directive rupture should occur asymmetrically with the majority of the triggered earthquakes in the direction of rupture propagation. For the Mineral earthquake, a compact, detached cluster of aftershocks at 8 km depth coincides almost exactly with the estimated location of the small subevent that marked mainshock rupture initiation. The estimated locations of the two much larger subevents that together were responsible for roughly 93% of the mainshock moment release lie within an obvious gap in aftershock activity (approximately 2-3 km wide, Fig. 2.3c).

The hypocenters define a tabular zone approximately 1 km in thickness with strike and dip in agreement with the orientation of a mainshock nodal plane. This was interpreted to delineate a previously unknown fault (Quail fault, Horton et al, 2015b). Yet, as will be discussed below, many of these aftershocks exhibit focal mechanisms different from the mainshock, and represent slip on faults other than the one responsible for the mainshock. The asymmetric arrangement of the majority of these aftershocks in a rough quarter-circle halo about the mainshock rupture reflects the direction of mainshock rupture propagation, which proceeded up-dip and along strike to the northeast, from the point of rupture initiation toward the area where the majority of main cluster aftershocks are concentrated (Chapman, 2013). It appears

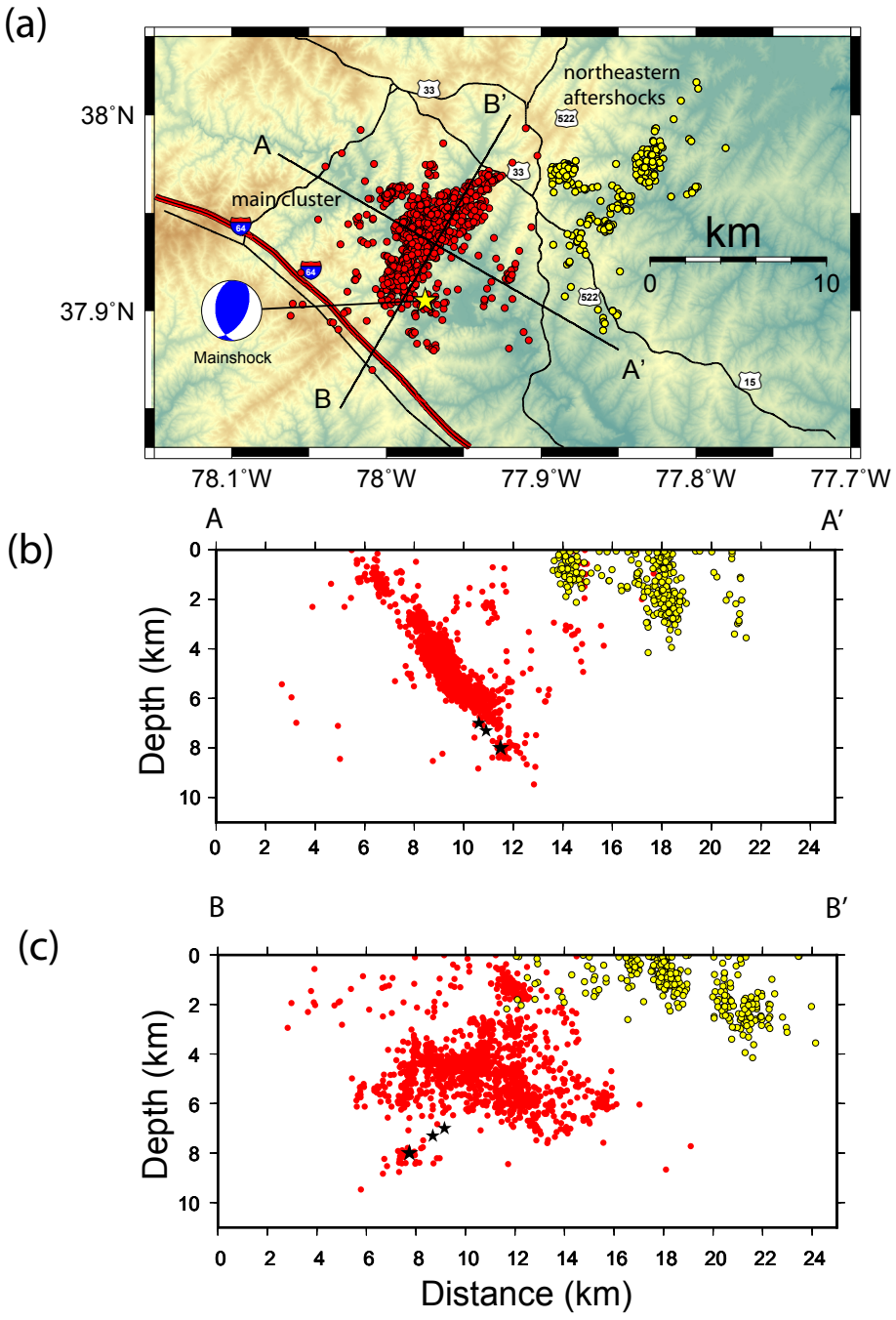

Figure 2.2: (a) Initial hypocenter locations of 1701 aftershocks using program Hypoellipse (Lahr, 1999). The mainshock focal mechanism is from Herrmann (2011). (b) Profile AA' is oriented N123°E. (c) Profile BB' is oriented along strike of a plane fit to the main cluster aftershocks: strike N33°E, dip 51°to the southeast. Mainshock subevents are shown by the filled stars (Chapman 2013).

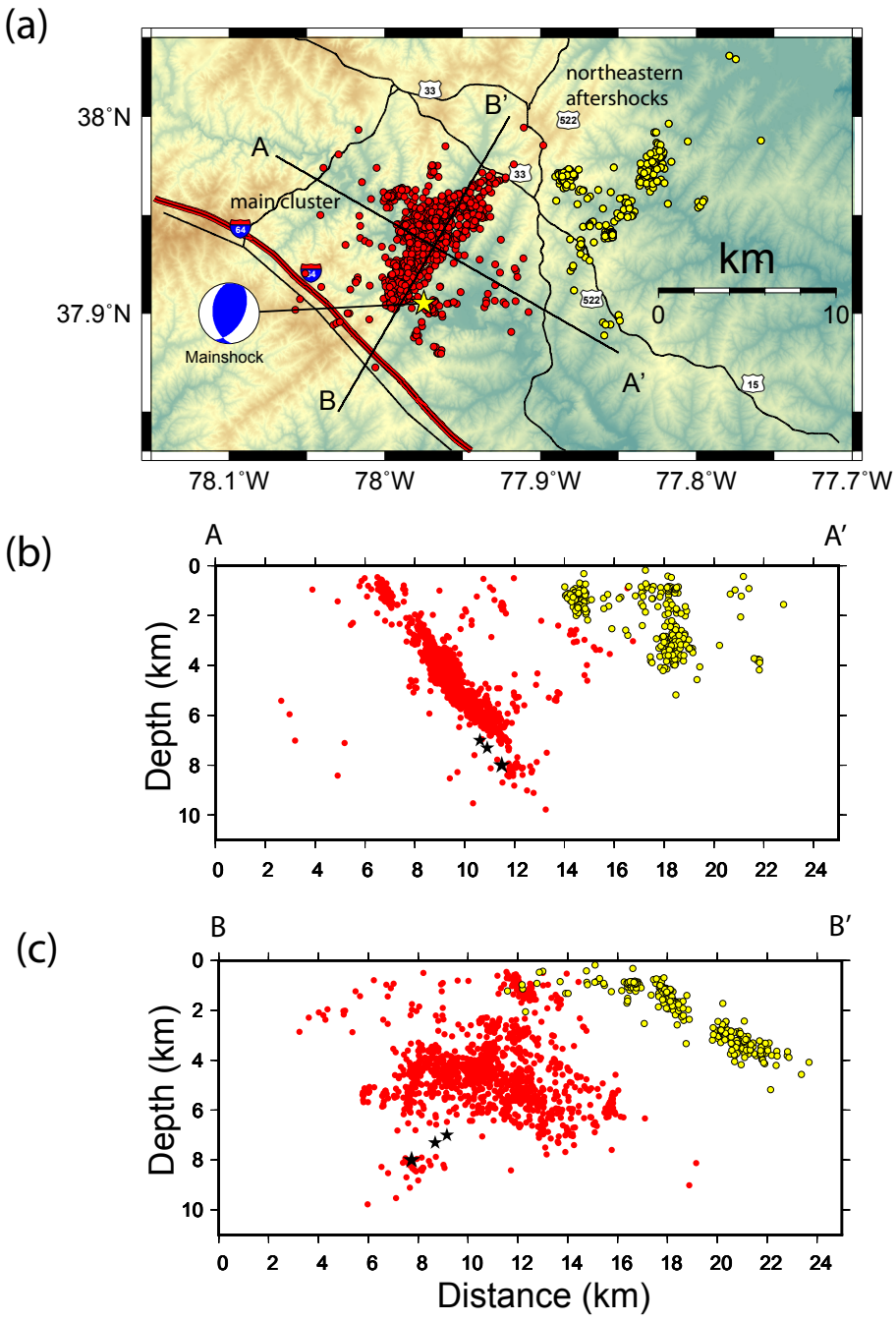

Figure 2.3: (a) Double-difference hypocenter relocations of 1666 aftershocks using program HypoDD (Waldhauser, 2001). The mainshock focal mechanism is from Herrmann (2011). (b) Profile AA' is oriented N123°E. (c) Profile BB' is oriented along strike of a plane fit to the main cluster aftershocks: strike N33°E, dip 51°to the southeast. Mainshock subevents are shown by the filled stars (Chapman 2013).

that the aftershock distribution in the main cluster was affected to a large extent by focusing of dynamic stresses due to the rupture directivity of the mainshock and a redistribution of stress away from the area where most mainshock slip occurred. Evidence for dynamic stress changes affecting aftershock patterns has been observed in other aftershock sequences (Gomberg, et al., 2003) and Coulomb static stress changes are well-known to strongly impact the spatial distribution of aftershocks (e.g., Reasenberg and Simpson, 1992; Harris, 1998; Stein, 1999). Thus, both dynamic and static stress changes due to the mainshock apparently played a role in defining the geometry of the main aftershock cluster.

Northeastern Aftershocks

The northeastern aftershocks are located 10-20 km from the mainshock and at shallow depths between 1 and 5 km. Most of the events are in one tight cluster and in two looser clusters. In map view (Fig. 2.4) the epicenters in the two loose clusters furthest from the mainshock suggest a northeasterly trend (profile F-F', Fig. 2.4), approximately parallel to the strike of mapped Paleozoic geologic structure (Pratt et al., 2015). Horton et al. (2015b) interpreted this as a northeast-trending, near-vertical Fredericks Hall fault, named for a nearby locality. However, the larger data set available in this study and our locations of hypocenters east of 77.9°W longitude indicate that the focal depths of the events that form the apparent northeast-trending alignment of epicenters systematically deepen to the northeast (Fig. 2.4c). The hypocenters in the northeastern group lie close to a single plane fit by least squares that strikes N320°E, in the direction of profile E-E' (Fig. 2.4a) and dips 29°to the northeast. Those in the tight cluster exhibit the same strike but a slightly steeper dip. Furthermore, the majority (29 out of 35, 83%) of focal mechanism solutions determined

for the northeastern events, further discussed in a later section, indicate reverse faulting on predominantly north-northwest trending nodal planes. Figure 2.4 shows the locations of the northeastern hypocenters in map view and in vertical projection along profiles oriented N320°E and N50°E. The spatial geometry of the northeastern aftershocks differs from the events in the main cluster. A northwesterly striking planar structure does not correspond with mapped Paleozoic structure in the study area (see Pratt et al., 2015; Horton et al., 2015a, 2015b). We will return to the spatial geometry of the aftershock hypocenters, in connection with the focal mechanism determinations and the Coulomb stress transfer analysis, in later sections. Next, we examine the temporal aspects of the aftershock sequence.

2.2.2 Statistical Analysis

Magnitude calculations were made using the signal duration and the peak amplitudes calibrated to yield indirect estimates of $m_{b(Lg)}$ (Nuttli, 1973). The routinely used duration magnitude (M_d) scale developed at Virginia Tech in the 1980s was derived from earthquakes in the central and southern Appalachians using short-period recordings at local and regional distances:

$$M_d = 2.83 \log_{10}(t_d) - 3.42 \tag{2.1}$$

where t_d is the duration in seconds of signal measured on 1-Hz instruments from P-wave onset until the time at which the coda amplitude equals the pre-event noise amplitude.

Equation (2.1) is based on a regression of $m_{b(Lg)}$ magnitude on $\log_{10}(td)$. M_d estimated

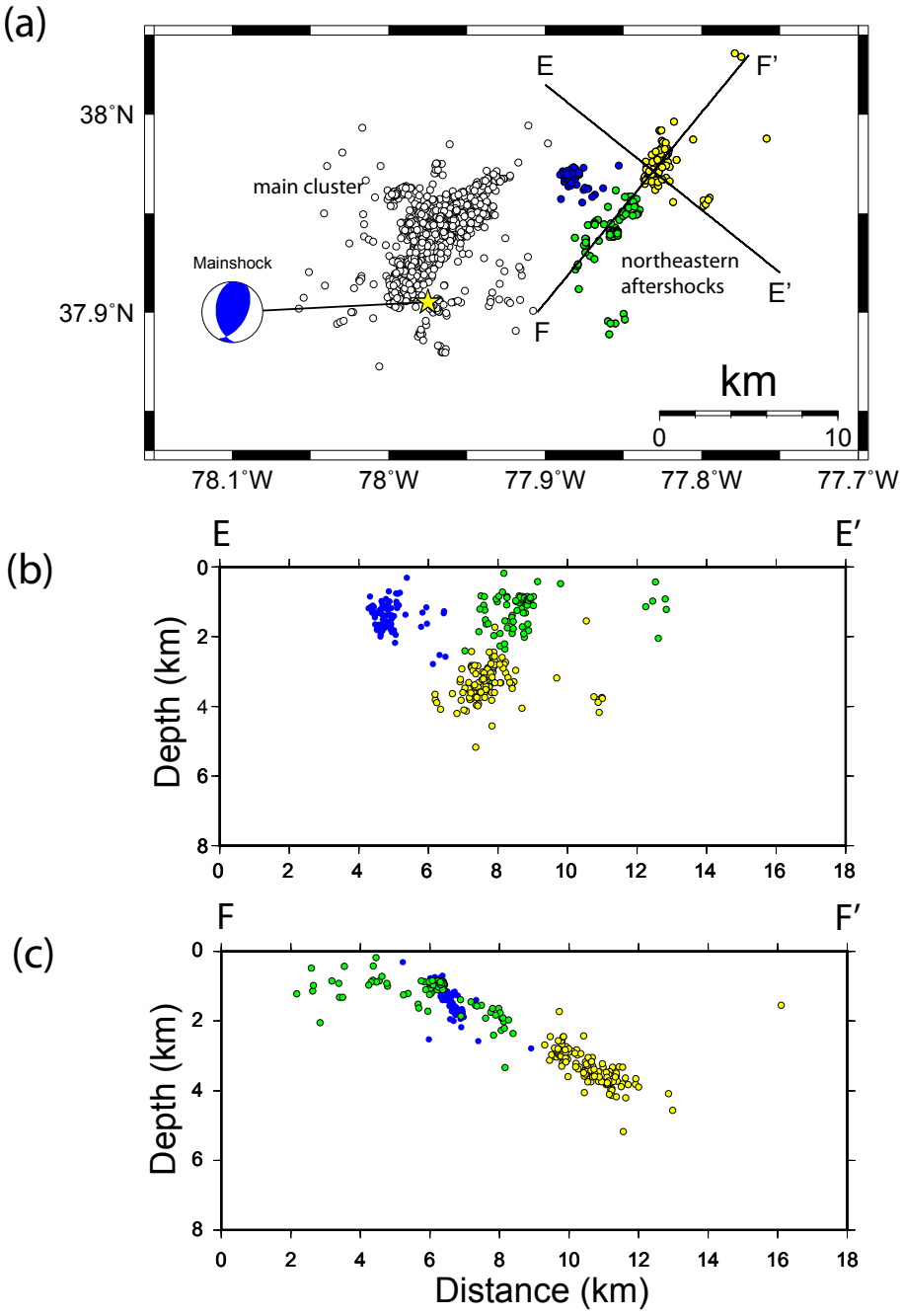

Figure 2.4: (a) Double-difference hypocenter relocations of 1666 aftershocks using program HypoDD (Waldhauser, 2001). The mainshock focal mechanism is from Herrmann (2011). (b) Profile EE' is oriented along strike of a plane fit to the northeastern aftershock group: strike N320°E, dip 29°to the northeast. (c) Profile FF' is oriented N50°E. Spatially distinct clusters in map view are indicated by different shading.

from equation (2.1) is an indirect estimate of $m_{b(Lg)}$ based on signal duration, and has been used for smaller earthquakes occurring in the CVSZ for decades. However, the aftershock data include large numbers of tiny shocks recorded at epicentral distances less than 10 km, and measured duration reaches a constant lower limit for the smaller earthquakes: *i.e.,* we observed an artificial saturation of M_d at small magnitudes. This was particularly the case during the first week following the mainshock when Hurricane Irene was passing along the coast of Virginia.

Table 2.1: Zeroes and poles corresponding to station PTTY.

Zeroes	Poles	Constant (counts/m)
(0.0, 0.0)	(-8.8860, 8.8860)	1.77218×10^9
(0.0, 0.0)	(-8.8860, -8.8860)	
(0.0, 0.0)		

We developed a new magnitude scale ($M_d{}^\star$) based on the peak trace amplitude measurements of three-component short-period data to automate and extend the determination of magnitude over the full range of our event detection capability. We selected 100 of the larger aftershocks with reliable M_d estimates and calculated the mean value of the maximum trace amplitudes measured on the three components. The attenuation with distance was assumed to be due to body-wave geometrical spreading in a homogeneous Earth and was taken into account by multiplying the trace amplitude by the hypocentral distance. In this process, we only used data from the 7 stations of network XY (Fig. 2.1), because those instruments were well calibrated with known instrument response and located within 10 km of the epicentral area of the main shock. A regression of M_d on the logarithm of distance-corrected trace

amplitude yielded the following equation for $M_d{}^*$, which in turn is calibrated to $m_{b(Lg)}$:

$$M_d{}^* = \log_{10}(R * A) - 4.2 \tag{2.2}$$

where R is hypocentral distance in kilometers and A is averaged 3-component peak trace amplitude in digital counts on an arbitrarily chosen standard instrument (station PTTY, 2 Hz short-period). The standard instrument transfer function, in terms of Laplace transform poles and zeros, is given in Table 2.1. Note that the logarithm of distance-corrected amplitude differs from $M_d{}^*$ by a constant, which implies that the assumed geometrical spreading correction is successful. Figure 2.5a shows the correlation between M_d and $M_d{}^*$ for the 100 selected events used to develop equation (2.2).

The distribution of aftershocks as a function of $M_d{}^*$ is shown in Figure 2.5b, based on magnitude bins 0.1 units wide. Like most aftershock sequences, the magnitude-frequency distribution as shown in Figure 2.5c follows the Gutenberg-Richter relation (Ishimoto and Iida, 1939; Gutenberg and Richter, 1944):

$$\log_{10} N = a - bM_d{}^* \tag{2.3}$$

where N is the cumulative number of aftershocks with magnitude equal to or greater than $M_d{}^*$ and a and b are empirical constants. In Figure 2.5c, the departure of the data from the linear trend indicates a detection threshold magnitude of about -0.4 for this aftershock sequence during the period of study. Analysis of the Mineral aftershock sequence through the

end of 2011 resulted in the estimate $a = 3.349 \pm 0.026$ and $b = 0.864 \pm 0.013$, which is consistent with the b-values in stable continental interiors (0.865±0.226; Ebel, 2009). McNamara et al. (2014) found a lower b-value of 0.75±0.04 using a different magnitude scale and a smaller dataset complete to magnitude 1.1.

We also analyzed the decay of the aftershock sequence with time, which is usually described by the modified Omori law (Utsu, 1961; Kisslinger and Jones, 1991; Utsu et al., 1995):

$$\dot{N(t)} = \frac{C_1}{(C_2 + t)^p} \tag{2.4}$$

where $\dot{N(t)}$ is the count of earthquakes per day, t is time after the mainshock in days, and C_1, C_2 and p are constants. The p-value defines the decay of aftershock rate and has been found to vary between about 0.6 and 1.4 (Wiemer and Katsumata, 1999). The p-value for the Mineral aftershocks was estimated to be 1.085±0.058 by least square fitting (Fig. 2.5d), which is well within the ranges estimated for stable continental regions (1.046±0.221) by Ebel (2009). The estimates of the other constants in equation (2.4) are $C_1 = 817.518 \pm 75.136$ and $C_2 = 2.992 \pm 0.634$.

2.2.3 Focal Mechanisms and Stress Inversion

Focal mechanism solutions were determined using P- and SH-wave first-motion polarities and P, SH and SV amplitude information derived from the 3-component records. The program FOCMEC (Snoke et al., 1984) was used to search through all possible fault plane

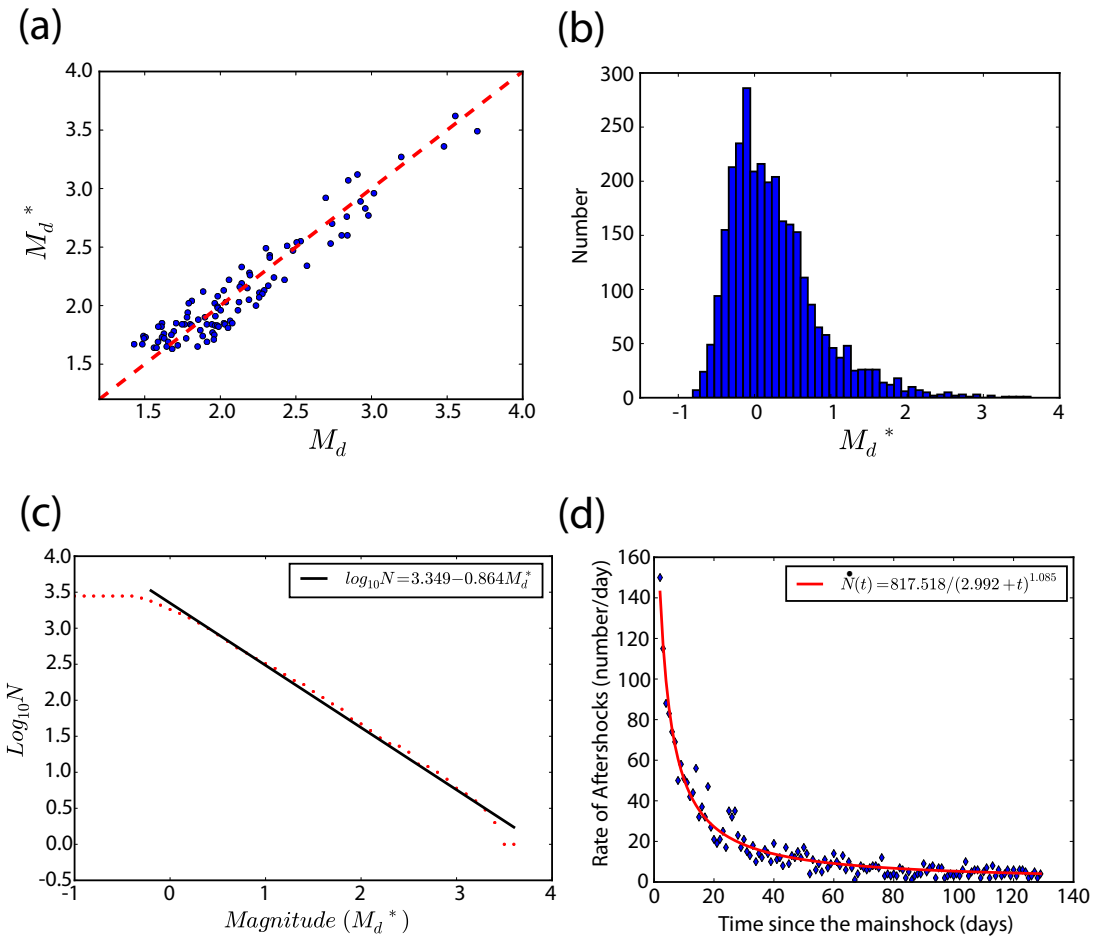

Figure 2.5: (a) Plot of the new magnitude scale developed in this study $M_d{}^*$ versus the duration magnitude scale M_d for the 100 events used to determine equation (2.2). (b) Histogram of the number of earthquakes per day versus $M_d{}^*$ for the study period. (c) Gutenberg-Richter recurrence relationship for the study period. N is the cumulative number of events greater than $M_d{}^*$ for the entire study period. The magnitude of completeness is $M_d{}^* = -0.4$. (d) Daily rate of earthquakes with $M_d{}^* > -0.4$ versus time since the mainshock. The line shows the least-squares fit of the modified Omori law to the data.

solutions by comparing the observations with the predictions based on selection parameters specified by the user. The selection parameters include the number of allowed polarity errors, the range for deviations between observed and calculated amplitude ratios, and the number of ratio errors that are allowed outside that range (Snoke, 2009). Horizontal components were rotated to radial (SV) and transverse (SH) components for determining polarities and amplitude ratios. Because most of the XY and YC network stations are close to the aftershock clusters, signal-to-noise ratios were good for a large number of events. Also, the azimuthal distribution of stations shown in Figure 2.1 provided good constraint on focal mechanisms. The use of SH-wave polarity and SH/P, SV/P amplitude ratios in addition to P-wave polarity provided much additional constraint. The amplitudes were measured at the first peak or trough following the first-motion onset on the integrated traces. Free-surface amplitude corrections were made. The maximum number of allowed polarity errors was 4. For most events, more than 10 polarities and tens of amplitude ratios were measured. Figure 2.6a shows the radial, transverse and vertical components of an $M_d{}^*$ 1.2 event that occurred on 22 September, 2011 recorded at station PTTY. P- and SH-wave polarities are clear on the vertical and transverse components respectively. Figure 2.6 shows the focal mechanism solution for the example event. The preferred solution is that with minimum RMS amplitude ratio error, chosen from the set of possible focal mechanism solutions determined by FOCMEC.

We compared our focal mechanism solutions with all the corresponding solutions determined from regional moment tensor inversion using low-frequency waveforms (Herrmann, 2011). In all but two cases (event numbers 1 and 11), the solutions are virtually identical, indicating that the high-frequency data from local short-period stations can indeed produce reliable

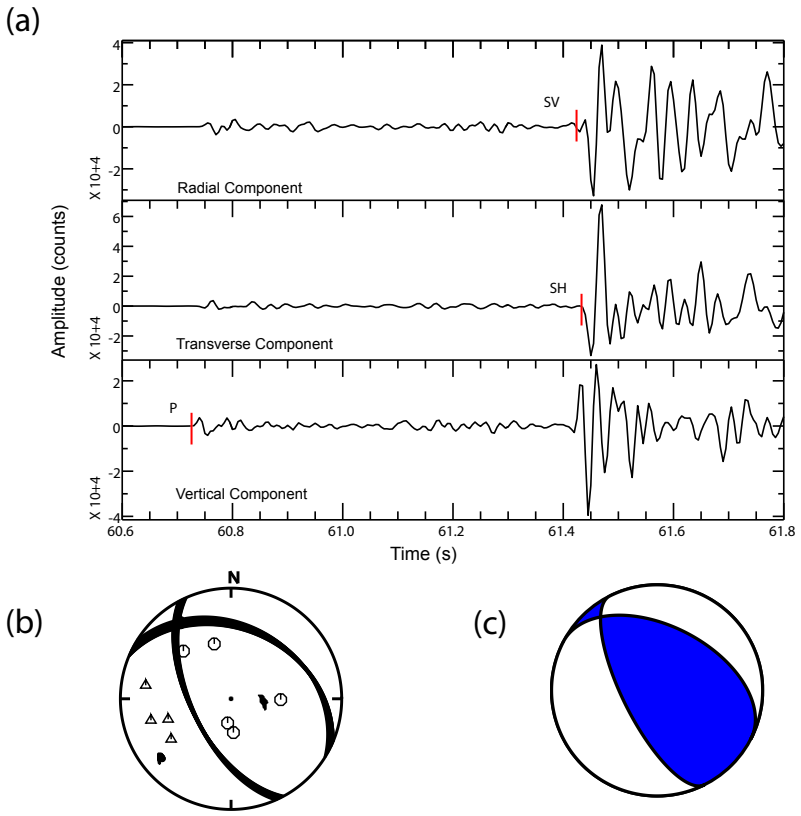

Figure 2.6: (a) Example waveforms for a typical M_d^* 1.2 event. Arrival times of P, SV and SH are indicated. (b) All possible focal mechanism nodal planes, with P polarities (triangles, hexagons) and P and T axes. (c) Best fitting solution, determined on the basis of minimum RMS amplitude ratio error.

mechanisms for these events (Fig. 2.7). Note that event 1 occurred on 25 August, 2011, when data quality was poor because of the large microseisms caused by Hurricane Irene, which struck the U.S. mainland on the North Carolina coast as a Category 1 hurricane, and then moved northward across Virginia and then to the northeastern U.S. (McNamara et al., 2014). Also, high-frequency polarity and amplitude data were sparse for this event due to noise levels.

Figure 2.8 plots all 393 focal mechanisms in map view and projected on planes perpendicular and parallel to the mainshock strike (N30°E). Figure 2.9 shows vertical projections of 35 focal mechanisms determined for the northeastern group of aftershocks. The solutions were classified into faulting types based on the plunge of P, T and B axes (Zoback, 1992) and listed in Table 2.2. The advantage of this classification is that it is based on more information than a simple classification based on rake, and is independent of the choice of fault plane. A total of 275 events are of reverse type, 35 oblique-reverse, 29 strike-slip, 12 normal and 1 oblique-normal (Table 2.2). Forty-one events marked as NA were not classified using the scheme, which may happen when the faulting types of the two nodal planes are different. Reverse faults dominate (70%) but all types of focal mechanism were observed. A large number of the aftershock mechanisms differ substantially from that of the mainshock. Only 54 events feature strike, dip and rake all within 20 degrees of the strike, dip and rake of the mainshock, i.e., strike: 28°±20°, dip: 50°±20°and rake: 113°±20°. Based on those criteria, more than 85% of the aftershock focal mechanism solutions differ from the mainshock. Heterogeneous focal mechanisms have been observed in previous shocks, for example, the 1989 M 6.9 Loma Prieta earthquake (Michael et al., 1990) and the 1992 M 7.3 Landers earthquake (Hauksson, 1994).

We plotted P-axis trends of all focal mechanisms in rose diagrams to examine the distribution of solutions (Fig. 2.10). The results indicate a significant variation in P-axis orientation, suggesting that aftershocks occurred on sets of fault planes with different orientations. We divided the focal-mechanism into 3 ranges of focal depth (0 - 4 km; 4 - 6 km; and > 6 km) and observed that the shallow aftershocks (depth < 4 km) had sub-horizontal P-axis trends of approximately N70°E. This includes events in both the main cluster and the majority of events in the northeastern group. But in the depth range from 4 to 6 km, which contains the majority of aftershocks in the main cluster and only a few in the northeastern group, three distinct sets of faults were active, one with the N70°E P-axis trend of the shallow events, one set with P-axes mostly trending approximately N135°E and the third with the P-axis trend of approximately N160°E, which represents a 90°rotation with respect to the trend of the shallow events. Finally, the P-axis trends of the 36 mechanisms for aftershocks in the depth range of the mainshock rupture (6-8 km), all in the main cluster, are approximately N85°E to N120°E, which includes the P-axis trend of the mainshock (N103°E).

Table 2.2: Types of faulting.

P-Plunge (PPl)	B-Plunge (BPl)	T-Plunge (TPl)	Type of Faulting	Number of Solutions
PPl > 52°		TPl < 35°	Normal	12 (3%)
40°< PPl < 52°		TPl < 20°	Normal Oblique	1 (0.3%)
PPl < 40°	BPl > 45°	TPl < 20°	Strike Slip	29 (7.4%)
PPl < 20°	BPl > 45°	TPl < 40°	Strike Slip	
PPl < 20°		40°< TPl < 52°	Reverse Oblique	35 (8.9%)
PPl < 35°		TPl > 52°	Reverse	275 (70%)
			NA	41 (10.4%)

The aftershock hypocenter locations (Fig. 2.3) suggest a single fault plane in the main

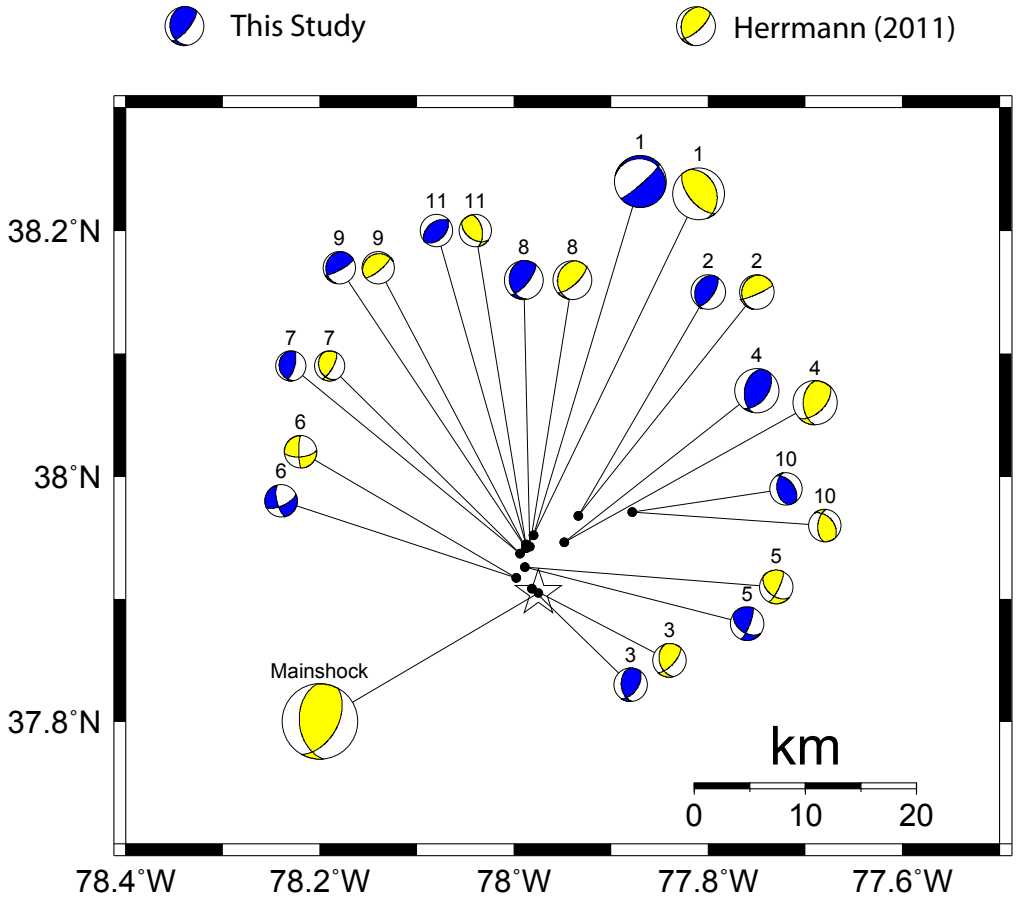

Figure 2.7: Comparison of focal mechanism solutions determined in this study with those derived from regional moment tensor inversion (Herrmann, 2011).

cluster containing the mainshock rupture area and aftershocks. But the focal mechanisms indicate otherwise. The tabular volume contains earthquakes with distinctly different fault orientations. The majority of mechanisms are reverse, with sub-horizontal P-axis plunge. Significantly, the P-axis azimuths range over 90 degrees.

We performed stress inversions using the focal mechanisms. The data were split into different depth intervals to study potential depth variations of the local stress regime throughout the aftershock sequence. The package MSATSI (Martnez-Garzn et al., 2014) used in this study is based on the stress inversion algorithm SATSI developed by Hardebeck and Michael (2006), which is a damped inversion method that simultaneously inverts for the stress field orientations in subareas taking into account the adjacent subareas to smooth the solution, and provides a bootstrap re-sampling uncertainty assessment. Outputs are the orientations of the three principal stresses, σ_1, σ_2, σ_3, and a relative stress magnitude $R = (\sigma_1 - \sigma_2)/(\sigma_1 - \sigma_3)$.

Individual stress inversions were done for the main cluster and the northeastern aftershocks (Fig. 2.11). The results suggest, at first glance, a difference between those two groups of aftershocks. Using all 358 events in the main cluster, the stress inversion best-estimate azimuth for the maximum principle stress (σ_1) is N55°E (N235°E) with sub-horizontal plunge. The 95% confidence region for the azimuths of σ_1 and σ_2 in the main cluster is large, approximately 70 degrees, whereas the near-vertical orientation of σ_3 is well constrained. This reflects the diversity of focal mechanisms in the main cluster. In contrast, the inversion result of 35 events in the northeastern cluster shows a well-constrained N75°E-trending σ_1 with a shallow plunge of 15 degrees. Thus, the best-estimate orientation of the stress field for the northeastern aftershocks appears to be rotated approximately 20 degrees clockwise

from the best estimate of the stress regime orientation using all shocks in the main cluster. However, most of the northeastern events are shallow (less than 5 km) whereas the main cluster is comprised mostly of deeper events, and the focal mechanisms in the main cluster show variability with depth (Fig. 2.10).

The events in the main cluster were divided into 3 different depth ranges (Fig. 2.11). For 94 focal mechanism solutions at depths less than 4 km, the stress inversion returned an ~ N80°E-trending sub-horizontal maximum principal stress (σ_1) and a nearly vertical σ_3, which is in good agreement with the P-axis trends (Fig. 2.10b). The stress inversion of 228 events between 4 and 6 km depth resulted in a sub-horizontal σ_1 with an azimuth of N235°E (N55°E). The best fit 1 direction for events deeper than 6 km, although not well constrained with only 36 events, is sub-horizontal with a trend of ~N100°E, which agrees with the P-axis azimuth of the mainshock focal mechanism (Herrmann, 2011).

The derived stress orientation of the shallow (< 4.0 km) events in the main cluster is very similar to that derived from the northeastern aftershocks. The apparent stress rotation mentioned above is not between the main cluster and the northeastern aftershocks, but occurs within the main cluster. A clockwise rotation of the inverted stress field occurs within the depth range 4 to 6 km where most of the main cluster aftershocks are located. The best-estimate azimuth of the sub-horizontal maximum compressive stress (σ_1) changes from N80°E at shallow depth to N100°E at the depth of the mainshock (8 km, approximately). The 4-6 km depth range shows a large (90 degree) range of focal mechanism P-axis trend (Fig. 2.8c) and the density of aftershocks in this depth range suggests that it may mark the shallow limit of significant mainshock slip.

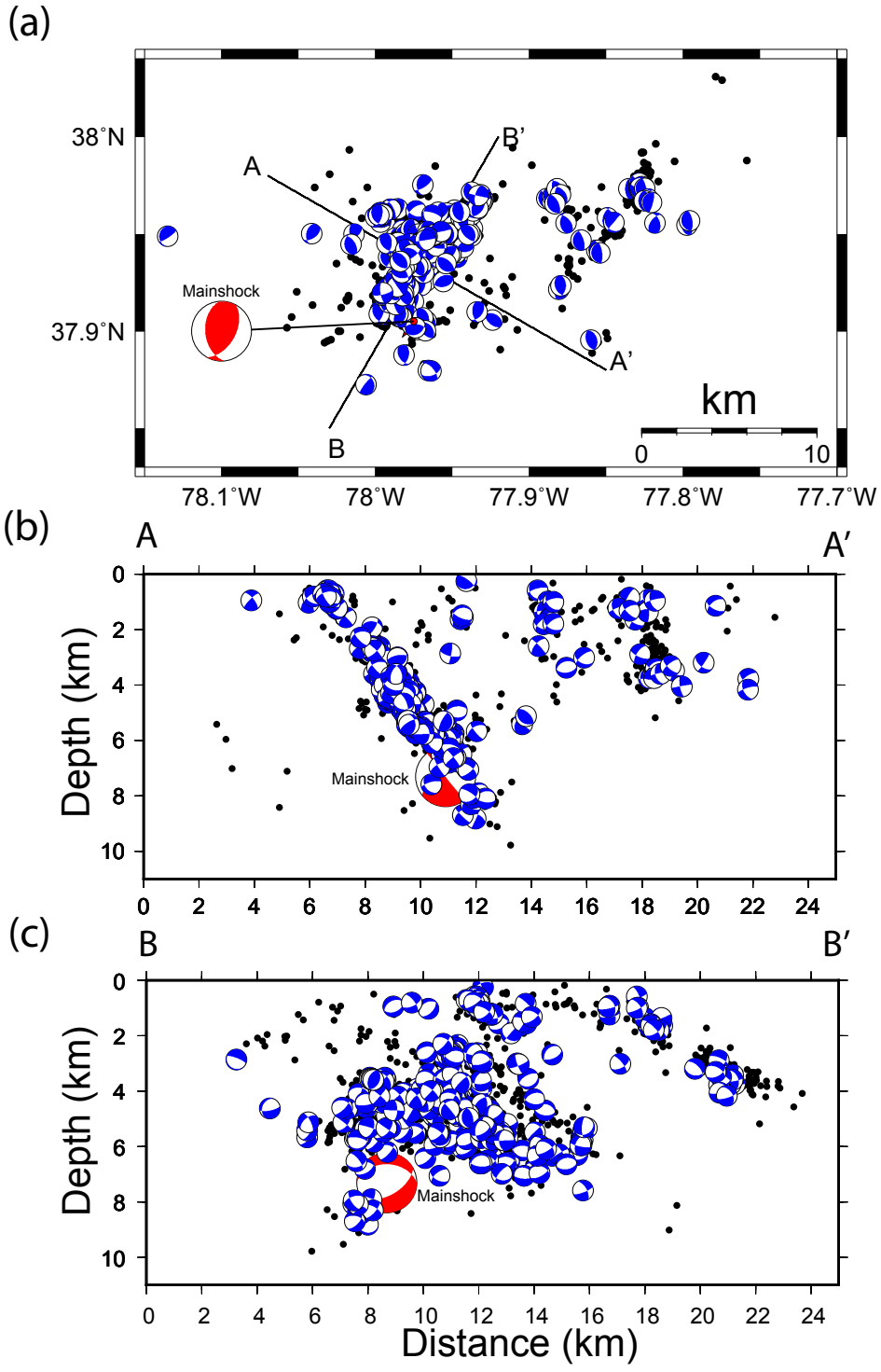

Figure 2.8: (a) Map view of 393 aftershock focal mechanism solutions determined in this study (lower hemisphere projection). (b) Profile view along AA' (N123°E). (c) Profile view along BB' (N33°E). Hypocenter locations of additional aftershocks without focal mechanism solutions are shown by the small filled circles. The mainshock focal mechanism solution is from Herrmann (2011).

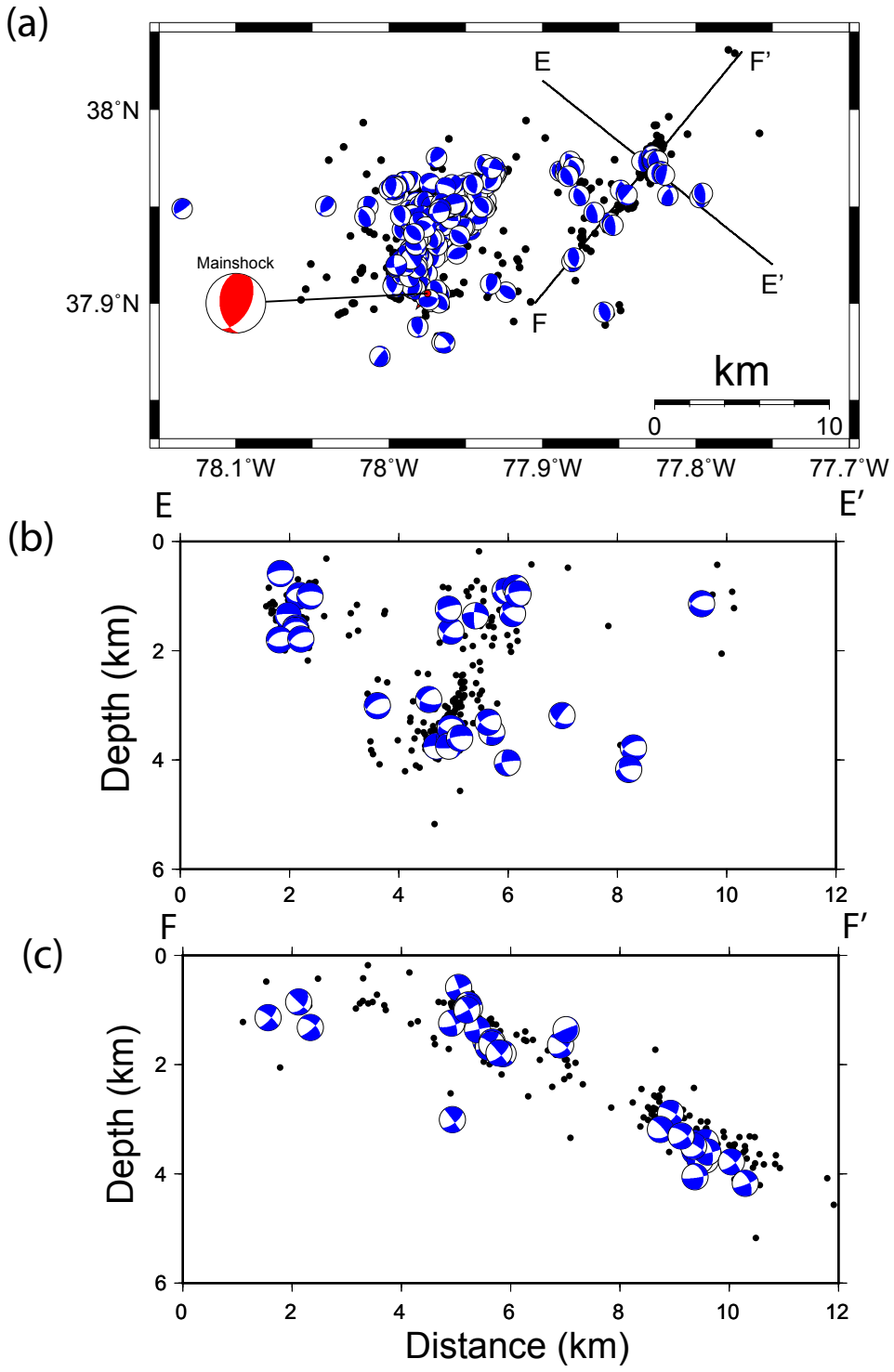

Figure 2.9: Similar to Figure 2.8, but showing expanded scale on the vertical profiles E-E' (N320°E) and F-F' (N50°E) in the northeastern aftershock group. Note the good correlation of nodal plane orientation with the spatial geometry of the hypocenters, indicating primarily reverse faulting on N-NW striking fault(s).

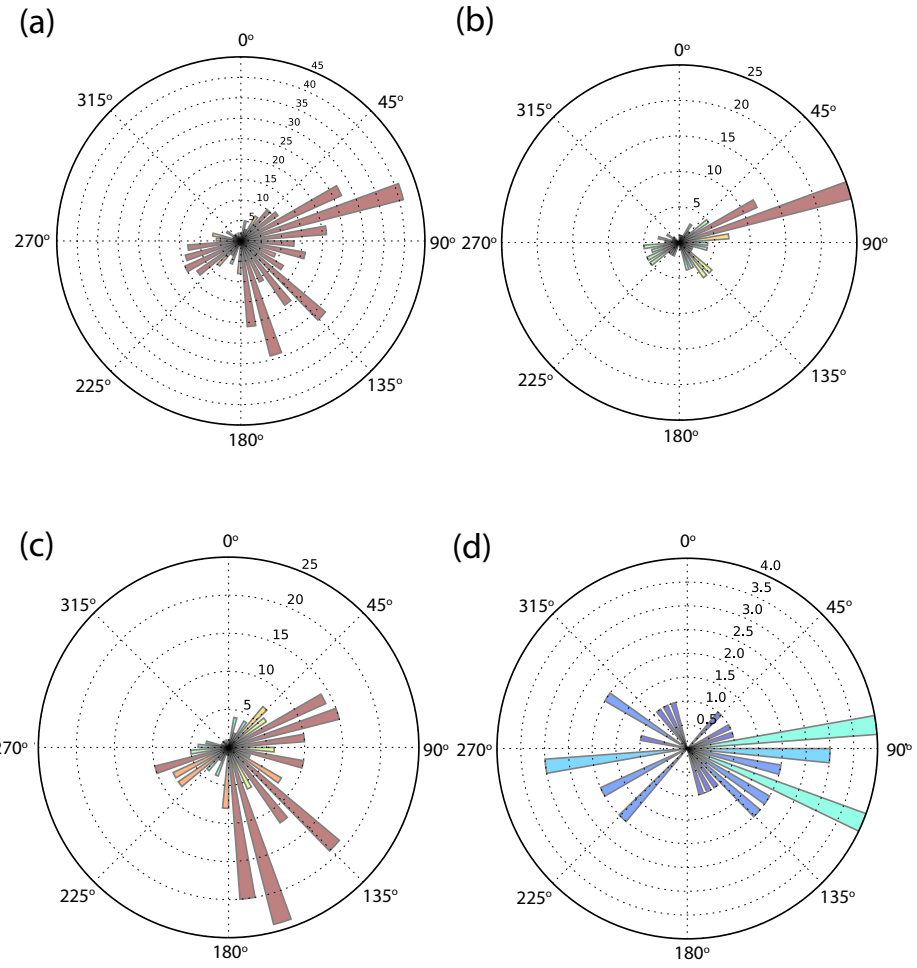

Figure 2.10: (a) Rose diagrams showing the frequency of P-axis trends of 393 focal mechanisms. (b) Focal depth between 0 and 4 km (126 events). (c) Focal depth between 4 and 6 km (231 events). (d) Focal depth greater than 6 km (36 events).

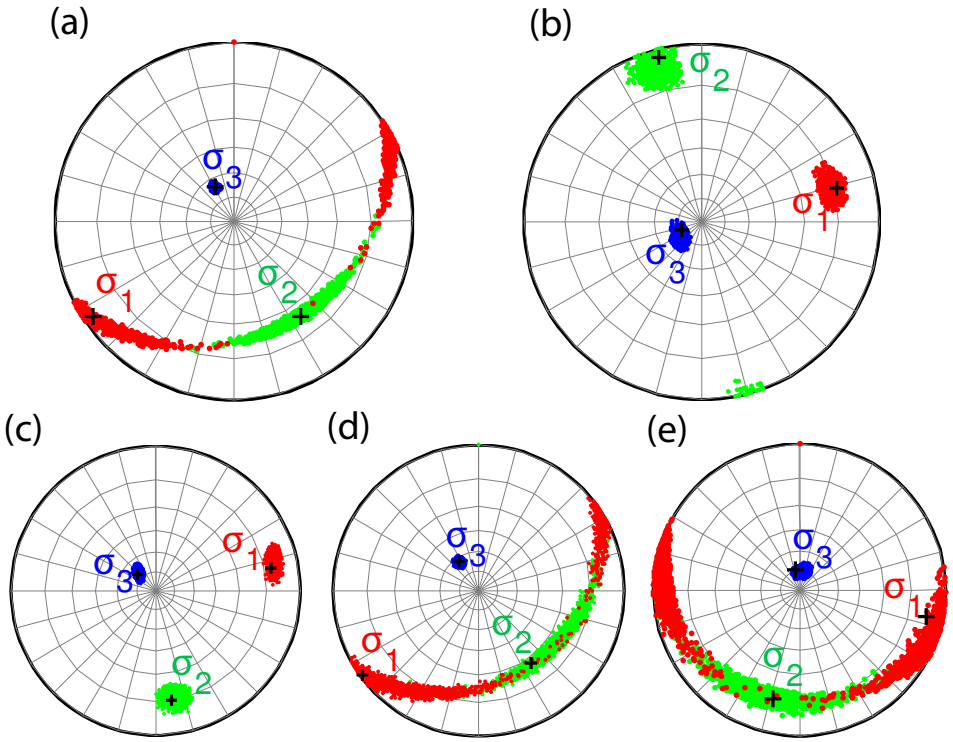

Figure 2.11: (a) Stress inversion results for focal mechanisms in the main cluster. (b) Stress inversion for the northeastern cluster. (c), (d) and (e) show the stress inversion results for depth range 0-4 km, 4-6 km, and greater than 6 km, respectively. The cross symbols denote the best estimate of the direction of the principal stress axes. The results are plotted using stereonet and lower hemisphere projection.

It is important to recognize that the inferences made here about the stress field are indirect, being based entirely on observations of the aftershock focal mechanisms (strain events).

2.2.4 Coulomb Stress Transfer Analysis

To better understand the aftershock distribution and the complexity of focal mechanisms and stress field, we investigated the static stress interaction between the mainshock and

aftershocks by applying a Coulomb stress transfer analysis. Earthquakes result in two types of stress change: permanent static stress changes in the surrounding crust, and temporary dynamic stress changes due to the passage of seismic waves. Dynamic stress changes can operate at large distances. Static stress changes decrease rapidly with distance but may affect nearby faults and help determine the location of future earthquakes (Harris, 1998; Freed, 2012). Both static and dynamic stress changes may raise the probability of occurrence of an earthquake by reducing its time to failure. Coulomb failure theory is one of the widely used methods to explain the static stress interactions based on the assumption that an increase of Coulomb stress promotes failure, while a decrease inhibits failure (e.g. Das and Scholz, 1981; Stein and Lisowski, 1983; Oppenheimer et al, 1988; Harris, 1998). Many investigations of Coulomb stress triggering have found that static stress change plays an important role in the production of aftershocks (Harris, 1998; Stein, 1999; Freed, 2005; Toda et al., 2011a).

The coulomb stress change ($\Delta\sigma_f$) is defined as:

$$\Delta\sigma_f = \Delta\tau + \mu(\Delta\sigma + \Delta P) \tag{2.5}$$

where $\Delta\tau$ is the shear stress change on the receiver fault (positive in the direction of slip), $\Delta\sigma$ is the normal stress change (positive for unclamping), ΔP is the pore pressure change in the fault zone, and μ is the friction coefficient (with range 0 - 1). Equation (2.5) can be re-written in terms of an effective coefficient of friction, μ', (Reasenberg and Simpson, 1992; King et al., 1994):

$$\Delta\sigma_f = \Delta\tau + \mu' \Delta\sigma \tag{2.6}$$

where $\mu' = \mu(1-B)$, and B is Skemptons coefficient with value between 0 and 1. The effective coefficient of friction mu' generally ranges from 0 to 0.8, and appears to be high for thrust faults (Lin and Stein, 2004). We assumed $\mu' = 0.8$ because the majority of focal mechanisms examined here are of reverse type. The sensitivity of our results to the assumed value of μ' is discussed below.

It has been demonstrated that positive changes of Coulomb stress as small as 0.1 bar (0.01 MPa) appear to be sufficient to trigger earthquakes (Reasenberg and Simpson, 1992). This may seem surprising because stress drops on a fault rupture surface are commonly much larger, *e.g.,* several bars to several hundred bars. The small Coulomb stress changes at distance from a rupture are important because many faults in an area may be in a critical stress condition. An earthquake on one of them (source fault) may bring others (receiver faults) closer to failure, and in some cases, trigger failure. Of course, the opposite can and does happen: in which case the Coulomb stress change on the receiver fault (equation 2.6) is negative and the fault may be stabilized.

We made two sets of Coulomb stress calculations. We first calculated Coulomb stress change on specified representative receiver faults. This approach allows us to graphically examine the 3-dimensional spatial geometry of the Coulomb stress field and compare it with the aftershock hypocenter distribution. In the second approach, we take advantage of the nearly 400 focal mechanism solutions and compute the Coulomb stress change on each nodal plane, and then examine the statistics of nodal planes with positive stress change and their spatial location.

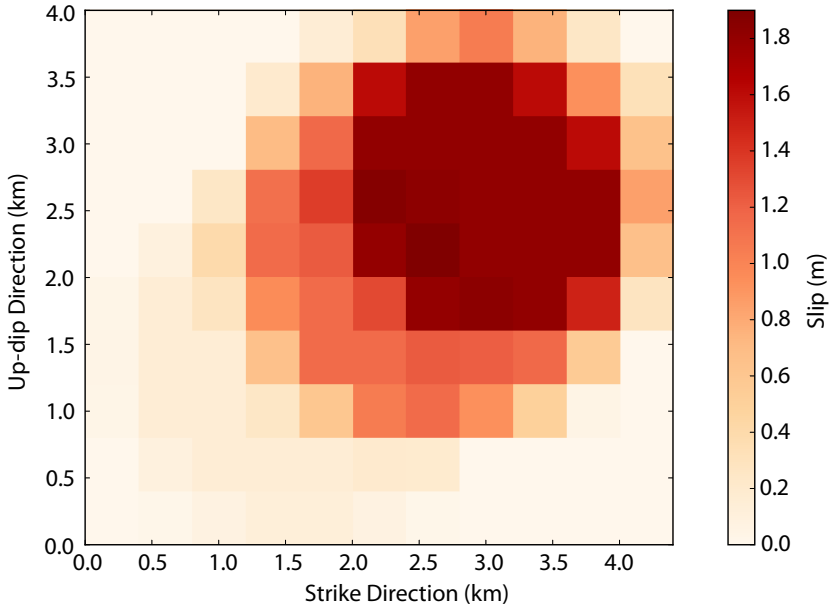

Figure 2.12: The source model derived from Chapman (2013). The fault plane is oriented with strike N28°E, dip 50°and rake 113°. The model dimension is 4.4 km along the strike direction (N28°E) by 4 km along dip direction, with grid size 0.4 km by 0.4 km. The peak slip is about 1.85 m.

The same slip model (displacement on the source fault) was used in both cases. According to Chapman (2013), the mainshock was a temporally and spatially complex rupture, comprised of 3 distinct subevents within a relatively small area. Motazedian and Ma (2014) derived similar results. The slip model (Fig. 2.12) used here for the source fault was based on the location and moment of the three subevents modeled by Chapman (2013), which is comparable to the finite fault slip model inverted from teleseismic waveforms by Hartzell et al. (2013).

Our focal mechanism solutions indicate that the aftershocks occurred on sets of fault planes with different orientations. Therefore, we cannot assume that the receiver faults have the

same strike, dip and rake as the mainshock. We defined 3 different categories of receiver faults based on the stress inversion results for different depth ranges: (1) 0 - 4 km: strike: N340°E, dip: 60°, rake: 90°; (2) 4 - 6 km: strike: N325°E, dip: 50°, rake: 90°; (3) > 6 km: strike: N30°E, dip: 50°, rake: 110°. Those three mechanisms are taken as representative of the events in each depth range. Calculations were made in an elastic half-space using the Coulomb 3.3 program (Toda et al., 2011b) with Young's modulus equal to 8×10^5 bar (8×10^4 MPa), shear modulus equal to 3.2×10^5 bar (3.2×10^4 MPa), and Poisson's ratio equal to 0.25.

Figure 2.13a shows in map view Coulomb stress change at 2 km depth on the category 1 receiver fault representing the shallow aftershocks in the main cluster and events in the northeastern group. The epicenters of earthquakes in the 0 - 4 km depth range are also plotted in Figure 2.13a. The epicenters of the shallow earthquakes correlate well with the two zones of positive Coulomb stress change at 2 km depth. This is further illustrated in Figures 2.13b and 2.13c by vertical profiles through the center of the main aftershock cluster and through the center of the northeastern aftershock group. The respective profiles show contoured Coulomb stress change and projected aftershock hypocenters lying within a 10 km wide band centered on the two profiles, and clearly indicate that lobes of positive stress change correspond to the aftershock zones. Significantly, the good match for the northeastern aftershocks indicates that the very small stress transfer imparted by the mainshock promoted failure in this zone on fault planes with orientation very different from the mainshock rupture.

The Coulomb stress calculations on receiver fault categories 2 and 3 show similar strong correlations of Coulomb stress change with the spatial distribution of aftershocks at depths

between 4 and 6 km, and greater than 6 km, respectively (Fig. 2.14 and 2.15). Considering the uncertainties in aftershock locations and details of the mainshock slip model, we expect to see some aftershocks located in the negative Coulomb stress change zones; however, there are relatively few examples of such.

A stricter calculation can be made to investigate whether the nodal planes of the aftershocks are promoted for failure by the Coulomb stress change. By resolving the Coulomb stress change on aftershock nodal planes in their rake directions, one need not make any assumptions about the receiver fault geometry. But while the shear stress on the two orthogonal nodal planes is the same, the unclamping stress is different. So, except for the special case of zero fault friction, the Coulomb stress imparted to the two nodal planes will differ, and, except under unusual circumstances, we do not know which of the two planes slipped (Hardebeck et al., 1998; Toda et al., 2011a). Because of the nodal plane ambiguity, we resolved the Coulomb stress change on both nodal planes of all 393 focal mechanisms. If we randomly select one of two nodal planes for each focal mechanism solution, 308 out of 393 events (78%) have positive stress change, and the percentage of stress increase for events in the main cluster and the northeastern cluster are 80% (286 of 358) and 63% (22 of 35) respectively. A percentage of 87% (343 out of 393) were found to have been brought closer to failure if we select the larger change from each pair of nodal planes, including 312 out of 358 (87%) for the main cluster and 31 out of 35 (89%) for the northeastern aftershocks. Figure 2.16 shows the results derived by choosing the larger Coulomb stress change from each pair of nodal planes. The majority of earthquakes in the northeastern group of aftershocks show small positive Coulomb stress change of approximately 0.2 bar (0.02 MPa). A further observation concerning these northeastern aftershocks is that 21 out of the 35 focal mechanisms show

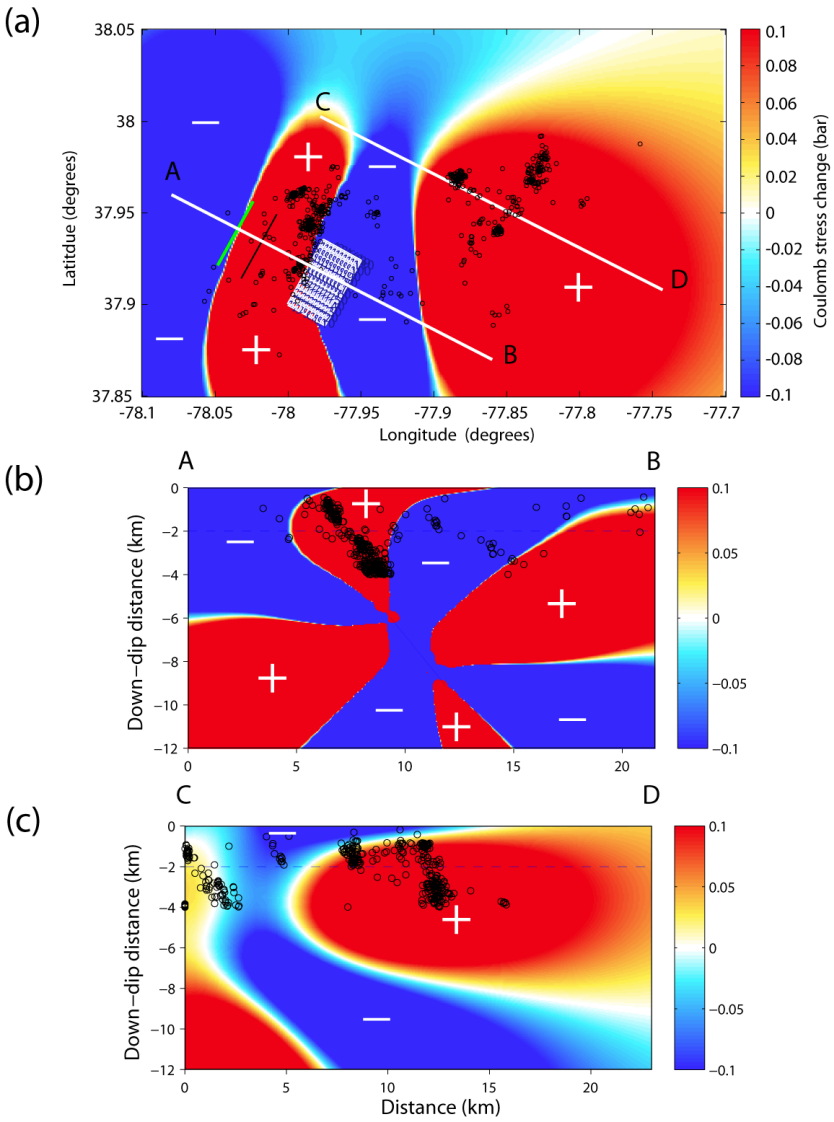

Figure 2.13: (a) Contoured values of Coulomb stress change at 2 km depth resolved on receiver fault type 1: strike: 340°, dip: 60°, and rake: 90°. The epicenters of aftershocks that occurred in the depth range 0-4 km are shown as small open circles. The projection of the source fault is shown by the rectangular grid. (b) and (c) show contoured Coulomb stress change on vertical profiles A-B and C-D, with hypocenters projected to the profile from a 10 km wide band. The plus and minus signs indicate lobes of positive and negative Coulomb stress change, respectively. Note that $\mu' = 0.8$ used here.

a positive stress change on the N-NW striking, NE-dipping nodal plane, whereas the other nodal plane shows in most cases negative stress change. This indicates that the faulting probably occurred on the NW-striking, NE-dipping planes, consistent with the geometry of the hypocenter locations (Fig. 2.9).

Figure 2.8 shows that focal mechanisms derived from aftershocks at depths greater than 4 km represent events spatially situated in the arcuate cluster that appears to halo the zone of mainshock rupture. Forty-three of the 268 focal mechanisms in this depth range (16%) had estimated Coulomb stress changes greater than 10 bars (1 MPa). The majority of events (59%) had estimated stress change between 1 and 10 bars (0.1 and 1 MPa). Due to proximity of the source fault, less than 1% of events with focal mechanisms had estimated stress change

between 0 and 1 bar. Two percent of the focal mechanisms had estimated Coulomb stress change between 0 and -1 bar (-0.1 MPa) and approximately 7% had estimated stress change between -1 and -10 bars (-0.1 and -1 MPa). There were 24 out of 268 estimates (approximately 9%) with large negative stress change estimates (less than -10 bars or -1 MPa). Those events with large negative estimates of stress change were at depths between 5.5 and 9 km, near the zone of mainshock rupture. It is likely that a small error in hypocenter location or in the modeling of the fault slip distribution is responsible for the negative Coulomb stress change estimates for some of the aftershocks near the mainshock rupture.

Changing the assumed value of μ' will reduce the contribution of the normal stress change to the Coulomb stress change (equation 2.6) and may perturb the estimated pattern of aftershock triggering. We examined the sensitivity of the Coulomb stress estimates to the assumed effective coefficient of friction μ'. We recalculated the Coulomb stress changes on

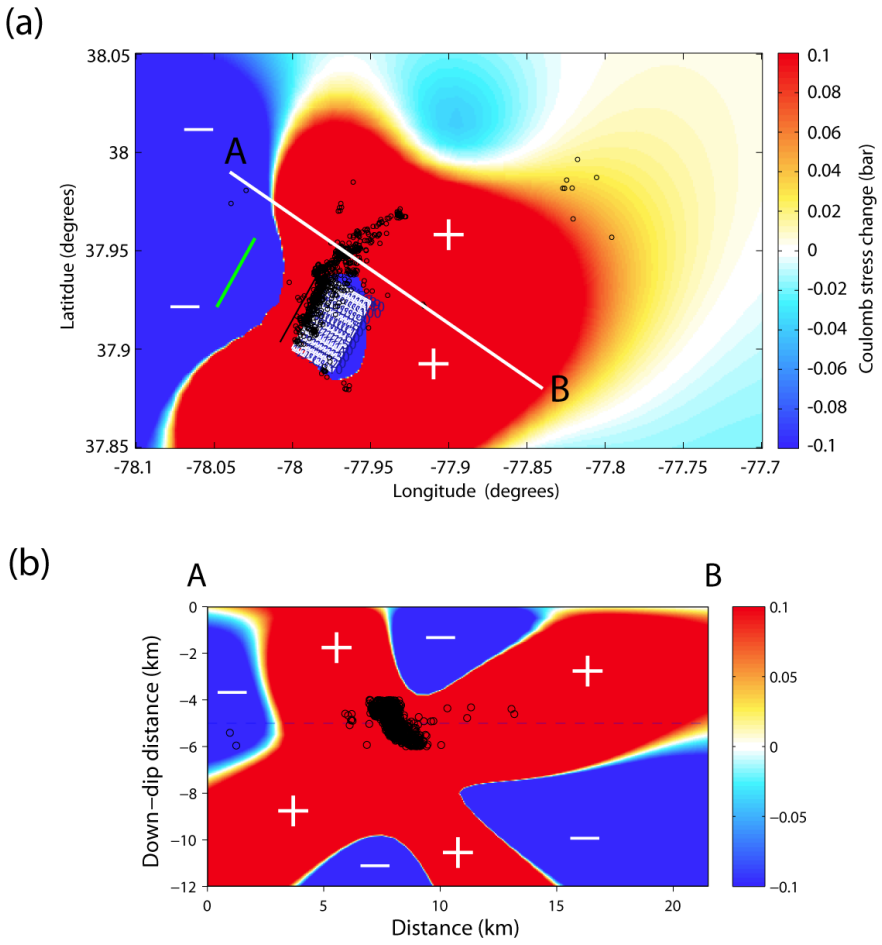

Figure 2.14: (a) Contoured values of Coulomb stress change at 5 km depth resolved on receiver fault type 2: strike: 325°, dip: 50°, and rake: 90°. The epicenters of aftershocks that occurred in the depth range 4-6 km are shown as small open circles. The projection of the source fault is shown by the rectangular grid. (b) Contoured Coulomb stress change on vertical profile A-B, with hypocenters projected to the profile from a 10 km wide band. The plus and minus signs indicate lobes of positive and negative Coulomb stress change, respectively. Note that $\mu' = 0.8$ used here.

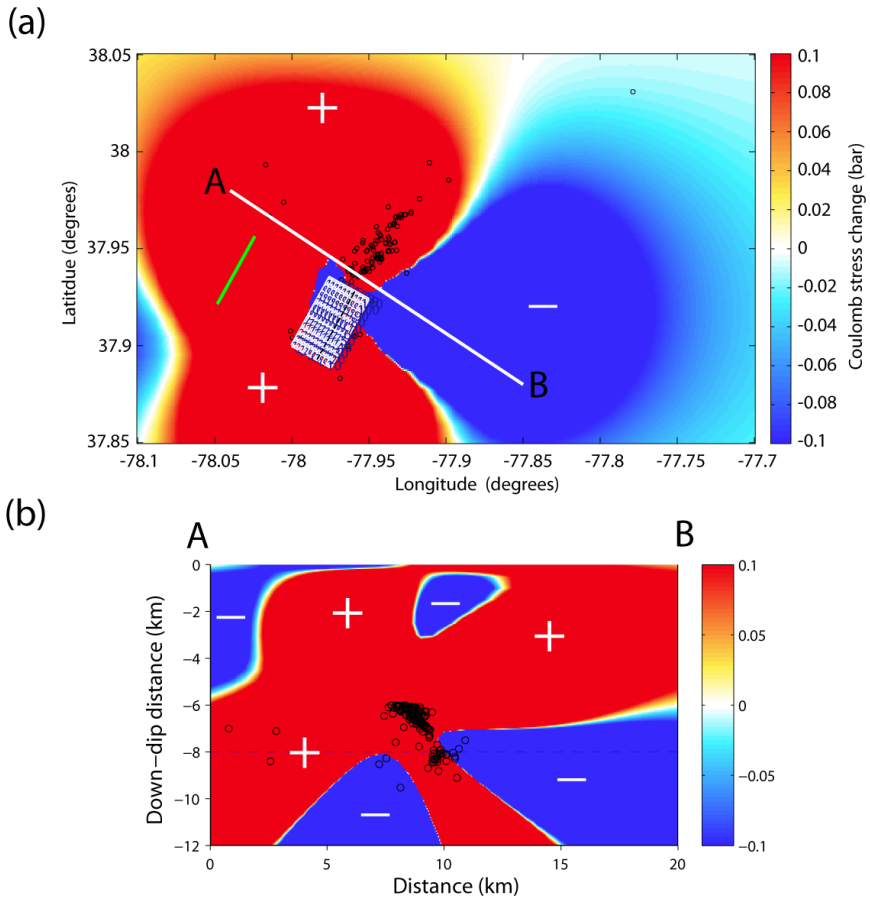

Figure 2.15: (a) Contoured values of Coulomb stress change at 8 km depth resolved on receiver fault type 3: strike: 30°, dip: 50°, and rake: 110°. The epicenters of aftershocks that occurred at focal depths greater than 6 km are shown as small open circles. The projection of the source fault is shown by the rectangular grid. (b) Contoured Coulomb stress change on vertical profile A-B, with hypocenters projected to the profile from a 10 km wide band. The plus and minus signs indicate lobes of positive and negative Coulomb stress change, respectively. Note that $\mu' = 0.8$ used here.

focal mechanism nodal planes assuming moderate ($\mu' = 0.4$) and low ($\mu' = 0.2$) friction. Comparison of the results based on smaller μ' with the calculation that assumes $\mu' = 0.8$ shows very minor changes. With $\mu' = 0.4$, we find that 86% of the events (338 out of 393) have positive Coulomb stress change if we select the maximum value of the two nodal planes; this percentage changes to 85% for $\mu' = 0.2$. And if we randomly select nodal planes, the percentages of stress increase changes to 81% and 84% for $\mu' = 0.4$ and $\mu' = 0.2$ respectively.

2.3 Discussion and Conclusions

This study of the aftershock sequence of the M_W 5.7, 23 August, 2011 Mineral, Virginia, earthquake resolved spatial details within the previously recognized tabular main aftershock zone and gave us some insights concerning the stress field operative during, and perhaps prior to, the early phase of the aftershock sequence. The temporal behavior of the aftershocks in the 129 day time period from 25 August, 2011 through 31 December, 2011 follows the modified Omori's law with a p-value of 1.085±0.058, and a Gutenberg-Richter b-value of 0.864±0.013. The detection threshold of the monitoring network during this time was approximately $M_d{}^*$ = -0.4, where $M_d{}^*$ is an indirect estimate of $m_{b(Lg)}$. The aftershock sequence statistics are within the range of typical aftershock sequences reported in the literature.

The main aftershock cluster is approximately 1 km thick and exhibits gross strike and dip in agreement with the mainshock fault plane. The majority of the focal mechanisms are of reverse type. However, the near-planar arrangement of the aftershocks in the main cluster belies the fact that the majority of them exhibit nodal planes with orientations significantly different from the mainshock. An important observation is the fact that this variability of the

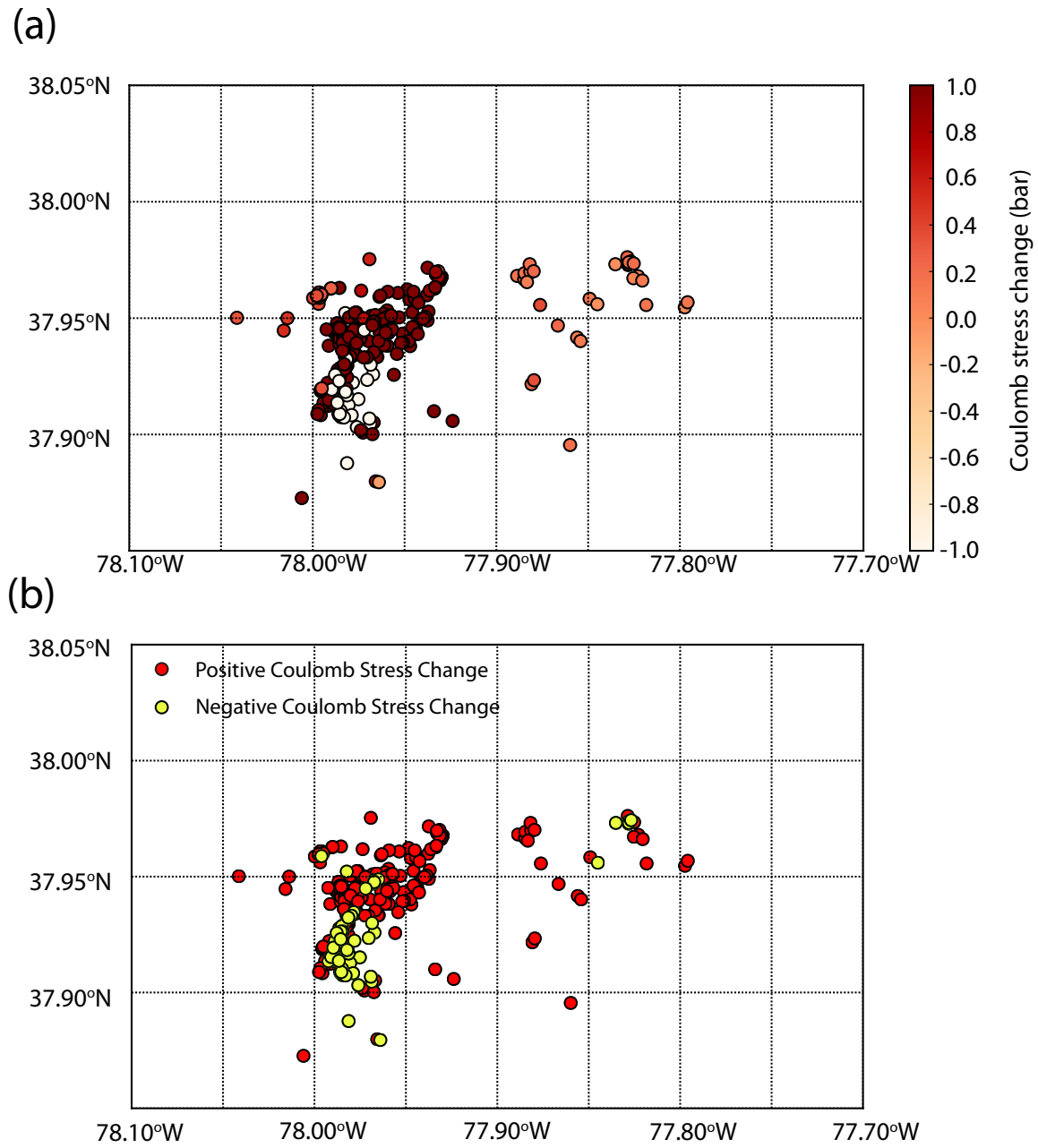

Figure 2.16: Coulomb stress change resolved on focal mechanism nodal planes. (a) Selection of the most positive Coulomb stress change value from each pair of nodal planes: positive stress change percentage is 87.3% (343 events). (b) Selection of the most positive Coulomb stress change value from each pair of nodal planes: symbols show positive and negative values. Note that $\mu' = 0.8$.

main cluster focal mechanisms is not random, but depends on the location of the aftershocks with respect to the mainshock. Shallow aftershocks mostly exhibit north-northwest trending nodal planes and invert to yield a well-constrained best-estimate maximum principle stress direction that is sub-horizontal, trending approximately N80°E. But most of the main cluster aftershocks occurred in the depth range 4 to 6 km. In contrast to the shallower shocks, those mostly reverse events show a 90 degree range of nodal plane trend, from approximately N-S to E-W. This large variability results in large uncertainty in the stress field inversion for the 4-6 km depth range containing by far the majority of main cluster events: the best estimate for the maximum principle stress direction for that depth range is sub-horizontal and trends N55°E, but the trend is uncertain by approximately 70 degrees at the 95% confidence level. The 25 degree difference in σ_1 azimuth found for the events in the 4-6 km depth range and that found for the shallower aftershocks is clearly insignificant given the uncertainties.

The relatively few (36) aftershock focal mechanisms at depths comparable to the mainshock rupture (> 6 km) show nodal planes that are, on average, similar to the mainshock. They invert to yield a sub-horizontal maximum principle stress direction trending ~N100°E. The approximate N100°E trend of σ_1 for the deep aftershocks agrees with the N103°E azimuth and sub-horizontal plunge of the mainshock focal mechanism P-axis. This suggests that the apparent 20 degree rotation (N80°E for events less than 4 km deep, versus N100°E for events deeper than 6 km) may be significant. A rotation of the ambient stress field with depth is further supported by the fact that very small positive static Coulomb stress change triggered shallow (5 km and less) aftershocks 10-20 km to the northeast of the main aftershock cluster, systematically on faults with a very different orientation from that of the mainshock. Furthermore, inversion of the focal mechanisms of those northeastern aftershocks yielded a

stress field orientation very similar to that derived from the shallow aftershocks (<4 km deep) in the main aftershock cluster. Our results suggest that the N-NW trending faults at shallow depths in both the main cluster and those to the northeast were in a near-critical stress condition prior to the mainshock, being optimally oriented for slip in an ambient stress field with σ_1 sub-horizontal and trending approximately N80°E. They were triggered to failure by approximately 0.2 bar (0.02 MPa) positive Coulomb stress transfer from the mainshock, which ruptured at greater depth and apparently in a different (rotated) stress regime. There are no mapped faults with this N-NW trending orientation in the vicinity of the main aftershock cluster or the northeastern cluster. However, early Mesozoic diabase dikes share the N-NW trend of the shallow aftershock nodal planes (Shah et al., 2015). Also, N-NW is the dominant trend of joints in this area, which have a major influence on drainage patterns (Burton et al, 2015). We note that there is an absence of shallow aftershocks located to the south and southwest of the mainshock, where they would be expected due to Coulomb stress transfer (Fig. 2.13a). This may indicate a lack of favorably oriented faults in that area, or perhaps is related to the rupture directivity of the mainshock.

The locations of the aftershocks and their focal mechanisms in the depth range 4-6 km in the main aftershock cluster point to the role of static and possibly dynamic stress changes near the mainshock fault rupture. The location of the events in a rough quarter-circle, up-dip and to the northeast of the rupture zone, reflects the direction of mainshock rupture propagation. The nearby I-64 reflection profile does not suggest a structural explanation for the aftershocks in the 4-6 km depth range (Pratt et al., 2015). The concentration of aftershocks and the diversity of their nodal plane orientations within this aftershock halo is likely because positive static Coulomb stress changes are largest just outside the zone of fault

rupture, thus promoting rupture on other faults that are less than optimally oriented in the ambient stress field. The location of the aftershocks in the direction of forward directivity may possibly be due to lingering effects of dynamic stresses operative during fault rupture and elastic wave propagation. Perhaps poroelastic effects in a permeable solid with pore fluids persist long after the seismic waves have passed.

References

Allen, R. (1982). Automatic phase pickers: their present use and future prospects, *Bull. Seismol. Soc. Am.* **72**, S225-S242.

Bollinger, G. A. (1969). Seismicity of the central Appalachian states of Virginia, West Virginia, and Maryland 1758 through 1968, *Bull. Seismol. Soc. Am.* **59**, 2103-2111.

Bollinger, G. A. (1973a). Seismicity and crustal uplift in the southeastern United States, *Am. J. Sci.* **273-A**, 396-408.

Bollinger, G. A. (1973b). Seismicity of the southeastern United States, *Bull. Seismol. Soc. Am.* **63**, 1785-1808.

Bollinger, G.A., M. C. Chapman and T.P. Moore (1980). Central Virginia regional seismic network: Crustal structure in central and southwestern Virginia, *NUREG/CR-1217*, U.S. Nuclear Regulatory Commission, Washington, D.C., 187 p.

Bollinger, G. A., A. C. Johnston, P. Talwani, L. T. Long, K. M. Shedlock, M. S. Sibol,

and M. C. Chapman (1991). Seismicity of the southeastern United States; 1698 to 1986, in *Neotectonics of North America*, D. B. Slemmons, E. R. Engdahl, M. D. Zoback, and D. D. Blackwell (Editors), Geological Society of America, 291-308.

Burton, W.C., R.W. Harrison, D.B. Spears, N.H. Evans and S. Mahan (2015). Geologic framework and evidence for neotectonics in the epicentral area of the 2011 Mineral, Virginia, earthquake, in *The 2011 Mineral, Virginia, Earthquake and its Significance for Seismic Hazards in Eastern North America*, Horton, J.W., Jr., Chapman, M.C., and Green, R.A., (Editors), Geological Society of America Special Paper 509, doi:10.1130/2015.2509(02), 345-376.

Chapman, M. C. (2013). On the rupture process of the 23 August 2011 Virginia earthquake, *Bull. Seismol. Soc. Am.* **103**, 613-628.

Chapman, M.C. (2015). Magnitude, recurrence interval, and near-source ground-motion modeling of the Mineral, Virginia, earthquake of 23 August 2011, in *The 2011 Mineral, Virginia, Earthquake and its Significance for Seismic Hazards in Eastern North America*, Horton, J.W., Jr., Chapman, M.C., and Green, R.A., (Editors), Geological Society of America Special Paper 509, doi:10.1130/2015.2509(02), 27-46.

Das, S., and C. H. Scholz (1981). Off-fault aftershock clusters caused by shear stress increase? *Bull. Seismol. Soc. Am.* **71**, 1669-1675.

Davenport, K. K., J. A. Hole, D. A. Quiros, L. D. Brown, M. C. Chapman, L. Han, and W. D. Mooney (2015). Aftershock imaging using a dense seismometer array (AIDA) after the 2011 Mineral, Virginia earthquake, in *The 2011 Mineral, Virginia, Earthquake and*

its Significance for Seismic Hazards in Eastern North America, Horton, J.W., Jr., Chapman, M.C., and Green, R.A., (Editors), Geological Society of America Special Paper 509, doi:10.1130/2015.2509(15), 273-283.

Ebel, J. E. (2009). Analysis of aftershock and foreshock activity in stable continental regions: Implications for aftershock forecasting and the hazard of strong earthquakes, *Seismol. Res. Lett.* **80**, 1062-1068.

Freed, A. M. (2005). Earthquake triggering by static, dynamic, and postseismic stress transfer, *Ann. Rev. Earth Planet. Sci.* **33**, 335-367.

Freed, A. M. (2012). Earthquakes: Casting stress shadows, *Nature* **5**, 371-372.

Gomberg, J., P. Bodin, and P. A. Reasonberg (2003). Observing earthquakes triggered in the near field by dynamic deformations, *Bull. Seismol. Soc. Am.* **93**, 118-138.

Gutenberg, R., and C. F. Richter (1944). Frequency of earthquakes in California, *Bull. Seismol. Soc. Am.* **34**, 185-188.

Hardebeck, J. L., and A. J. Michael (2006). Damped regional-scale stress inversions: Methodology and examples for southern California and the Coalinga aftershock sequence, *J. Geophys. Res.*, **111**, B11310, doi 10.1029/2005JB004144.

Hardebeck, J. L., J. N. Julie and H. Egill (1998). The static stress change triggering model: Constraints from two southern California aftershock sequences, *J. Geophys. Res.*, **103**, 24427-24437.

Harris, R. A. (1998). Introduction to special section; stress triggers, stress shadows, and implications for seismic hazard, *J. Geophys. Res.* **103**, 24347-24358.

Hartzell, S., C. Mendoza, and Y. Zeng (2013). Rupture model of the 2011 Virginia, earthquake from teleseismic and regional waveforms, *Geophys. Res. Lett.* **40**, 5665-5670.

Hauksson, E. (1994). State of stress from focal mechanisms before and after the 1992 Landers earthquake sequence, *Bull. Seismol. Soc. Am.* **84**, 917-934.

Heller, M.J. and A.M. Carter (2015). Residential property damage in the epicentral area of the Mineral, Virginia, earthquake of 23 August 2011, in *The 2011 Mineral, Virginia, Earthquake and its Significance for Seismic Hazards in Eastern North America*, Horton, J.W., Jr., Chapman, M.C., and Green, R.A., (Editors), Geological Society of America Special Paper 509, doi:10.1130/2015.2509(10), 173-188.

Herrmann, R.B. (2011). St. Louis University Earthquake Center website: `http://www.eas.slu.edu/eqc/eqc20110823.html` (last accessed January, 2015).

Horton, J.W., Jr., M.C. Chapman, and R.A. Green (2015a). The 2011 Mineral, Virginia, earthquake, and its significance for seismic hazards in eastern North AmericaOverview and synthesis, in *The 2011 Mineral, Virginia, Earthquake and its Significance for Seismic Hazards in Eastern North America*, Horton, J.W., Jr., Chapman, M.C., and Green, R.A., (Editors), Geological Society of America Special Paper 509, doi:10.1130/2015.2509(01), 1-26.

Horton, J.W., Jr., A.K. Shah, D.E. McNamara, S. L. Snyder and A.M. Carter (2015b). Aftershocks illuminate the 2011 Mineral, Virginia, earthquake causative fault zone and nearby

active faults, in *The 2011 Mineral, Virginia, Earthquake and its Significance for Seismic Hazards in Eastern North America*, Horton, J.W., Jr., Chapman, M.C., and Green, R.A., (Editors), Geological Society of America Special Paper 509, doi:10.1130/2015.2509(14), 253-272.

Ishimoto, M., and K. Iida (1939). Observations of earthquakes registered with the micro-seismograph constructed recently, *Bull. Earthq. Res. Inst.* **17**, 443-478.

Kim, W., and M. Chapman (2005). The 9 December 2003 central Virginia earthquake sequence: A compound earthquake in the Central Virginia Seismic Zone, *Bull. Seismol. Soc. Am.* **95**, 2428-2445.

King, G., R. S. Stein, and J. Lin (1994). Static stress changes and the triggering of earthquakes, *Bull. Seismol. Soc. Am.* **84**, 935-953.

Kisslinger, C., and L. M. Jones (1991). Properties of aftershocks in southern California, *J. Geophys. Res.* **96**, 11947-11958.

Lahr, J. C. (1999). HYPOELLIPSE: A computer program for determining local earthquake hypocentral parameters, magnitude, and first-motion pattern, U.S. Geol. Surv. Open-File Rept. 99-23, version 1.1, 119 pp., software, available at `http://pubs.usgs.gov/of/1999/ofr990023/` (last accessed December, 2014).

Lin, J., and R. S. Stein (2004). Stress triggering in thrust and subduction earthquakes and stress interaction between the southern San Andreas and nearby thrust and strike-slip faults, *J. Geophys. Res.* **109**, no. B02303, doi: 10.1029/2003JB002607.

Martnez-Garzn, P., Kwiatek, G., Ickrath, M. and M. Bohnhoff (2014). MSATSI: A MATLAB package for stress inversion combining solid classic methodology, a new simplified user-handling and a visualization tool, *Seismol. Res. Lett.* **85**, 896-904.

McNamara, D. E., Benz, H. M., Herrmann, R. B., Bergman, E. A., Earle, P., Meltzer, A., Withers, M., and M. Chapman (2014). The Mw 5.8 Mineral, Virginia, earthquake of August 2011 and aftershock sequence: constraints on earthquake source parameters and fault geometry, *Bull. Seismol. Soc. Am.* **104**, 40-54.

Mendoza, C. and S. H. Hartzell (1988). Aftershock patterns and main shock faulting, *Bull. Seismol. Soc. Am.* **78**, 1438-1449.

Michael, A. J., W. L. Ellsworth and D. H., Oppenheimer (1990). Coseismic stress change induce by the 1989 Loma Prieta California earthquake, *Geophys. Res. Lett.*, **17**, 1441-1444.

Motazedian D., S. Ma (2014). A review study of the source parameters of the August 2011 Mw 5.7 Virginia earthquake, *Bull. Seismol. Soc. Am.* **104**, 2611-2618.

Nuttli, O.W. (1973). Seismic wave attenuation and magnitude relations for eastern North America, *J. Geophys. Res.* **78**, 876-885.

Oppenheimer, D. H., P. A. Reasenberg, and R. W. Simpson (1988). Fault plane solutions for the 1984 Morgan Hill, California, earthquake sequence; evidence for the state of stress on the Calaveras Fault, *J. Geophys. Res.* **93**, 9007-9026.

Pratt, T. L., C. oruh, J. K. Costain, and L. Glover III (1988). A geophysical study of the Earths crust in central Virginia: Implications for Appalachian crustal structure, *J. Geophys.*

Res. **93**, 6649-6667.

Pratt, T. L., J. W. Horton, Jr., D. B. Spears, A.K. Gilmer and D. E. McNamara (2015). The 2011 Virginia Mw 5.8 earthquake: Insights from seismic reflection imaging into the influence of older structures on eastern U.S. seismicity, in *The 2011 Mineral, Virginia, Earthquake and its Significance for Seismic Hazards in Eastern North America*, Horton, J.W., Jr., Chapman, M.C., and Green, R.A., (Editors), Geological Society of America Special Paper 509, doi:10.1130/2015.2509(16), 285-294.

Reasenberg, P. A., and R. W. Simpson (1992). Response of regional seismicity to the static stress change produced by the Loma Prieta earthquake, *Science* **255**, 1687-1690.

Shah, A. J., J. W. Horton Jr., W. C. Burton, D. B. Spears and A. K. Gilmer (2015). Subsurface geologic features of the 2011 central Virginia earthquakes revealed by airborne geophysics, in *The 2011 Mineral, Virginia, Earthquake and its Significance for Seismic Hazards in Eastern North America*, Horton, J.W., Jr., Chapman, M.C., and Green, R.A., (Editors), Geological Society of America Special Paper 509, doi:10.1130/2015.2509(17), 295-304.

Snoke, J. A. (2009). FOCMEC: FOCal MEChanisms Determinations Manual., `http://ds.iris.edu/pub/programs/focmec/` (last accessed December 2014).

Snoke, J. A., J. W. Munsey, A. C. Teague, and G. A. Bollinger (1984). A program for focal mechanism determination by combined use of polarity and SV-P amplitude ratio data, *Earthq. Notes* **55**, no. 3, 15.

Stein, R. (1999). The role of stress transfer in earthquake occurrence, *Nature* **402**, 605-609.

Stein, R. S., and M. Lisowski (1983). The 1979 Homestead Valley earthquake sequence, California; control of aftershocks and postseismic deformation, *J. Geophys. Res.* **88**, 6477-6490.

Stover, C. W. and J. L. Coffman (1993). Seismicity of the United States, 1568-1989 (Revised), U.S. Geological Survey Professional Paper 1527, 418 p.

Taber, S. (1913). Earthquakes in Buckingham county, Virginia, *Bull. Seismol. Soc. Am.* **3**, 124-133.

Toda, S., J. Lin, and R. S. Stein (2011a). Using the 2011 Mw 9.0 off the Pacific coast of Tohoku earthquake to test the Coulomb stress triggering hypothesis and to calculate faults brought closer to failure, *Earth Planets Space*, **63**, 725-730.

Toda, S., R. S. Stein, V. Sevilgen, and J. Lin (2011b). Coulomb 3.3 Graphic-Rich Deformation and Stress-Change Software for Earthquake, Tectonic, and Volcano Research and Teaching User Guide, United States Geological Survey Open File Report 2011-1060, 63 p., available at http://pubs.usgs.gov/of/2011/1060/.

Utsu, T. (1961). A statistical study of the occurrence of aftershocks, *Geophysical Magazine* **30**, 521-605.

Utsu, T., Y. Ogata, and R. S. Matsuura (1995). The centenary of the Omori formula for a decay law of aftershock activity, *J. Phys. Earth*, **43**, 1-33.

Waldhauser, F. (2001). HYPODD A program to compute double-difference hypocenter locations, U.S. Geol. Surv. Open-File Rept. 01-113, 25 pp.

Waldhauser, F., and W. L. Ellsworth (2000). A double-difference earthquake location algorithm: Method and application to the northern Hayward fault, California, *Bull. Seismol. Soc. Am.* **90**, 1353-1368.

Wells, D., J. A. Egan, D. G. Murphy and T. P. Paret (2015). Ground shaking and structural response of the Washington Monument during the 2011 Mineral, Virginia, earthquake, in *The 2011 Mineral, Virginia, Earthquake and its Significance for Seismic Hazards in Eastern North America*, Horton, J.W., Jr., Chapman, M.C., and Green, R.A., (Editors), Geological Society of America Special Paper 509, doi:10.1130/2015.2509(12), 199-234.

Wessel, P., and W. Smith (1991). Free software helps display data, *Eos Trans. AGU* **72**, 445-446.

Wiemer, S., and K. Katsumata (1999). Spatial variability of seismicity parameters in aftershock zones, *J. Geophys. Res.* **104**, 13135-13151.

Withers, M., R. Aster, C. Young, J. Beiriger, M. Harris, S. Moore, and J. Trujillo (1998). A comparison of selected trigger algorithms for automated global seismic phase and event detection, *Bull. Seismol. Soc. Am.* **88**, 95-106.

Wu, Q., M. C. Chapman, and J. N. Beale (2014). Automatic detection and hypocenter determination of the August 23, 2011 Mineral, Virginia, earthquake aftershock sequence, *Seismol. Res. Lett.* **85**, 241.

Zoback, M.L., (1992). First- and second-order patterns of stress in the lithosphere: The World Stress Map project. *J. Geophys. Res.* **97**, 11703-11728.

Chapter 3

Near-source Geometrical Spreading in the Central Virginia Seismic Zone[†]

[†]**Citation: Wu, Q.**, M. C. Chapman, J. N. Beale and S. Shamsalsadati (2016). Near-source geometrical spreading in the central Virginia seismic zone determined from the aftershocks of the 2011 Mineral, Virginia, earthquake, *Bull. Seismol. Soc. Am.* **106**, 943-955.

Abstract

We used aftershocks of the 2011 Mineral, Virginia, earthquake to study geometrical spreading at hypocentral distances less than 60 km in the central Virginia seismic zone (CVSZ). Sixty-nine aftershocks occurring from 25 August, 2011 through 24 December, 2011 provided the data. We used the coda-normalization method to estimate the attenuation coefficient associated with geometrical spreading. We filtered the time domain signals in several octave-wide frequency bands and examined attenuation of peak S-wave amplitude in the frequency range 1.0 - 30.0 Hz. Amplitude was assumed to decrease as a function of hypocenter distance R according to $R^{-\gamma}$. The coefficient of attenuation γ, was examined for the 3 component S-wave amplitudes, with corrections for SH and SV radiation patterns.

We observe no systematic frequency dependence of γ. The coefficient of attenuation for the radial and transverse components, assuming infinite Q, derived as a weighted mean over the entire range of frequencies (1 to 30 Hz), are both 1.51±0.05. The weighted mean value of the attenuation coefficient on the vertical component over the same range of frequencies is 1.45±0.05, slightly less than for the horizontal components. We corrected the data assuming three Q models. The estimated geometrical spreading coefficients are in the range of 1.30-1.46, depending on assumed Q model and component, only slightly less than the estimates of γ determined assuming infinite Q. The estimated attenuation coefficients differ significantly from the value of 1.0 expected for a whole space. The results for the horizontal components are in agreement with previous full wavefield modeling. However, the observed vertical component attenuation is substantially less than that predicted by the synthetics. The depths of the earthquakes are less than 8 km, so these results may not be representative of

geometrical spreading in parts of eastern North America where earthquakes occur at greater depths.

3.1 Introduction

The observational data for earthquakes in the eastern United States (EUS) are sparse in the critical near-source distance range for strong ground motion. Few seismic stations operate in most areas of the EUS, and station spacing is several tens of kilometers or more over most of the region. As a result, data for the development of ground motion prediction models consists largely of recordings made at distances in excess of 120 km, beyond the range at which significant damage to structures usually occurs in the case of moderate earthquakes.

Most current ground motion prediction models for eastern North America (ENA) are based to some degree on the stochastic model (Hanks and McGuire, 1981; Boore, 1983; Atkinson and Boore, 1995; Toro et al., 1997; Boore, 2003, Atkinson and Boore, 2006). The target ground acceleration spectrum in the stochastic model is comprised of three main components: the source spectrum, the path effect, and the site response. The path effect involves two physical processes: geometrical spreading of the S waves and the Lg group and frequency-dependent attenuation due to anelastic absorption and/or scattering. At near-source distances, the path effect is mostly dominated by geometrical spreading, whereas anelastic attenuation becomes important at larger distances and at higher frequencies. Independent estimation of the parameters defining geometrical spreading and anelastic attenuation is difficult, particularly at larger hypocentral distances, because of trade-offs between the parameters (Atkinson and Mereu, 1992). In the hypocentral distance range of interest here (to approximately 60

km), geometrical spreading dominates the path effect, and is the more important of the two processes at frequencies of engineering concern. In that distance range uncertainty in the value of Q does not have large effects on estimates of geometrical spreading, as we demonstrate below.

Empirical studies using data primarily from earthquakes in southeastern Canada and the northeastern United States report relatively rapid decay ($R^{-1.3}$) of ground motion amplitude with hypocenter distance R, for R less than approximately 70 km. Less rapid decay ($R^{-0.5}$) is observed at distances exceeding approximately 120 km and a zone of no attenuation, or increasing amplitude with distance, in the intervening distance range has been documented (Atkinson and Mereu, 1992; Atkinson, 2004; Atkinson and Boore, 2014). The flattening of apparent attenuation and/or increase in amplitude observed from approximately 70 to 120 km has been attributed to large amplitude post-critical reflections from the mid-lower crust and Moho (Burger et al., 1987, Atkinson, 2004).

Geometrical spreading is well-constrained by observations at distances beyond approximately 120 km where Lg waves dominate the wavefield, but closer to the epicenter the direct S-wave arrival and S-wave reflections off internal crustal interfaces and the Moho are important and geometrical spreading is more complex. The amplitude behavior at distances less than 60 km is not well-constrained by observations in the EUS, and the data that are available show a large amount of scatter. Theoretically, much of this scatter of near-source amplitudes should be attributable to the effects of the S-wave radiation pattern. Several studies have examined attenuation in the near-source distance range. Atkinson (2004) investigated Fourier spectral amplitudes of 186 earthquakes in southeastern Canada and in the northeastern United States

and determined a geometrical spreading of $R^{-1.3}$ in the distance range 20-70 km. Some other previous studies reported a geometrical spreading of R^{-1} at local distances: *e.g.*, Zandieh and Pezeshk (2010) in the New Madrid seismic zone. Atkinson et al. (2011) examined ground-motion attenuation within approximately 30 km for 12 shallow earthquakes of magnitude M_N 1.0-3.1 that occurred near Sudbury, Ontario and found that at high frequencies (3-10 Hz), the ground motions decay as $R^{-1.3}$ for the horizontal component, while the vertical-component motion appears to decay as $R^{-1.1}$. Atkinson and Boore (2014) assumed that the Q model calculated from regional observations (> 150 km) also applies to near-source distance (< 50 km) and separated Q and geometrical spreading for events of **M** 3.5-5.8 in ENA. They found an effective geometrical spreading rate of $R^{-1.3}$ within 50 km of the source and $R^{-0.5}$ at greater distances. Frankel (2015) quantified the decay of S-wave amplitude at distances of 10-80 km in the Charlevoix, Quebec area using coda-normalized S-wave amplitudes from 7 earthquakes and found that the decay rate is steeper at low frequency (1 Hz) than at high frequency (14 Hz). He suggested that this result is a consequence of the radiation pattern and rupture directivity. Theoretical studies suggest that ground motion attenuation depends on focal depth, source mechanism and crustal velocity models. Synthetic simulation by Chapman and Godbee (2012) demonstrated that the apparent geometrical spreading is substantially steeper than R^{-1} and is dependent on focal mechanisms. Both empirical and numerical studies indicate that an assumption of simple body wave geometrical spreading of R^{-1} for a homogeneous whole space may not be appropriate for modeling ground motion in all cases.

The 23 August, 2011, M_W 5.8 earthquake in central Virginia was felt over most of the eastern seaboard of the United States. The reverse-faulting earthquake, with a compound rupture

process consisting of at least three prominent subevents, occurred in the central Virginia seismic zone (CVSZ), which has a long history of moderate earthquake activity (Taber, 1913; Bollinger, 1969, 1973a, b; Kim and Chapman, 2005; Chapman, 2013). Detailed studies of the aftershock sequence provided accurate hypocenter locations and focal mechanism solutions of the aftershocks (McNamara et al., 2014a; Wu et al., 2015). McNamara et al. (2014b) determined the frequency-dependent attenuation of the crust for the CVSZ and the surrounding EUS region by analyzing S and L_g waves recorded from the 2011 Mineral, Virginia earthquake and its aftershock sequence, and found that Q in the EUS is high at both local and regional distances. They found an average regional L_g Q described by $Q(f) = 751(\pm 39.0) f^{0.28(\pm 0.054)}$ in the distance range 250-1100 km, and an average S-wave Q described by $Q(f) = 230(\pm 26) f^{0.51(\pm 0.11)}$ at distances less than 250 km. Dreiling and Mooney (2015) measured the near-source attenuation of S-wave amplitude in the CVSZ using 40 aftershocks recorded by 30 stations deployed along a profile extending approximately 60 km to the northeast of the mainshock epicenter (AIDA profile). They directly measured the peak amplitudes of the trace envelopes without accounting for the source effect and site response and observed frequency-dependent decay of S-wave amplitudes with hypocentral distance R, as $R^{-0.8}$ for 1-2 Hz, $R^{-0.9}$ for 2-4 Hz, $R^{-1.05}$ for 4-8 Hz and $R^{-1.15}$ for 8-16 Hz.

In this study, we also examine the S-wave attenuation at hypocentral distances less than 60 km in the CVSZ using the aftershocks of the 2011 earthquake, recorded by both the AIDA profile stations and 32 additional stations surrounding the mainshock epicenter. The analysis makes use of 3-component recordings at high frequencies collected from 69 aftershocks with $m_{b(Lg)}$ ranging from 1.8 to 3.6. We use the coda-normalization method to account for the earthquake source and recording site response. We estimate the attenuation coefficient γ

for the radial, transverse and vertical component peak S-wave amplitudes in 10 octave-wide frequency bands: 1-2 Hz, 1.4-2.8 Hz, 1.875-3.75 Hz, 2.5-5 Hz, 3.375-6.75 Hz, 4.5-9 Hz, 6-12 Hz, 8.4-16.8 Hz, 11.25-22.5 Hz and 15-30 Hz. We make corrections for the source radiation pattern using focal mechanism solutions. We also investigate the effects of the window selection for the measurements of amplitudes and the frequency-dependent characteristics of the estimates of the coefficient of attenuation, including the sensitivity of the estimates to uncertainties concerning Q.

3.2 Data

Figure 3.1 shows the locations of seismic stations and earthquakes used in this study. The stations were deployed with two objectives. Thirty stations (triangles in Figure 3.1) were deployed by Virginia Tech, Cornell University and the U.S. Geological Survey (USGS) along a 60 km northeast-trending profile extending from near the mainshock epicenter to near Fredericksburg, Virginia, to study velocity structure and attenuation (Dreiling and Mooney, 2015; Davenport et al., 2015). These stations are referred to as the AIDA (Aftershock Imaging with Dense Arrays) profile, and consisted of 3-component, 4-Hz geophones recorded at 100 samples/s. These instruments operated from 1 September through 9 September, 2011. Additionally, 32 off-profile stations (shown as squares in Figure 3.1) were deployed by different groups including the University of Memphis, Virginia Tech, Lehigh University, the USGS, and the Incorporated Research Institutions for Seismology (IRIS), to locate aftershocks and determine focal mechanisms. Some of those stations operated for more than 1 year. The off-profile instruments were a mixture of short-period (2 Hz) and low and high-gain broadband

instruments, with data sampling at 100 or 200 samples/s, depending on station. Those two networks together provided abundant data to study the behavior of S-wave amplitude decay over a range of hypocentral distance from approximately 3 to 50 km in the CVSZ. Note that there is an approximately 6-km gap on the AIDA profile due to a reservoir (Lake Anna). Also note that some of the AIDA stations to the northeast of the profile were deployed along a road, which severely limited their data due to traffic noise. We carefully selected traces with good signal-to-noise ratio by visual inspection to avoid possible contamination or artifacts caused by traffic noise.

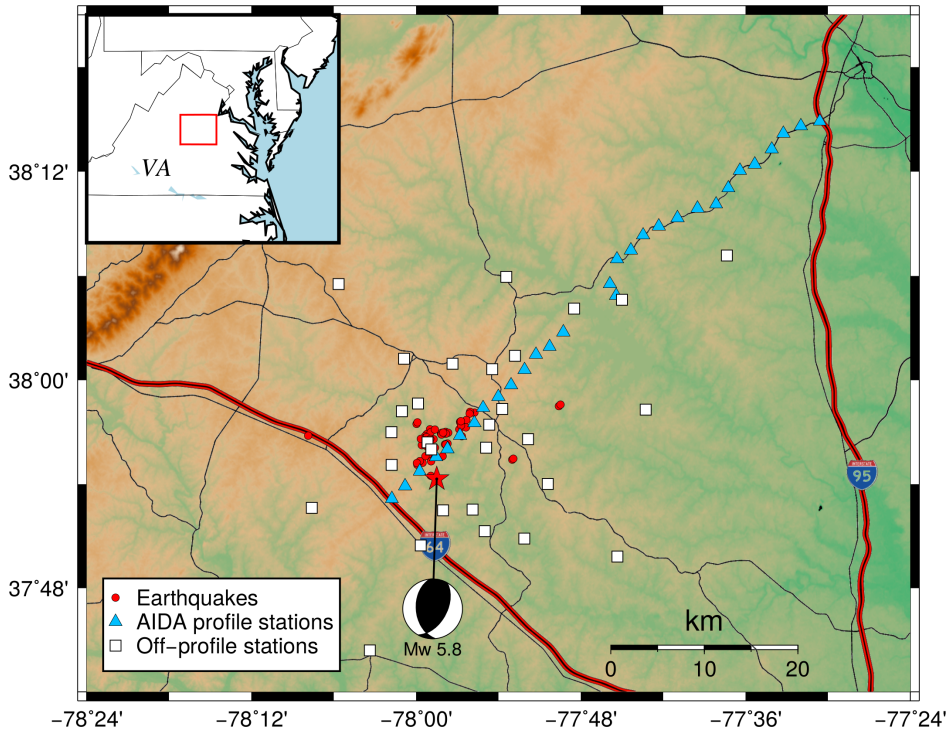

Figure 3.1: Map of study area showing the temporary station deployment for monitoring aftershock activity of the August 23, 2011 Mineral, Virginia earthquake. AIDA profile stations are shown as filled triangles and off-profile stations are shown by open squares. The earthquakes used in this study are denoted by filled circles. The inset map shows the location of the study area in central Virginia (rectangle). The mainshock focal mechanism is from Herrmann (2011; see Data and Resources Section). The epicenter of the mainshock is indicated by the filled star (Chapman, 2013). Note that the more distant AIDA profile stations to the northeast were deployed along a highway.

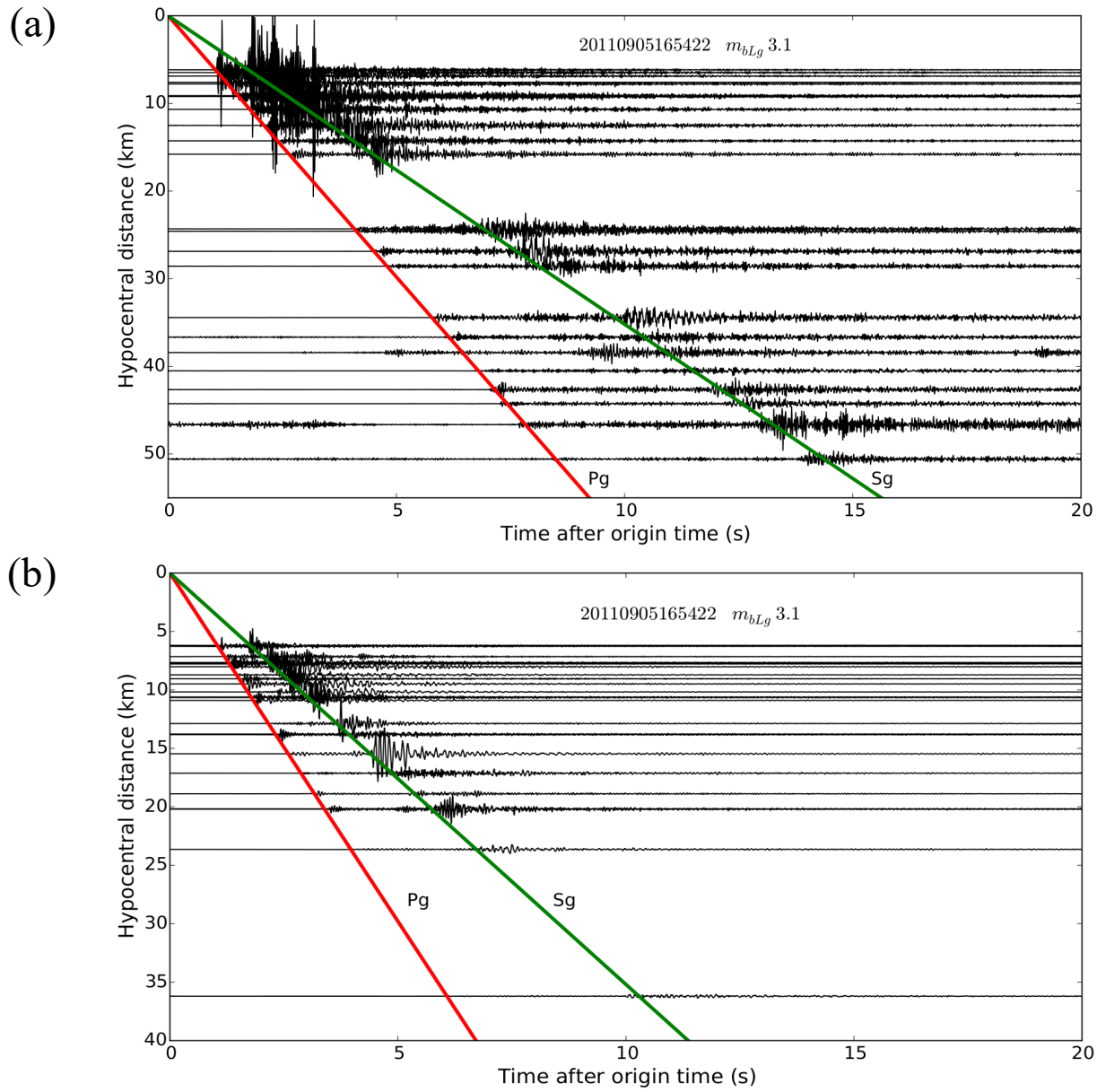

Figure 3.2: Vertical component recordings of the 16:54, 5 Sept., 2011 UTC $m_{b(Lg)}$ 3.1 aftershock recorded by (a) the AIDA profiles stations and (b) the off-profile stations. The traces are sorted by hypocentral distance and scaled by multiplying by the corresponding hypocentral distance to correct for geometrical spreading of R^{-1}.

The data used here were collected from 69 earthquakes ($m_{b(Lg)}$ 1.8 - 3.6) that occurred in the time period 25 August 24 December, 2011. Hypocenter locations and focal mechanisms

for those aftershocks were determined from the off-profile stations (Wu et al., 2015). The aftershocks are shallow, with depths ranging from 1.5 to 7.2 km, and most of them are located at depths 3-7 km. Figure 3.2 shows record sections for a September 5, 2011 event ($m_{b(Lg)}$ 3.1) recorded by the AIDA profile stations and the off-profile stations. The traces are sorted by hypocentral distance and scaled by multiplying by the corresponding hypocentral distance, which would correct for geometrical spreading of $R^{-1.0}$. An obvious observation is that the signal amplitudes at the distant stations are substantially under-corrected relative to the close-in stations, which indicates that the actual geometrical spreading should be steeper than $R^{-1.0}$.

3.3 Method and Analysis

We use the coda-normalization method to quantify the decay of the S-wave amplitudes. This method was originally proposed by Aki (1980) and normalizes the S-wave spectral amplitude by that of coda waves at a fixed lapse time. The method enables us to measure the distance decay of S-wave amplitudes from a data set obtained at a single station. It is based on the observation that coda spectral amplitude at a given lapse time greater than roughly twice the S-wave travel time is proportional to the source spectral amplitude of S waves and is independent of hypocentral distance. Frankel et al. (1990) extended this method to invert for Q and geometrical spreading from a set of earthquakes recorded by multiple stations. Many other studies applied this method to measure Q by assuming that geometrical spreading is proportional to R^{-1} (e.g., Yoshimoto et al., 1993; Kim et al., 2004). The method offers advantages for this study because the source spectrum, site response and

instrument response are effectively canceled by normalization of S-wave amplitudes using the coda wave amplitudes measured at a fixed lapse time.

The spectral amplitude of the recorded S-wave, $A_s(f, R)$, as a function of frequency f and hypocenter distance R, can be represented by

$$A_S(f, R) = CS(f)G(f)I(f)R^{-\gamma}e^{-\pi fR/Q(f)\beta} \tag{3.1}$$

where C is the S-wave radiation pattern factor, $S(f)$ is the source spectrum, $G(f)$ is the site amplification, $I(f)$ is the instrument response, γ is the coefficient of geometrical spreading, $Q(f)$ is the S-wave quality factor and β is the average S-wave velocity. The term $R^{-\gamma}$ represents the geometrical spreading effect, and the exponential term describes the anelastic attenuation effect.

The amplitude spectrum of the coda $A_C(f, t_C)$ at some lapse time t_C after the earthquake origin time can be represented as

$$A_C(f, t_C) = S(f)G(f)I(f)E(f, t_C) \tag{3.2}$$

where $E(f, t_C)$ is a function that describes the decay of coda as a function of frequency and lapse time. Dividing equation (3.1) by equation (3.2) leads to

$$\frac{A_S(f, r)}{CA_C(f, t_C)} = R^{-\gamma}e^{-\pi fR/Q(f)\beta}/E(f, t_C) \tag{3.3}$$

Normalizing the S-wave amplitude by dividing by the coda amplitude at a fixed lapse time removes the effects of the source spectrum, along with site and instrument response. Following Frankel et al. (1990), we assume that is the same for all earthquakes and stations and is not dependent on focal depth. We assume that the coda, being made up of scattered S-waves that have taken a wide range of paths between source and receiver, is largely independent of source radiation pattern at a sufficiently large lapse time. Following coda-normalization according to equation (3.3) for a fixed lapse time (e.g., twice the S-wave travel time or greater), amplitude versus distance data from multiple earthquakes can be combined on a single plot (for a given frequency), allowing attenuation parameters to be estimated jointly. Assuming that n stations record m earthquakes, a system of $(n \times m)$ linear observational equations can be written for a given frequency f:

$$\ln \frac{A_{Sij}(f, R_{ij})}{C_{ij} A_{Cij}(f, t_C)} = D - \gamma \ln R_{ij} - \pi f R_{ij}/Q\beta \tag{3.4}$$

where i^{th} earthquake is recorded by j^{th} station. D is a constant.

In Figure 3.3, we show the coda-normalized envelopes of the bandpass-filtered seismograms for station BUPP located 7.5 km from the hypocenter and station PTRD with a hypocentral distance of 35.1 km. The selected coda window corresponds to twice the S-wave travel time to 50 km hypocenter distance. The envelopes are plotted as functions of lapse time following the origin time of the earthquake. Figure 3.3 demonstrates that the coda decays are similar for stations at different hypocentral distances for lapse time greater than approximately 25 s. Note that the two stations have different instrument responses. And the effects of the

instrument responses are effectively removed by coda normalization, which highlights the fact that the coda-normalization method is particularly useful when the instrument responses are poorly known.

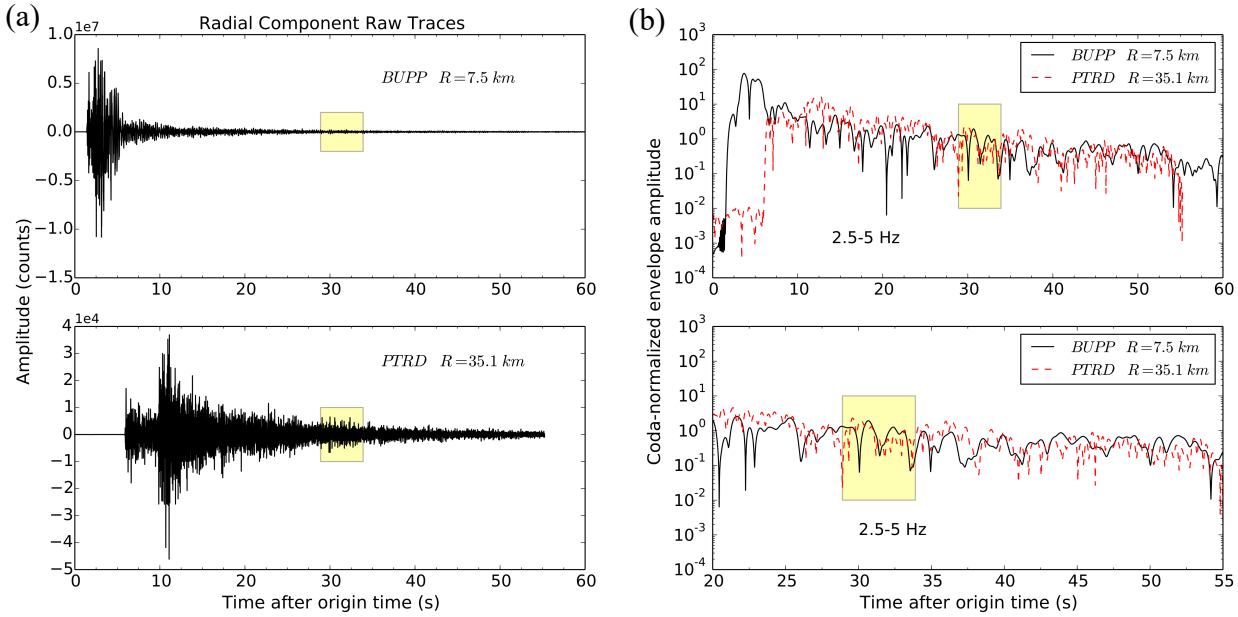

Figure 3.3: Radial component trace and coda-normalized envelopes for stations BUPP (7.5 km hypocentral distance) and PTRD (35.1 km hypocentral distance), from the $m_{b(Lg)}$ 3.6 earthquake at 09:09 UTC on 1 Sept., 2011. (a) The raw seismograms. Note that the two stations have different instrument types. (b) The envelope functions (right top) computed from traces filtered in octave-wide frequency bands 2.5-5 Hz. The coda lapse time window used to establish the amplitude normalization is from 28.9 to 33.9 seconds after the earthquake origin time (annotated by transparent rectangles). The lower part of 3b shows the late portion of the envelopes, illustrating the uniformity of coda decay between stations at different distances.

We rotated the seismic traces to radial, transverse and vertical components and analyzed them separately because the synthetic modeling by Chapman and Godbee (2012) suggests that the behavior of the vertical component is different from the horizontal components. We measured S-wave and coda amplitudes from the time-domain envelope function, derived from a series of narrow bandpass-filtered seismograms using a 7-pole Butterworth filter. This

measurement scheme has been found to be able to produce more stable results than calculating the Fourier spectrum in a short time window (Benz et al., 1997; Frankel, 2015). We use 10 octave-wide frequency bands, centered at frequencies 1.50, 2.10, 2.81, 3.75, 5.06, 6.75, 9.00, 12.60, 16.88 and 22.50 Hz. We measured the maximum amplitude of the envelope function in a 5-second time window following the predicted S-wave arrival time. The coda amplitude was calculated from the root-mean-square (RMS) amplitude of the envelope function in a 5-second time window beginning at lapse time t = 28.9s following the origin time, corresponding to twice the direct S-wave travel time to 50 km hypocentral distance, which is the maximum distance for this data set. The non-stationary nature of noise due to vehicular traffic required a visual inspection of the data from the more distant AIDA stations that were sited along a busy road (Figure 3.1). Recordings showing noise contamination from that source were not used. We further refined the selection of the remaining data based on a criterion that assumes a stationary noise amplitude. We used only data exhibiting coda amplitude at least three times greater than the amplitude of the pre-P-wave noise.

The radiation pattern factor C was calculated using equations (4.84) (4.86) in Aki and Richards (2002). The SV radiation pattern term was used to correct the observed S-wave amplitude on the radial and vertical components, whereas the SH radiation pattern was used for the transverse component.

The hypocentral distances involved in this study are less than 50 km. The recording sites are on weathered rock and residual soils, underlain at shallow depth by Paleozoic metamorphic rock with shear wave velocity in excess of 3.4 km/s (Chapman, 2013, Dreiling and Mooney, 2015, Davenport et al., 2015). Stephenson et al. (2015) investigated site conditions at

several of the stations used in this study. The interpreted bedrock depth at those stations varied from 3 m to 50 m, with median values ranging from 11 m to 34 m. We expect the anelastic attenuation to be negligible over most frequencies of interest because of the small distances and high Q of the basement rocks involved in this study. Assuming S-wave Q for the study area of approximately 740 at 10 Hz (McNamara et al., 2014b), the anelastic attenuation of amplitude at 50 km would be about 0.6 units from equation (3.4), while the geometrical spreading term at the same distance would be approximately 5 units. Assuming that frequency-dependent anelastic absorption is negligible, equation (3.4) can be written as

$$\ln \frac{A_{Sij}(f, R_{ij})}{C_{ij} A_{Cij}(f, t_C)} = D - \gamma \ln R_{ij} \tag{3.5}$$

where the constant D and the attenuation coefficient γ can be estimated by linear regression. The extent to which the assumption concerning high-frequency anelastic/scattering loss is viable can be assessed by examining any frequency-dependent behavior of the regression estimates of γ. If the effect of anelastic attenuation is significant, the estimates of γ from equation (3.5) should increase with frequency.

If significant frequency dependence is observed, corrections for anelastic attenuation should be made with an appropriate Q model. With an assumed Q model, equation (3.4) can be written as

$$\ln \frac{A_{Sij}(f, R_{ij})}{C_{ij} A_{Cij}(f, t_C)} + \pi f R_{ij} / Q\beta = D - \gamma \ln R_{ij} \tag{3.6}$$

Theoretically, geometrical spreading effects dominate the decay of S-wave amplitude in the near-source distance range of this study; therefore, the Q correction should not strongly affect the estimates of γ.

3.4 Results

In Figure 3.4, we plot the coda-normalized amplitudes of the S-wave against hypocentral distance for all earthquake-station pairs for the vertical, radial and transverse components in four of the ten frequency bands. The filled circles correspond to measurements, and the solid lines represent the least-squares fits to the data. As a reference, we plot the amplitude decay of R^{-1} for a homogeneous whole space with dashed lines. The best estimates of the geometrical spreading coefficient γ are also shown in Figure 3.4. The data points are in good agreement with the fitted lines with little scatter, which indicates the reliability and efficiency of the coda-normalization method. It is obvious that the observed amplitude decay is substantially steeper than R^{-1} for all three components throughout the listed frequency bands. There appears to be no systematic differences between the three components of motion for the frequency bands shown in Figure 3.4. For the radial component at high frequencies such as 8.4 16.8 Hz and 15 30 Hz (Figure 3.4), it appears that the amplitude decay may have a shallower slope at larger distances (20 50 km) than at closer distances. If real, this perhaps indicates a depth dependence of Q or a change of geometrical spreading with distance. The estimates of γ for the whole data set over the full distance range of the data are dominated by the abundant data at distances less than 20 km. Attempts to fit the data with a bi-linear regression model allowing a change in slope at 20 km were undertaken.

The slope of the bi-linear model at distances less than 20 km agrees closely with that of the linear fit to the whole data set at all frequencies. The bi-linear fit at larger distances is very uncertain due to lack of data, and the slope at larger distances is not significantly different from that at closer distances, given the uncertainties. Unfortunately, we lack the data necessary to establish whether or not a change in slope occurs in this data set at a distance of 20 km.

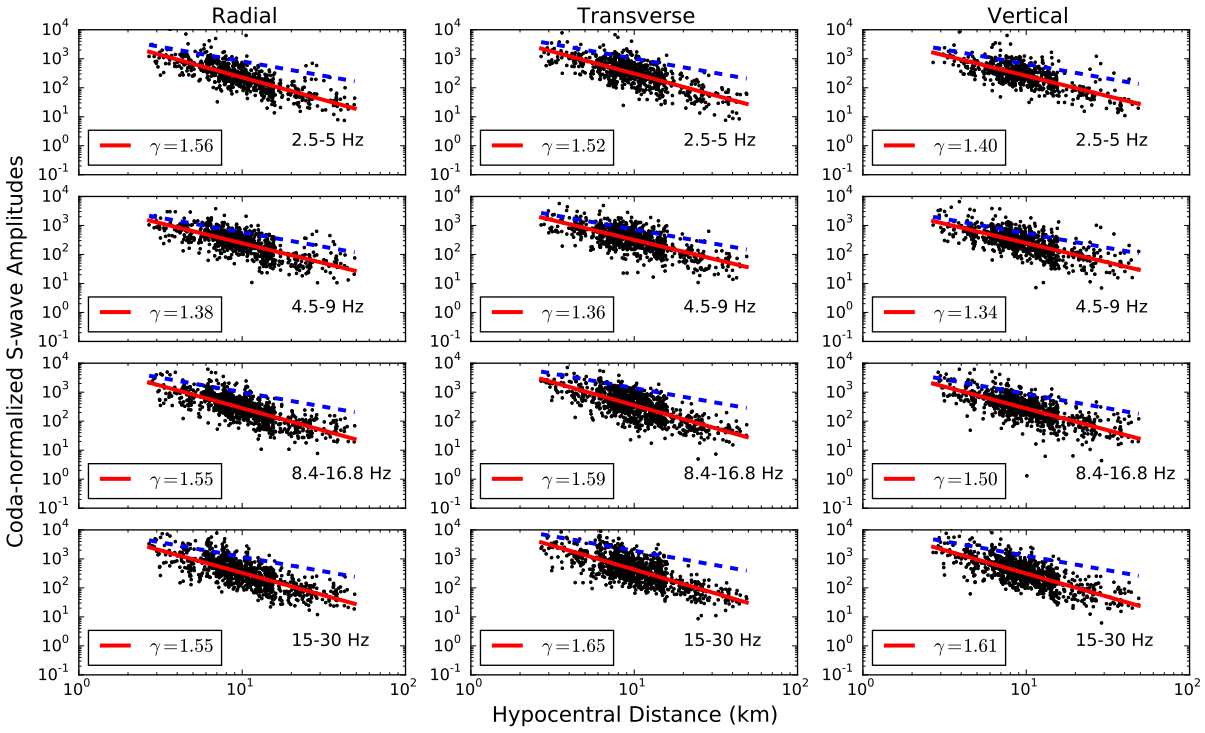

Figure 3.4: Plots of coda-normalized S-wave peak trace envelope amplitudes (small dots) versus hypocentral distance in 4 octave-wide frequency bands, centered at 3.75, 6.75, 12.6 and 22.5 Hz. Left column shows radial component amplitudes, center column shows transverse component amplitudes, and the right column shows vertical component amplitudes. The solid lines show least-squares fits to the data. The corresponding geometrical spreading coefficients γ are shown at the lower-left corner of each subplot. The dashed lines indicate the slope of geometrical spreading of R^{-1} ($\gamma = 1$) in a homogeneous whole space.

Radiation pattern has been observed to have less effect at high frequencies than at low

frequencies because of increased scattering and source complexity as frequencies increase (e.g., Zeng at al., 1995). We performed our analysis with and without the radiation pattern correction. The estimates of γ for the three components for all ten frequency bands with and without radiation pattern correction are shown in Figure 3.5. The error bars represent ± one standard error of estimate. It appears that the radiation pattern correction does not make a significant difference in either the mean estimate of γ or the standard error of γ. We expected the radiation pattern correction to reduce the scatter in the data. The fact that this did not occur to a significant degree may point to significant scattering at all frequencies used in our study. Additionally, many earthquakes with various focal mechanism solutions were combined to achieve a joint estimate of γIt is conceivable that radiation pattern effects on attenuation are masked (smoothed) by effectively averaging over many different focal mechanism solutions. The estimated values of γ, with small standard errors for all the frequency bands except for the lowest frequency band 1-2 Hz, do not show compelling evidence of systematic trends with frequency. Since the earthquakes used in this study are shallow (1.5 - 7.2 km), we notice that at low frequencies (< 3 Hz) surface waves sometimes dominate the energy in the 5 s window in which we search for the peak amplitude of the *S*-wave. It is likely that the unstable estimations at low frequencies, as indicated by the larger standard errors of estimate, are due to the presence of appreciable surface wave energy in the analysis window. The results for the three components are very similar, with weighted-mean estimates over the 10 frequency bands of 1.51±0.05, 1.51±0.05 and 1.45±0.05 for radial, transverse and vertical component, respectively. These results differ from those reported by Dreiling and Mooney (2015). They used Mineral earthquake aftershock data recorded by the AIDA profile stations and examined peak time domain S-wave amplitudes in four

octave-wide frequency bands. For the geometric mean of the two horizontal components, they reported attenuation coefficients of 0.8 (1-2 Hz), 0.9 (2-4 Hz), 1.05 (4-8 Hz) and 1.15 for 8-16 Hz. They used a regression of peak S-wave envelope amplitude with hypocentral distance, but did not normalize the peak S-wave amplitudes using coda amplitudes as was done in this study. Also, this study used 32 off-profile stations in addition to the 30 AIDA profile stations, corrected for radiation pattern, and used a larger set of earthquakes. The coda normalization we have used significantly reduces the scatter in the S-wave amplitude versus distance regressions. This, along with the larger data set used in this study, may account for the differences in geometrical spreading determined here and those determined by Dreiling and Mooney (2015).

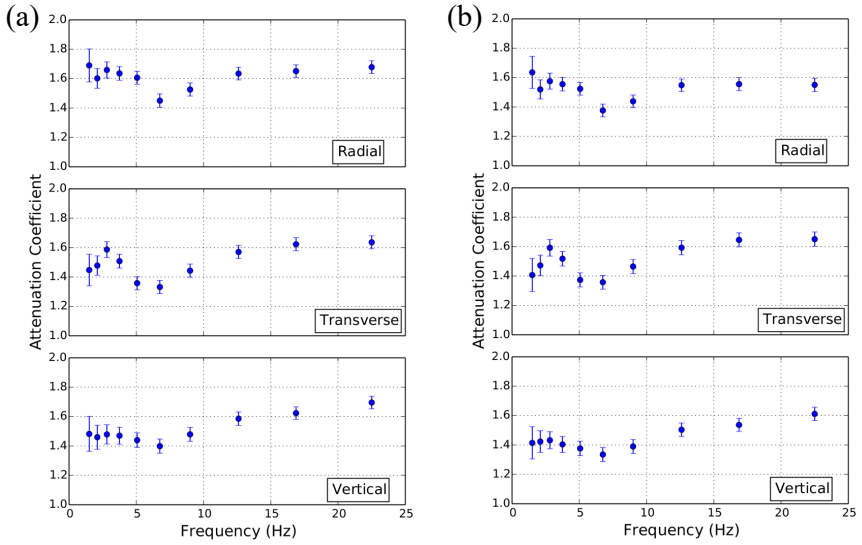

Figure 3.5: Estimates of γ, the attenuation coefficient, for peak S-wave ground motion in 10 octave-wide frequency bands centered at 1.50, 2.10, 2.81, 3.75, 5.06, 6.75, 9.00, 12.60 16.88, and 22.50 Hz, (a) without radiation pattern correction; and (b) with radiation pattern correction. Error bars indicate ± one standard error of estimate. The results for radial, transverse and vertical component are shown from top to bottom.

Figure 3.5 shows a systematic increase of γ with frequency at frequencies greater than 7

Hz. This implies possible frequency-dependent effects caused by anelastic absorption and scattering. There have been several Q models developed in this area. Chapman and Rogers (1989) assumed a geometrical spreading of R^{-1} and determined a frequency-dependent coda Q, represented by $Q = 811f^{0.42}$ (1.5 Hz < f < 12 Hz), in the Southern Appalachian region (referred to here as Q model 1). A recent study by McNamara et al. (2014b) found from regional L_g waves (here, Q model 2) and from local S waves (here, Q model 3) for the CVSZ and surrounding EUS region. For the geometrical spreading correction, McNamara et al. (2014b) applied $R^{-0.5}$ for L_g waves, and a hinged-trilinear functional form for S waves. This hinged-trilinear functional form was proposed by Atkinson (2004) to describe the geometrical spreading in ENA as $R^{-1.3}$ to 70 km, as $R^{0.2}$ for 70 130 km, and as $R^{-0.5}$ beyond 130 km. Mereu et al. (2013) demonstrated that there is no unique pair of values of the coefficients Q_0 and η to describe the frequency-dependent quality factor relationship. The trade-off between Q_0 and η allows different Q models to represent the anelastic attenuation equally well. We applied each of the three Q models and made the correction based on equation (3.6). The results are summarized in Figure 3.6. It is apparent that the estimation is not very sensitive to the assumed Q model, which supports our assumption that the geometrical spreading dominates the decay of S-wave amplitude in the distance range of interest here. The Q corrections reduced the frequency variation of the estimated values to some extent, particularly at high frequencies. The results for the three components are consistent, neglecting the unstable estimates at very low frequencies. Q model 3 performs slightly better at high frequencies, making the estimated geometrical spreading coefficients lie in an approximate range of 1.2-1.4, with a weighted-mean value of 1.37±0.05, 1.37±0.05 and 1.30±0.05 for radial, transverse and vertical component, respectively. Table 3.1 lists the

values of γ (weighted mean over all frequency bands) and their standard errors of estimate, for radial, transverse and vertical components, for each assumed Q model. The differences of apparent geometrical spreading coefficients determined by applying different Q models are less than 0.1, indicating the stability of our results.

Table 3.1: Weighted-mean values of γ with assumed Q models.

Q model	Radial Component	Transverse Component	Vertical Component
1	1.46±0.05	1.46±0.05	1.40±0.05
2	1.44±0.05	1.44±0.05	1.37±0.05
3	1.37±0.05	1.37±0.05	1.30±0.05

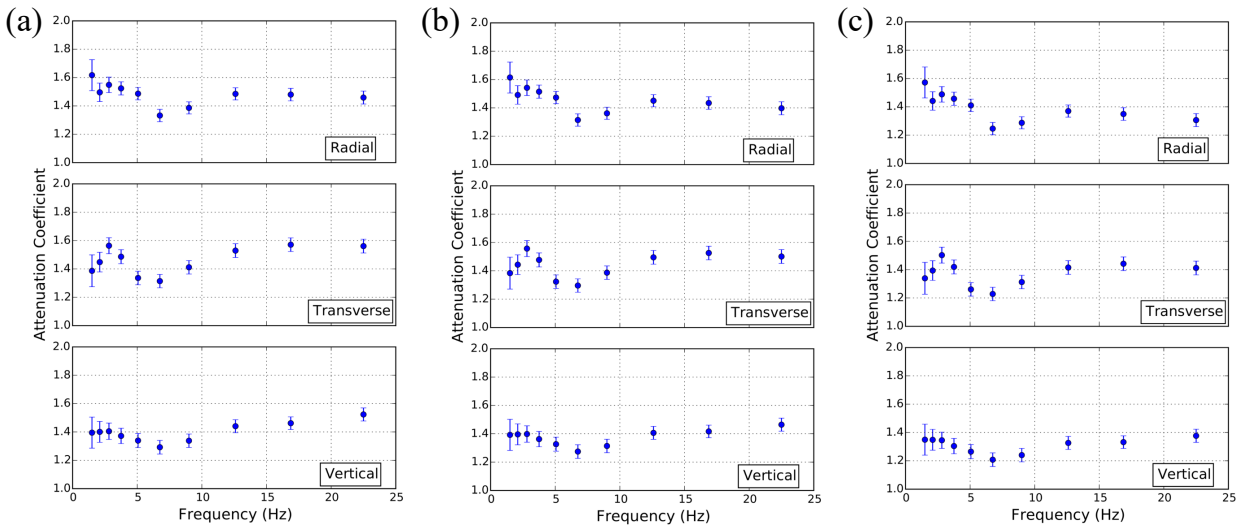

Figure 3.6: Estimates of the apparent geometrical spreading coefficient γ for peak S-wave ground motion in 10 octave-wide frequency bands with assumed Q models. (a) Q model 1 from Chapman and Rogers (1989); (b) Q model 2 from McNamara et al. (2014b); (c) Q model 3 from McNamara et al. (2014b). The error bars represent ± one standard error of estimate.

3.5 Discussion

3.5.1 Measurement of amplitudes

A broadening of high-frequency S-wave seismogram envelopes of local earthquakes with increasing hypocentral distance was reported in previous studies (Sato, 1989; Atkinson, 1993; Tripathi et al., 2010). In that circumstance, the peak amplitude may not necessarily represent the direct S-wave amplitude. We observed that the peak amplitude sometimes appears several seconds after the first arrival of the S wave at low frequencies. Both the broadening of the envelope and surface wave contamination may contribute to the uncertainty of amplitude measurement, and may affect the estimate of γ. We compared two different measures of S-wave amplitude: the peak amplitude measurement in the 5 s window beginning at the predicted S-wave arrival time as described above in the Method and Analysis section, and the RMS amplitude of a 2 s window centered on the peak amplitude. In Figure 3.7a, we compare the estimates of γ using the peak amplitude measurement to those using the RMS amplitudes, without accounting for Q effects. The results obtained from the RMS amplitude analysis appear to show smaller variation with frequency, implying that the RMS amplitudes may better represent the S-wave amplitude. However, the use of a fixed window-length for all frequency bands could eliminate possible frequency-dependent characteristics if any exists. This explains the observation that the results obtained from the RMS amplitude analysis with a fixed window-length are very similar to those obtained from the peak amplitude analysis with additional Q corrections, as illustrated in Figure 3.7b. To avoid the possible artifacts due to fixed-window measurements, we applied an adaptive window scheme, in which the window was also placed around the peak amplitude, the window length was chosen

to be proportional to the central period of the associated frequency band, and the S-wave amplitude was taken from the RMS value of the window. The estimates of γ made using the adaptive window were nearly identical to those determined by the peak-amplitude analysis (Figure 3.7c).

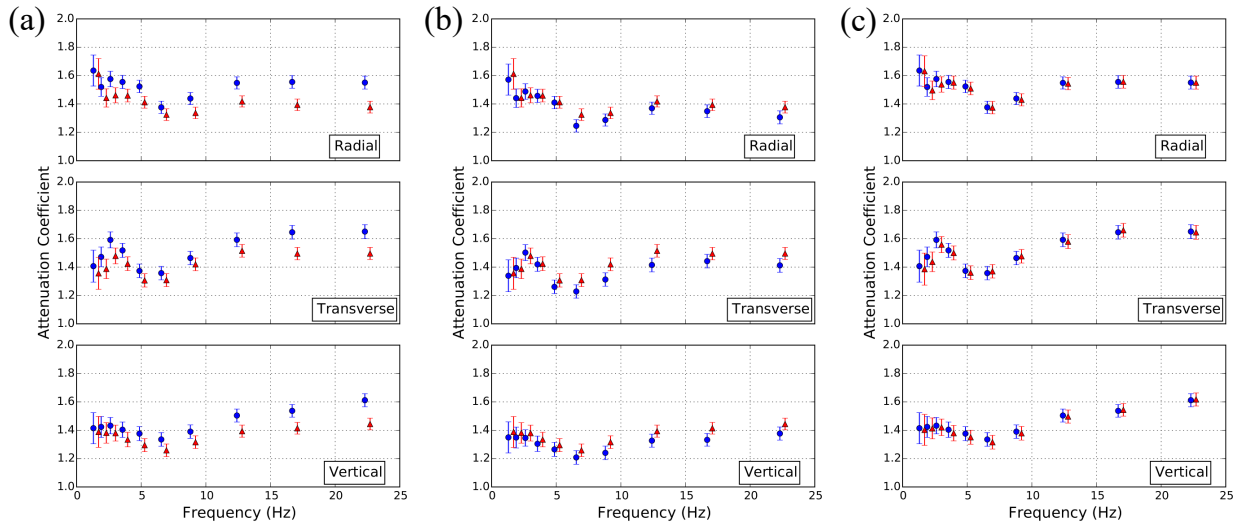

Figure 3.7: Comparisons of the estimates of attenuation coefficients using different measurements of S-wave amplitudes in 10 octave-wide frequency bands. (a) Comparison of the estimates of γ using peak-amplitude measurements (dots) and RMS amplitude measurements in a 2 s window (triangles); (b) Comparison of the estimates using peak-amplitude measurements with additional Q correction using Q model 3 from McNamara et al. (2014b) (dots) and RMS amplitude measurements in a 2 s window (triangles); (c) Comparison of the estimates of γ using peak-amplitude measurements (dots) and RMS amplitude measurements in an adaptive window with the window length twice the central period of the examined frequency band (triangles). The error bars represent ± one standard error of estimate. For display purposes, the dots and triangles are shifted 0.2 units to the left and right from their true positions, respectively, in the horizontal direction.

3.5.2 Effects of window length

A window length of 5 s was used for the measurements of peak S-wave amplitude and coda-wave amplitude in this study. Our results suggest that variation of window length causes

no significant change in the coda-amplitude measurement, because coda-wave amplitude is approximately stationary at lapse time greater than approximately twice the S-wave travel time. For the S-wave amplitude measurement, on the other hand, the variation of window length may affect the estimated S-wave decay significantly in cases where the peak amplitude does not appear to be the first arrival. We found that a window length of 5 s was always long enough to capture the peak amplitude for our dataset. We obtained almost identical results for the RMS amplitude measurements of the S-wave in a fixed window, using window lengths of 2, 3, 4 and 5 s. No noticeable differences in the estimates were found by using an adaptive window length of $1T$, $2T$, $3T$, $4T$ or $5T$, where T represents the central period of the corresponding frequency band. The experiments point to the fact that the RMS measurement can produce stable results given a reasonable range of window lengths.

3.5.3 Effects of Q

In principle, the geometrical spreading exponent γ and Q could be jointly inferred from the non-linear inversion of coda-normalized amplitudes with equation (3.4), but the trade-off between γ and Q could give rise to unreasonable values of these parameters. Frankel et al. (1990) found that the S-wave amplitude decays can be fit with either a frequency-independent Q and a geometrical spreading exponent γ greater than 1 or a frequency-dependent Q and a geometrical spreading of R^{-1} in New York State and South Africa. De lorenzo et al. (2013) proposed a quadratic approximation of the coda-normalization method to jointly obtain stable estimates of γ and Q. However, the hypocentral distances involved in our dataset are less than 60 km and our study area is characterized by high Q values,

therefore, the effect of Q should be negligible compared to that of geometrical spreading. As demonstrated in a previous section, we observed a systematic increase of γ with frequency, for frequencies greater than 7 Hz (Fig. 3.5). In principle this could be due to anelastic attenuation/scattering. We examined that possibility using three very different Q models from previous studies (Chapman and Rogers, 1989; McNamara et al., 2014b), and found that the Q-corrected apparent geometrical spreading coefficients lie in the range of 1.3-1.5 and were thus not very sensitive to the assumed Q model.

3.5.4 Regional variation

Previous studies in southeastern Canada and in the northeastern United States (Atkinson and Mereu, 1992; Atkinson, 2004; Atkinson et al., 2011; and Atkinson and Boore, 2014) determined the amplitude decay rate to be between $R^{-1.1}$ and $R^{-1.3}$ for distances out to 70 km depending on the dataset used. Zandieh and Pezeshk (2010) reported a geometrical spreading of R^{-1} at distances less than 70 km in the New Madrid seismic zone. Frankel (2015) used the coda-normalization method to examine near-source S-wave attenuation at distances 1080 km in the Charlevoix, Quebec, region from 7 earthquakes with M_N magnitudes in the range 3.3-5.4, and focal depths from 6.5 to 24.5 km. Six of those events were at depths between 11 and 25 km, substantially deeper than those studied here. We examined the amplitude decay in the distance range 10 50 km which is common to this study and Frankel (2015). We found the results obtained using only data at distances 10 50 km very similar to those using the data over the full distance range. At frequencies near 1 Hz, 5 Hz and 14 Hz, we found geometrical spreading exponents (averaged over three components)

of -1.58±0.20, -1.41±0.10 and -1.53±0.09 respectively, while Frankel (2015) reported values of -1.52±0.17, -1.21±0.14 and -0.79±0.15 respectively. The resolved geometrical spreading exponents at low frequencies (near 1 Hz) are similar in both studies. However, the significant frequency dependence observed in Frankel (2015), which he attributed to radiation pattern and directivity effects, was not found in this study.

It is possible that the divergent results of different studies dealing with geometrical spreading are due to factors such as random variability in the limited data sets, subtle differences in analysis methods and un-modeled physical effects, such as source directivity. However, the results here suggest that there may be real differences in geometrical spreading between different regions of ENA. Such differences might conceivably arise due to systematically different crustal structure and earthquake focal depth. This implies that the results obtained from a certain region may not be applicable everywhere. Differences in attenuation might also exist between earthquakes at different depths in the same region. The depth range of the earthquakes used in this study is 1.5-7.5 km and more than half of those earthquakes occurred in the narrow range 4-6 km. Resolving any depth dependent behavior of γ over this limited range of focal depth is problematic. We examined the distance decay in different focal depth ranges (0-4 km, 4-6km, 6-8km) and found no evidence of systematic depth dependence of γ. The earthquakes studied here occurred in detached metamorphic rocks of Paleozoic age above the basal Appalachian Decollement which lies at a depth of approximately 12 km (Chapman 2013; Wu et al. 2015).The underlying Grenville basement may be more representative of conditions at Charlevoix and may be more isotropic in regard to wave propagation and attenuation than the detached Paleozoic Appalachian crystalline rocks containing the direct S-wave raypaths of our data set. A direct comparison with the results of Frankel et al.

(2015) would require data from shocks at depth in the basement and such deep shocks are not known to occur in the central Virginia seismic zone (Chapman, 2013). Another notable point is that our data at the largest distances are mostly sampling azimuths sub-parallel to the strike direction of Appalachian structure. Data at small distances sample a wide range of azimuths. Appreciable azimuthally dependent attenuation due to the Appalachian structural grain might be reflected by larger γ (more attenuation) at smaller distances. Insofar as the sparse data at distances greater than 20 km suggest that such may be the case, the Appalachian structural grain in the study area may be a contributing factor.

3.6 Conclusions

We analyzed data from 69 aftershocks of the 2011 Mineral, Virginia earthquake by means of the coda-normalization method to quantify S-wave amplitude decay with distance at hypocentral distances less than 60 km in the CVSZ. The coda-normalized S-wave amplitudes were corrected for the source radiation pattern. The observed S-wave amplitudes decay as a function of hypocenter distance R according to $R^{-1.51}$, $R^{-1.51}$, and $R^{-1.45}$ for radial, transverse and vertical component motion, respectively. Frequency-dependent attenuation effects are found to be marginally significant in the data examined. With assumed Q models, the apparent geometrical spreading coefficients γ are determined to be in the range of 1.37-1.46, 1.37-1.46 and 1.30-1.40 for radial, transverse and vertical component, respectively, which are substantially steeper than R^{-1} for a homogeneous whole space.

The results of this study can be used in the stochastic simulation method to predict ground motions in the CVSZ. The earthquakes studied here are shallow, with focal depths less than 8

km, and the results obtained may not be applicable in other parts of ENA where earthquakes typically occur at greater depths.

References

Aki, K. (1980). Attenuation of shear waves in the lithosphere for frequencies from 0.05 to 25 Hz, *Phys. Earth Planet. Int.* **21**, 50-60.

Aki, K., and P. G. Richards (2002). *Quantitative Seismology*, Second Ed., Univ. Sci. Books, Sausalito, California.

Atkinson, G. M. (1993). Notes on ground motion parameters for eastern North America: duration and H/V ratio, *Bull. Seismol. Soc. Am.* **83**, 587-596.

Atkinson, G. M. (2004). Empirical attenuation of ground-motion spectral amplitudes in southeastern Canada and the northeastern United States, *Bull. Seismol. Soc. Am.* **94**, 1079-1095.

Atkinson, G. M. and D. M. Boore (1995). New ground motion relations for eastern North America, *Bull. Seismol. Soc. Am.* **85**, 17-30.

Atkinson, G. M. and D. M. Boore (2006). Earthquake ground motion prediction equations for eastern North America, *Bull. Seismol. Soc. Am.* **96**, 2181-2205.

Atkinson, G. M., and D. M. Boore (2014). The attenuation of Fourier amplitudes for rock sites in eastern North America, *Bull. Seismol. Soc. Am.* **104**, 513-528.

Atkinson, G. and R. Mereu (1992). The shape of ground motion attenuation curves in southeastern Canada, *Bull. Seismol. Soc. Am.* **82**, 2014-2031.

Atkinson, G., N. Kraeva and K. Assatourians (2011). Ground-motion attenuation at short hypocentral distances (¡ 30 km) near Sudbury, Ontario, *Bull. Seismol. Soc. Am.* **101**, 433-437.

Benz, H. M., A. Frankel, and D. M. Boore (1997). Regional Lg attenuation for the continental United States, *Bull. Seismol. Soc. Am.* **87**, 606-619.

Bollinger, G. A. (1969). Seismicity of the central Appalachian states of Virginia, West Virginia, and Maryland 1758 through 1968, *Bull. Seismol. Soc. Am.* **59**, 2103-2111.

Bollinger, G. A. (1973a). Seismicity and crustal uplift in the southeastern United States, *Am. J. Sci.* **273-A**, 396-408.

Bollinger, G. A. (1973b). Seismicity of the southeastern United States, *Bull. Seismol. Soc. Am.* **63**, 1785-1808.

Boore, D. M. (1983). Stochastic simulation of high-frequency ground motions based on seismological models of the radiated spectra, *Bull. Seismol. Soc. Am.* **73**, 1865-1894.

Boore, D. M. (2003). Prediction of ground motion using the stochastic method, *Pure Appl.Geophys.* **160**, 635-676.

Burger, R., P. Somerville, J. Barker, R. Herrmann, and D. Helmberger (1987). The effect of crustal structure on strong ground motion attenuation relations in eastern North America,

Bull. Seismol. Soc. Am. **77**, 420-439.

Chapman, M. C. (2013). On the rupture process of the 23 August 2011 Virginia earthquake, *Bull. Seismol. Soc. Am.* **103**, 613-628.

Chapman, M.C. and R.W. Godbee (2012). Modeling geometrical spreading and the relative amplitudes of vertical and horizontal high-frequency ground motions in eastern North America, *Bull. Seismol. Soc. Am.* **102**, 1957-1975.

Chapman, M. C., and M. J. B. Rogers (1989). Coda Q in the southern Appalachians, *Geophys. Res. Lett.* **16**, no. 6, 531-534.

Davenport, K. K., J. A. Hole, D. A. Quiros, L. D. Brown, M. C. Chapman, L. Han, and W. D. Mooney (2015). Aftershock imaging using a dense seismometer array (AIDA) after the 2011 Mineral, Virginia earthquake, in *The 2011 Mineral, Virginia, Earthquake and its Significance for Seismic Hazards in Eastern North America*, Horton, J.W., Jr., Chapman, M.C., and Green, R.A., (Editors), Geological Society of America Special Paper 509, doi:10.1130/2015.2509(15), 273-283.

de Lorenzo S., F. Bianco, and E. D. Pezzo (2013). Frequency dependent Q and Q in the Umbria-Marche (Italy) region using a quadratic approximation of the coda-normalization method, *Geophys. J. Int.* **193**, 1726-1731.

Dreiling, J. and W. D. Mooney (2015). Shear-wave velocity structure and attenuation derived from aftershock data of the 2011 Mineral, Virginia, earthquake, in *The 2011 Mineral, Virginia, Earthquake and its Significance for Seismic Hazards in Eastern North America*,

Horton, J.W., Jr., Chapman, M.C., and Green, R.A., (Editors), Geological Society of America Special Paper 509, doi:10.1130/2015.2509(05), 81-94.

Frankel, A. (2015). Decay of S-wave amplitudes with distance from earthquakes in the Charlevoix, Quebec area: Effects of radiation pattern and directivity, *Bull Seismol. Soc. Am.* **105**, 850-857.

Frankel, A., A. McGarr, J. Bicknell, J. Mori, L. Seeber and E. Cranswick (1990). Attenuation of high-frequency shear waves in the crust: Measurements from New York state, South Africa, and southern California, *J. Geophys. Res.* **95**, 17,441-17,457.

Hanks, T., and R. T. McGuire (1981). The character of high-frequency strong ground motion, *Bull. Seismol. Soc. Am.* **71**, 2071-2095.

Kim, W., and M. Chapman (2005). The 9 December 2003 central Virginia earthquake sequence: A compound earthquake in the Central Virginia Seismic Zone, *Bull. Seismol. Soc. Am.* **95**, 2428-2445.

Kim, K. D., T. W. Chung, and J. B. Kyung (2004). Attenuation of High-Frequency P and S Waves in the Crust of Choongchung Provinces, Central South Korea, *Bull. Seismol. Soc. Am.* **94**, 1070-1078.

McNamara, D. E., H. M. Benz, R. B. Herrmann, E. A. Bergman, P. Earle, A. Meltzer, M. Withers, and M. Chapman (2014a). The Mw 5.8 Mineral, Virginia, earthquake of August 2011 and aftershock sequence: constraints on earthquake source parameters and fault geometry, *Bull. Seismol. Soc. Am.* **104**, 40-54.

McNamara, D. E., L. Gee, H. M. Benz, and M. Chapman (2014b). Frequency-dependent seismic attenuation in the eastern United States as observed from the 2011 central Virginia earthquake, *Bull. Seismol. Soc. Am.* **104**, 55-72.

Mereu, R. F., S. Dineva, and G. M. Atkinson (2013). The application of velocity spectral stacking to extract information on source and path effects for small-to-moderate earthquakes in southern Ontario with evidence for constant-width faulting, *Seismol. Res. Lett.* **84**, 899-916.

Sato, H., (1989). Broadening of seismogram envelopes in the randomly inhomogeneous lithosphere based on the parabolic approximation: southeastern Honshu, Japan, *J. Geophys. Res.* **94**, 17,735-17,747.

Stephenson, W. J., J. K. Odum, D. E. McNamara, R. A. Williams, and S. J. Angster (2015). Ground-motion site effects from multimethod shear-wave velocity characterization at 16 seismograph stations deployed for aftershocks of the August 2011 Mineral, Virginia, earthquake, in *The 2011 Mineral, Virginia, Earthquake and its Significance for Seismic Hazards in Eastern North America*, Horton, J.W., Jr., Chapman, M.C., and Green, R.A., (Editors), Geological Society of America Special Paper 509, doi:10.1130/2015.2509(03), 47-65.

Taber, S. (1913). Earthquakes in Buckingham county, Virginia, *Bull. Seismol. Soc. Am.* **3**, 124-133.

Toro, G. N., N. Abrahamson and J. Schneider (1997). Model of strong ground motion in eastern and central North America; best estimates and uncertainties, *Seismol. Res. Lett.*

68, 41-57.

Tripathi J. N., H. Sato and M. Yamamoto (2010). Envelope broadening characteristics of crustal earthquakes in northeastern Honshu, Japan, *Geophys. J. Int.* **182**, 988-1000.

Wessel, P., and W. Smith (1991). Free software helps display data, *Eos Trans. AGU* **72**, 445-446.

Wu, Q., M. C. Chapman, and J. N. Beale (2015). The aftershock sequence of the 2011 Mineral, Virginia, earthquake: temporal and spatial distribution, focal mechanisms, regional stress, and the role of Coulomb stress transfer, *Bull. Seismol. Soc. Am.* **105**, 2521-2537.

Yoshimoto, K., H. Sato, and M. Ohtake (1993). Frequency-dependent attenuation of P and S waves in the Kanto area, Japan, based on the coda-normalization method, *Geophys. J. Int.* **114**, 165-174.

Zandieh, A., and S. Pezeshk (2010). Investigation of geometrical spreading and quality factor functions in the New Madrid seismic zone, *Bull. Seismol. Soc. Am.* **100**, 2185-2195.

Zeng, Y., J. G. Anderson, and F. Su (1995). Subevent rake and random scattering effects in realistic strong ground motion simulation, *Geophys. Res. Lett.* **22**, 17-20.

Chapter 4

Stress Drop Estimates and Source Scaling of the 2011 Mineral, Virginia Mainshock and Aftershocks †

†**Note: Wu, Q.** and M. C. Chapman (2017). Stress Drop Estimates and Source Scaling of the 2011 Mineral, Virginia Mainshock and Aftershocks, *Bull. Seismol. Soc. Am.* (**In revision**).

Abstract

We estimate corner frequencies and stress drops for the 2011 Mw 5.65 Mineral, Virginia earthquake and its aftershocks using a multi-window coda spectral ratio method. To obtain reliable measurements of corner frequency as well as the associated uncertainties, we apply a Bayesian approach using a Markov chain Monte Carlo algorithm to fit the observed spectral ratios of selected event pairs with the omega-square source spectral model (i.e., Brune model). Detailed analysis procedures are presented. We show that the use of S-wave coda provides more stable source spectral ratios than using direct S-waves. The event pairs are selected by examining the common decay characteristics of narrow-band coda envelopes. We determined an unusually high stress drop of 86 MPa for the mainshock. The estimated stress drops for the aftershocks with moment magnitudes ranging from 0.71 to 4.16 have a wide range of 0.02-80 MPa. The larger earthquakes (M_W 3 and greater) have high stress drops within a relatively small range of 10-100 MPa. We observe a decrease of stress drop with decreasing magnitude below ~ M_W 2.5, suggesting a possible breakdown of self-similar source scaling. However, that observation could in principle be related to the limited bandwidth of the data. We found no clear depth dependence or temporal patterns in the estimated stress drops. A spatially isolated cluster of shallow aftershocks was determined to have systematically low stress drops, possibly indicating triggering of seismicity on a set of relatively weak fault or joint planes.

4.1 Introduction

The 23 August 2011 moment magnitude $M + W$ 5.65 Mineral, Virginia earthquake caused severe damage (VIII MMI) in Louisa County, Virginia near the epicenter and significant damage as far away as Washington D.C. (Chapman, 2013; Wells et al., 2015). Even though the mainshock was poorly recorded at local to regional distances, the aftershock sequence was well recorded by a temporary network consisting of 32 stations, making it one of the best studied aftershock sequences in eastern North America (ENA) (Chapman, 2013; McNamara et al., 2014; Wu et al., 2015). This earthquake sequence, which spans about five orders of magnitude, provides an opportunity to study the source characteristics and scaling relationships of intraplate earthquakes in ENA, where the seismicity rate is generally low and moderate-to-large earthquakes are infrequent.

Stress drop and seismic moment are two important earthquake source parameters (e.g., Brune 1970, 1971). For a given seismic moment (or magnitude Mw), high-frequency ground motion amplitudes depend on stress drop (Boore, 1983; Hanks and Johnston, 1992; Hough, 2014). The relationship between seismic moment and stress drop (source scaling) plays an important role not only in understanding source physics, but also in strong ground-motion prediction. However, it has been a controversial issue since Aki (1967) first proposed the scaling law of the source spectrum. Self-similar source scaling at magnitudes greater than ~ 4 is supported by numerous studies (e.g., Ide et al., 2001; Imanishi et al., 2004; Oth et al., 2010; Baltay et al., 2011). On the other hand, some studies have shown evidence of a breakdown in constant-stress drop scaling at smaller magnitudes (e.g., Dysart et al., 1988; Shi et al., 1998; Izutani and Kanamori, 2001; Mayeda et al., 2007; Malagnini et al., 2008;

Yoo et al., 2010; Somei et al., 2014). Another important issue is the dependence of stress drop on tectonic setting. It has been reported that the stress drops of intraplate earthquakes are larger than those of interplate earthquakes (Kanamori and Anderson, 1975; Scholz et al., 1986; Allmann and Shearer, 2009; Boyd et al., 2017). Allmann and Shearer (2009) investigated the global variation of stress drops for earthquakes with moment magnitudes 5.2 to 8.3 and found that stress drops for intraplate earthquakes are two times higher compared to interplate earthquakes. A recent study of 1121 M_W 3 and larger earthquakes in the lower 48 United States and parts of Canada (Boyd et al., 2017) found that the Brune stress drops for tectonic mainshocks in the eastern United States (EUS) ranges from 2.6 to 36 MPa whereas stress drops for mainshocks in the western United States (WUS) range from 1.0 to 7.9 MPa. Another question involves the stress drops of shallow earthquakes induced by fluid injection. Boyd et al. (2017) found that stress drops of potentially induced mainshocks in the central United States (CUS) range from 0.6 to 5.6 MPa, or approximately 5 times less than stress drops of tectonic earthquakes in the EUS. Huang et al. (2016) obtained a range of stress drops of 1.02-42.5 MPa with a median of 10.57 MPa for the Guy-Greenbrier, Arkansas sequence, which was potentially induced by waste-water injection. A stress drop of approximately 10 MPa is typical of values reported for tectonic earthquakes in ENA.

There have been fewer studies of earthquake source parameters in ENA in comparison with the WUS, mainly because of the relatively small number of earthquakes available for study in ENA. Shi et al. (1998) analyzed 49 small-to-moderate sized earthquakes in the northeastern US and found that stress drops tend to decrease with decreasing seismic moment below a threshold moment of about 2×10^{13} Nm (~ M_W 2.8), suggesting a breakdown in self-similarity. Viegas et al. (2010) found high stress drops (median value ~ 20 MPa, converted to Brune

stress drops) and no evidence for magnitude dependence in the range M_W 2-5 for the 2002 Au Sable Forks, NY, mainshock and a few aftershocks. Boatwright et al. (2011) analyzed four moderate earthquakes (M_W 4.4-5.8) in northeastern North America and obtained Brune stress drops ranging from 13 to 42 MPa. Viegas (2012) determined a high stress drop (~ 20 MPa Brune stress drop) for the 2010 M_W 3.4 Germantown, Maryland, earthquake. Those studies used a variety of methods and data, and different corner frequency and stress drop values were obtained for common earthquakes. For example, Viegas et al. (2010) estimated a corner frequency of 1.7 Hz for the 2002 Au Sable Forks mainshock, whereas Boatwright et al. (2011) found a value of 1.34 Hz for the same earthquake. Such a difference in corner frequency translates to a factor of two in stress drop estimates because stress drop is proportional to the cube of corner frequency. Nevertheless, there is generally an agreement that some ENA earthquakes have high stress drops (e.g., Shi et al., 1998; Viegas et al., 2010; Boatwright et al., 2011; Viegas 2012, and references therein).

For the 2011 Mineral, Virginia mainshock, Ellsworth et al. (2012) used a multi-window spectral ratio method to estimate a stress drop of 50-75 MPa. They determined stress drops in excess of 100 MPa for some aftershocks. They proposed that the Mineral shock was an example of nearly complete stress drop (i.e., the stress drop was equal to the pre-earthquake shear stress). Hartzell et al., (2013) performed a finite-fault slip inversion for the Mineral mainshock and estimated peak stress drop in the range 30-50 MPa, and an average stress drop of 15-25 MPa. Boyd et al., (2017) used the empirical Greens function spectral ratio method to estimate a mainshock stress drop of 17-39 MPa. These previous studies indicate that the stress drop of the Mineral shock was large, even in relation to other eastern North American shocks.

Large variability persists in source parameter studies. Most often, stress drop measurements are based either directly or indirectly on determination of source spectrum corner frequency. Accurate determination of the corner frequency can be challenging, particularly for small earthquakes, because it requires effective path and site effects corrections. The empirical Greens function (EGF), also known as the spectral ratio method, is an attractive approach to determine corner frequencies because it effectively removes the propagation and site effects for co-located earthquakes with similar focal mechanism (e.g., Hough, 1997; Ide et al., 2003; Viegas et al., 2010; Abercrombie, 2015; Huang et al., 2016). However, the EGF method is often limited because it is not always possible to find event pairs that are co-located and have the same focal mechanism. In practice, it may be necessary to relax these requirements with the result that path effects are not entirely cancelled in the spectral ratio. Estimates of the moment ratio may be affected to the extent that the focal mechanisms differ. Directivity can affect the corner frequency estimate, and increase inter-station variation of the corner frequency estimates.

Imanishi and Ellsworth (2006) proposed a multi-window spectral ratio method to obtain stable spectral ratios by stacking the ratios calculated from moving windows taken along the record following the direct waves. Mayeda et al. (2007) showed that the use of S-wave coda reduces the inter-station variation of spectral ratios by a factor of 3 compared to the use of the direct S-wave. Abercrombie (2013) compared direct wave and coda wave stress drop measurements for the 2008 Wells, Nevada, earthquake sequence, and found that the source spectral ratios from the direct S-waves and coda waves are similar for the same pairs of earthquakes. Somei et al. (2014) applied a S-wave coda spectral ratio analysis on 17 inland crustal earthquake sequences in Japan.

Finally, quantification of uncertainties in source parameter estimates is a difficult problem. It has been noticed, in spectral ratio studies, that the corner frequency of the smaller earthquake of an event pair is less well resolved (Hough and Dreger, 1995; Viegas et al., 2010; Abercrombie, 2013). Many previous studies simply measure the inter-station variation of corner frequency estimates without explicitly considering the model fitting constraints or limited bandwidth of the data. Godano et al. (2015) and Garcia-Aristizabal et al. (2016) addressed the issue for error estimation by applying a robust Bayesian approach to estimate source parameters and their uncertainties.

In this study, we apply a multi-window coda spectral ratio method to obtain corner frequency and stress drop estimates for 46 earthquakes with Mw ranging from 0.71 to 5.65 in the 2011 Mineral, Virginia, earthquake sequence. Quantitative criteria are presented to select quality event pairs to remove path and site effects effectively. We model the source spectral ratios with an omega-square source model (Brune, 1970, 1971) using a Bayesian approach to estimate corner frequencies and uncertainties. We discuss the dependence of stress drops on earthquake size (i.e., seismic moment or M_W) and focal depth. We also examine the temporal and spatial variation of stress drops.

4.2 Dataset

The 2011 Mw 5.65 Mineral, Virginia earthquake occurred in the central Virginia seismic zone and was a complex rupture comprised of multiple subevents in a small fault area centered at depths between ~ 6 to 8 km (Chapman, 2013; Hartzell et al., 2013; Motazedian and Ma, 2014). The mainshock was recorded by a few stations at local to regional distances. Figure

4.1a shows all broadband stations within 400 km used in determining the corner frequency of the mainshock. Those stations were sampled at 40, 100 or 200 samples/s. Unlike the mainshock, the aftershocks were very well-recorded locally by more than 30 temporary stations deployed shortly after the mainshock. The instruments were a mixture of short-period (2 Hz) and broadband instruments, with sampling rates of 100 or 200 samples/s. Wu et al. (2015) conducted a comprehensive study of the aftershock sequence and obtained a complete catalog of thousands of earthquake locations and hundreds of focal mechanism solutions. The aftershocks are shallow, with focal depths ranging from ~ 2 to 10 km. Aftershocks near the mainshock define a tabular zone with orientation similar to the mainshock fault plane, and another group of aftershocks occurred 10-20 km to the northeast and was interpreted to have been triggered by Coulomb stress change caused by the mainshock (Wu et al., 2015). The 46 earthquakes and the temporary stations used in this study are shown in Figure 4.1b. Herrmann (2011) determined moment tensor solutions for the mainshock and 16 aftershocks (M_W 1.6-3.9). While the moment magnitude of the mainshock was well constrained, those of the small aftershocks tend to have large uncertainties. Therefore, we estimate the moment magnitude of the aftershocks from the spectral ratio analysis at low frequencies.

4.3 Method

We extend the multi-window spectral ratio method (Imanishi and Ellsworth, 2006) to the *S*-wave coda, and refer to it as the multi-window coda spectral ratio (MWCSR) method. We demonstrate that this method significantly reduces the inter-station variation of spectral ratios compared to conventional spectral ratio methods.

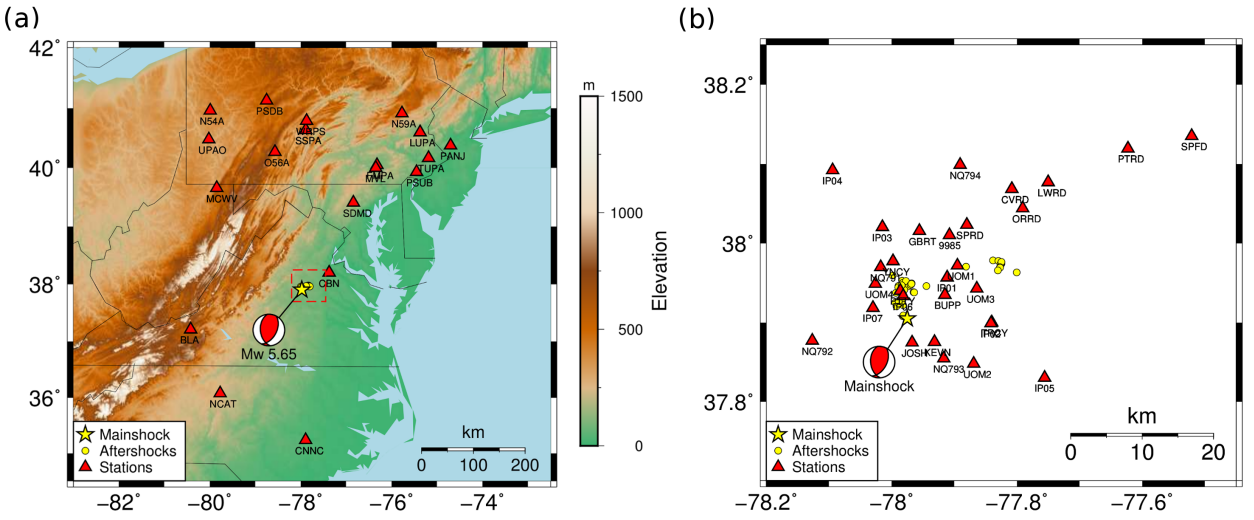

Figure 4.1: Earthquake epicenters and stations used in this study. (a) All broadband stations (filled triangles) within 400 km that recorded the 2011 M_W 5.65 Mineral, Virginia mainshock, which is shown as a filled star.; (b) The epicentral area is shown as a dashed rectangle in (a). Temporary stations (filled triangles) that recorded the aftershocks (filled circles). The station names are shown below the station symbols. The mainshock epicenter and focal mechanism are from Chapman (2013) and Herrmann (2011), respectively.

We generally follow the procedures of Somei et al. (2014) to process the data. In the following, we briefly describe the coda theory and our data processing steps for a mainshock-aftershock pair and an aftershock-aftershock pair (Fig. 4.2 and Fig. 4.4).

4.3.1 Event-pair and window selections

We select earthquakes that occurred close to each other to form event pairs. We require a maximum spatial separation of 10 km for mainshock-aftershock pairs and 3 km for aftershock-aftershock pairs in consideration of the very different station distributions in the two cases. Large aftershocks with M_W 3 and greater are used as EGF events in conjunction with the mainshock. The minimum magnitude difference of aftershock-aftershock pairs is set at 0.8.

According to previous coda studies, at lapse time greater than roughly 1.5 to 2 times the S-wave traveltime, the coda spectral amplitude is proportional to the source spectral amplitude of the S-wave and the decay rate of the coda amplitude with lapse time becomes stationary, independent of magnitude and hypocentral distance (Aki and Chouet, 1975; Rautian and Khalturin, 1978; Somei et al., 2014; Frankel, 2015; Wu et al., 2016). The assumption is that the S-wave coda, being made up of scattered S-waves that take a wide range of paths between source and receiver, is largely independent of source radiation pattern and rupture complexities, such as directivity, at a sufficiently large lapse time. The spectral amplitude of the recorded S-wave at frequency f and hypocentral distance R can be represented as:

$$A_S(f,R) = CS(f)G(f)I(f)R^{-\gamma}e^{-\pi fR/Q(f)\beta} \tag{4.1}$$

where C is the S-wave radiation pattern factor, $S(f)$ is the source spectrum, $G(f)$ is the site amplification, $I(f)$ is the instrument response, γ is the coefficient of geometrical spreading, $Q(f)$ is the S-wave quality factor and β is the average S-wave velocity. The term $R^{-\gamma}$ represents the geometrical spreading effect, and the exponential term describes the anelastic attenuation effect. The amplitude spectrum of the coda $A_C(f,t_C)$ at some lapse time t_C after the earthquake origin time is given by:

$$A_C(f,t_C) = S(f)G(f)I(f)E(f,t_C) \tag{4.2}$$

where $E(f,t_C)$ is a function that describes the decay of coda as a function of frequency f and lapse time t_C.

For two exactly co-located earthquakes with the same focal mechanism, taking the spectral ratio at a given station should effectively remove the path and site effects by cancellation, leaving an estimate of the source spectral ratio. However, it is not always easy to find many event pairs that are closely co-located with the same focal mechanism. We have found that, in cases where the events are not very closely separated in space and lack identical focal mechanisms, the propagation terms and radiation pattern will not effectively cancel if the direct S-waves are used to form the spectral ratio. Finite-fault rupture complexity, such as directivity effects, may also cause problems. Moreover, the azimuthal and distance coverage of recording stations is not usually sufficient to average out those effects. In that case, the coda should perform better than the direct S-wave because the coda has the property of homogenizing the energy spatially (Sato et al., 2012; Mayeda et al., 2007; Somei et al., 2014). However, in forming the spectral ratio, we must ensure that the respective numerator and denominator terms $E(f, t_C)$ (equation 4.2) exhibit common amplitude decay during the lapse time intervals chosen for analysis.

We define the beginning of the coda window at lapse time $1.5T_S$ at stations distant from the epicenter (¿100 km) and at lapse time $2T_S$ for close-in stations (< 100 km), where T_S denotes the S-wave traveltime. The entire coda window length is selected to be 30 seconds and 20 seconds for mainshock-aftershock pairs and aftershock-aftershock pairs, respectively. This difference in analysis window length was necessary because of the smaller signal-to-noise ratios of the smaller magnitude aftershocks, compared to the mainshock, at large lapse times. We divide the entire coda window into 5 successive sub-windows by overlapping the sub-windows by 1/2 of the sub-window duration. This procedure gives sub-window lengths of 10 seconds and 6.67 seconds for mainshock-aftershock pairs and aftershock-aftershock pairs,

respectively. Figure 4.2a shows the waveforms of the M_W 5.65 mainshock and a M_W 3.36 aftershock recorded at station BLA along with the coda window placements.

We then examine the decay of coda envelopes for event pairs in four frequency bands: 1-2 Hz, 2-4 Hz, 4-8 Hz and 8-16 Hz. This is done to be certain that the coda decay of both numerator and denominator events is nearly identical over a wide frequency range. The coda envelopes are smoothed using a moving average computed over a 10 second interval, starting immediately after the S-wave arrival (Fig. 4.2). In the selected coda window, we calculate the envelope amplitude ratio for the large (numerator) and small (denominator) events in a pair and normalize it by the average ratio of the entire coda window (Fig. 4.2). If the coda envelopes decay in the same manner for the two events, the normalized envelope ratio should be close to 1 over the entire coda analysis window. We require the mean and standard deviation of the normalized envelope ratios to be 1.0 ± 0.1 and 0.05, respectively, over the coda analysis window. This scheme can effectively detect cases where small earthquakes are buried in the analyzed coda window, a circumstance that would adversely affect the estimation of moment ratios and corner frequencies.

4.3.2 Spectral ratios

For qualified event pairs that meet our selection criteria, we calculate the spectral ratios of both the direct S-wave window and multiple coda windows on three-component velocity seismograms that have been rotated to radial, transverse, and vertical directions. Transverse components are used to pick S-wave arrivals. The spectra of the S-wave window and coda windows as well as the pre-P noise window are calculated using a multi-taper approach

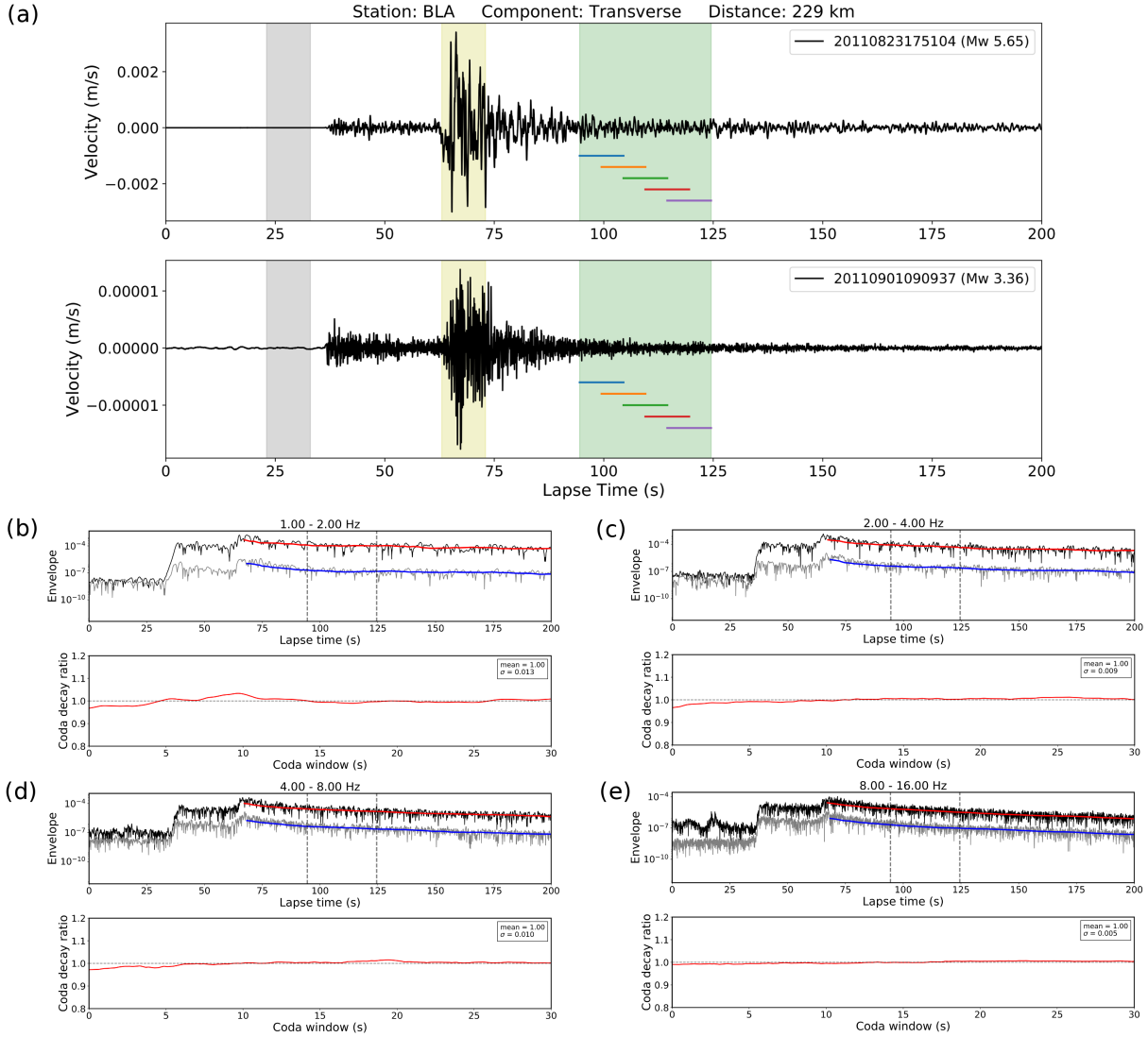

Figure 4.2: The mainshock and an M_W 3.36 aftershock recorded at station BLA at an epicentral distance of 229 km. (a). The transverse-component velocity records of the two events. The shaded areas from left to right denote the pre-signal noise window, the direct S-wave window, and the whole coda window. The short horizontal bars below the seismograms within the coda window mark the placement of 5 sub-divided short coda windows; (b)-(e). Comparison of the coda decay characteristics for the large and small events in four frequency bands: 1-2 Hz (b); 2-4 Hz (c); 4-8 Hz (d) and 8-16 Hz (e). In (b)-(e), the top panels show the narrow-band original and smoothed envelopes. The vertical dashed lines indicate the coda window. The bottom panels show the normalized coda decay ratio for the coda window (see text for details). The mean value and standard deviation of coda decay ratios are shown at the upper-right corner of the bottom panels.

(Prieto et al., 2009). We set an upper bound frequency of 80% of the Nyquist frequency for our dataset. We obtain the final coda spectral ratios by stacking the ratios calculated from the multiple sub-windows in logarithmic space. The spectral ratios are then re-sampled equally to 100 points between 0.1 and 100 Hz on a logarithmic scale to equalize the weight of low and high frequency in the source model fitting. We further stack the spectral ratios from all stations with a signal-to-noise ratio (SNR) of at least 2 at distant stations (> 100 km) and 3 at close-in stations (< 100 km) for both large and small events. We only accept event pairs showing a clear low-frequency plateau and high-frequency asymptote as predicted by the omega-square source model. In cases where the coda waves suffer from low SNR at low frequencies (typically below 1 Hz), we combine the spectral ratios of the direct S-wave at low frequencies with multi-window coda spectral ratios at high frequencies. The justification for this is based on our finding that ratios derived from coda waves always show smaller inter-station variation than ratios derived from direct S-waves at frequencies greater than 1 Hz, while showing stacked spectral ratios that are very similar to those of the direct waves (Fig. 4.3 and Fig. 4.5). In fact, the direct S-wave spectral ratio was only used in this study for mainshock-aftershock pairs to resolve the corner frequency of the mainshock, which was found to be beyond the available bandwidth of coda due to the lack of close-in stations (Fig. 4.3). For aftershock pairs, the multi-window spectral ratios are always preferred because they show reduced scatter across the whole frequency range needed to resolve corner frequencies of both large and small events (Fig. 4.5). The error-bars in the stacked spectral ratios (Fig. 4.3 and Fig. 4.5) represent the standard deviation of measurements from different stations, which are taken as the weights in the model fitting step discussed below.

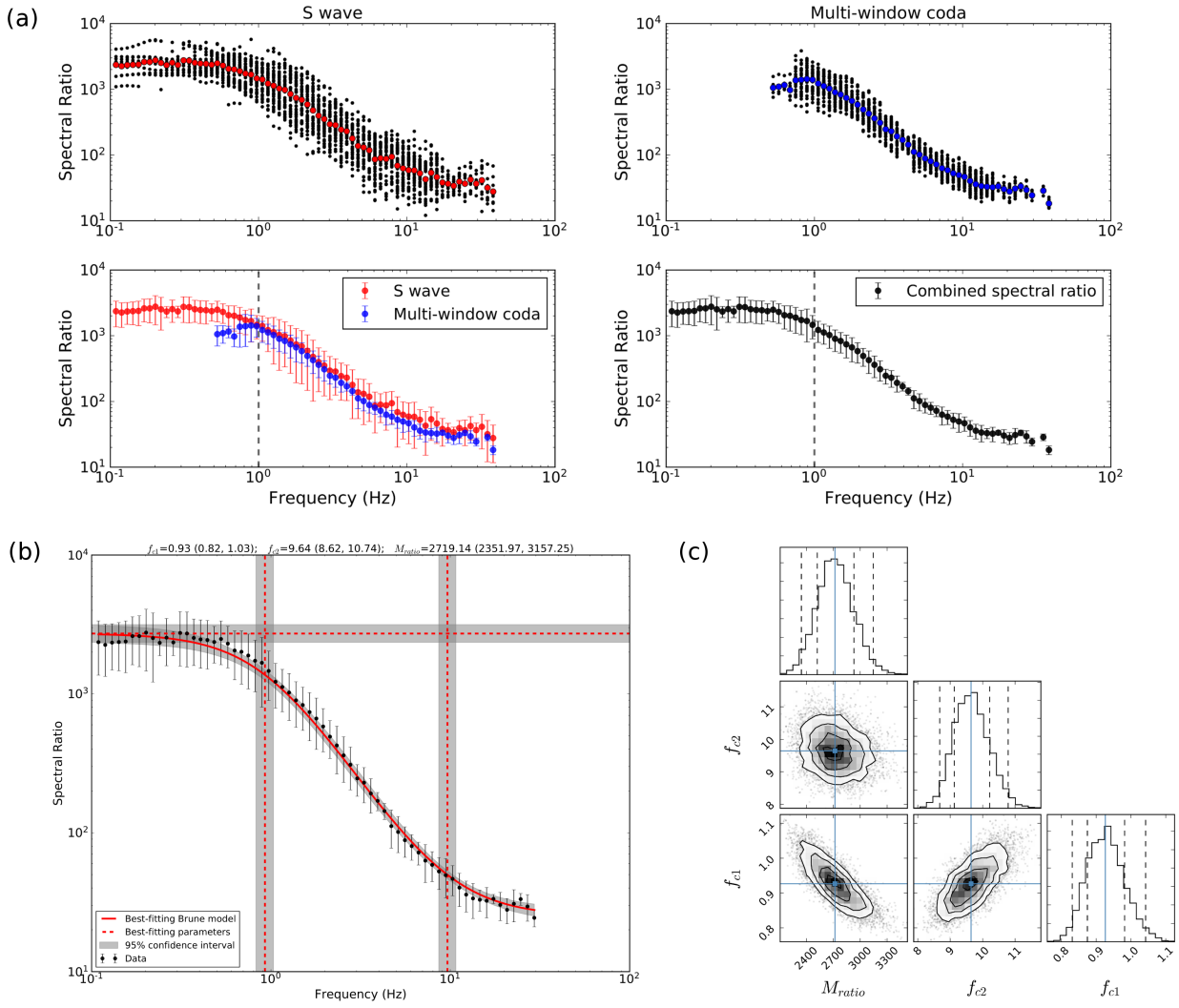

Figure 4.3: The spectral ratios and corner frequency estimates of the mainshock-aftershock pair shown in Figure 4.2. (a). S-wave spectral ratios (upper left) and multi-window coda spectral ratios (upper right) measured at all stations. Note the similar stacked spectral ratios for S-wave and coda and much reduced inter-station variation for coda above 1 Hz (lower right). The error-bars denote the standard deviation of measurements at many stations. The combined spectral ratios are obtained with low-frequency S-wave measurements and high-frequency coda measurements (lower left). (b). Bayesian model fitting. The dashed lines show the best-fitting model parameters (f_{c1}, f_{c2}, M_{ratio}). The shaded areas show the 95% confidence intervals of the estimated parameters. The values are shown above the figure. (c). The posterior distributions of the model parameters. The diagonal panels display the posterior probability density function (PDF) of M_{ratio} (top), f_{c2} (middle), and f_{c1} (bottom). The vertical dashed lines mark the 68% and 95% confidence intervals. The off-diagonal panels show the two-dimensional projections of the posterior samples (gray dots) of the Markov chain Monte Carlo simulations, in which the contours represent 0.5, 1, 1.5, and 2 standard deviations.

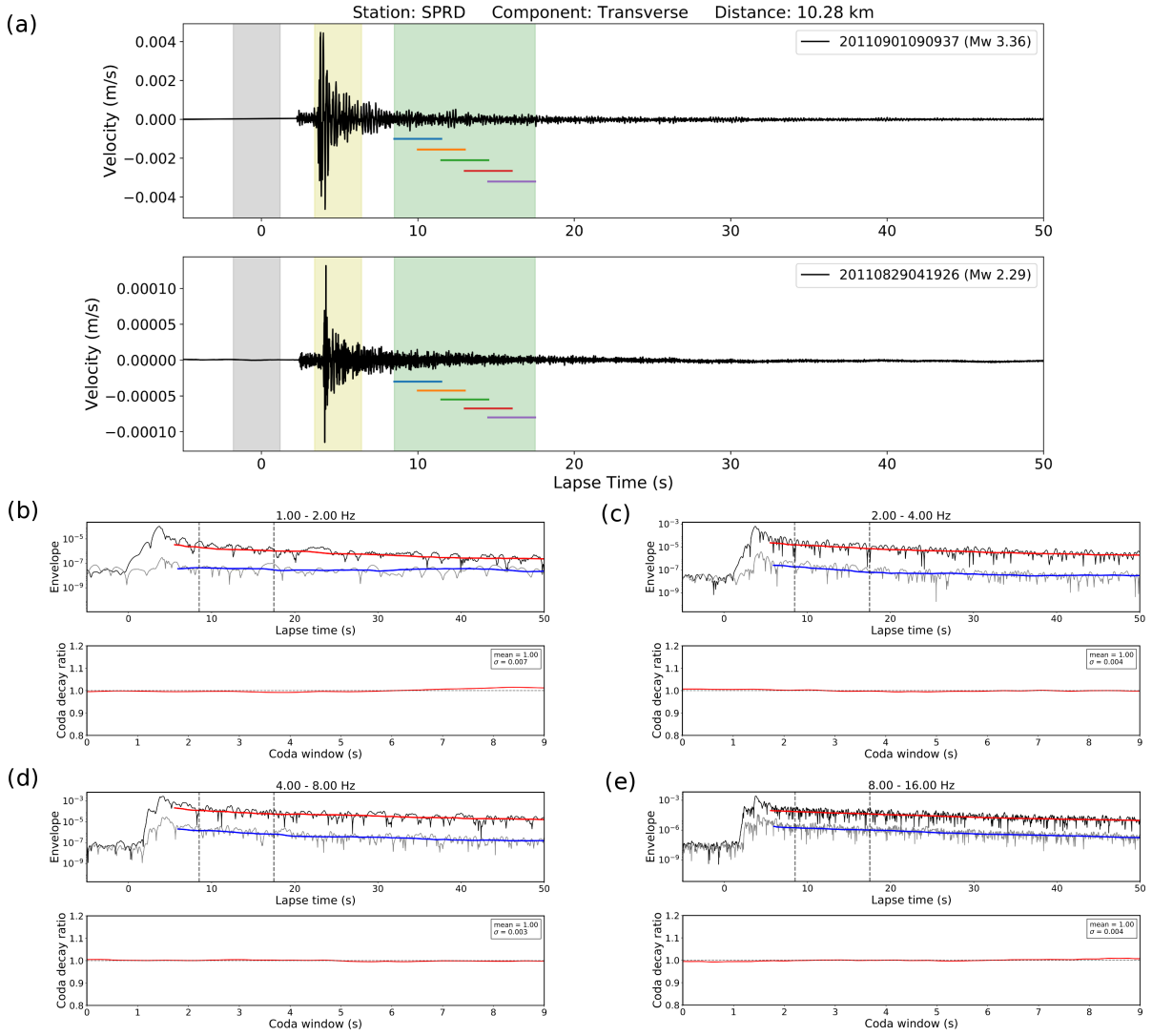

Figure 4.4: An M_W 3.36 aftershock and an M_W 2.29 aftershock recorded at station SPRD at ~10 km epicentral distance. (a). The transverse-component velocity records of the two events. The shaded areas from left to right denote the pre-signal noise window, the direct S-wave window, and the whole coda window. The short horizontal bars below the seismograms within the coda window mark the placement of 5 subdivided short coda windows; (b)-(e). Comparison of the coda decay characteristics for the large and small events in four frequency bands: 1-2 Hz (b); 2-4 Hz (c); 4-8 Hz (d) and 8-16 Hz (e). In (b)-(e), the top panels show the narrow-band original and smoothed envelopes. The vertical dashed lines indicate the coda window. The bottom panels show the normalized coda decay ratio for the coda window (see text for details). The mean value and standard deviation of coda decay ratios are shown at the upper-right corner of the bottom panels.

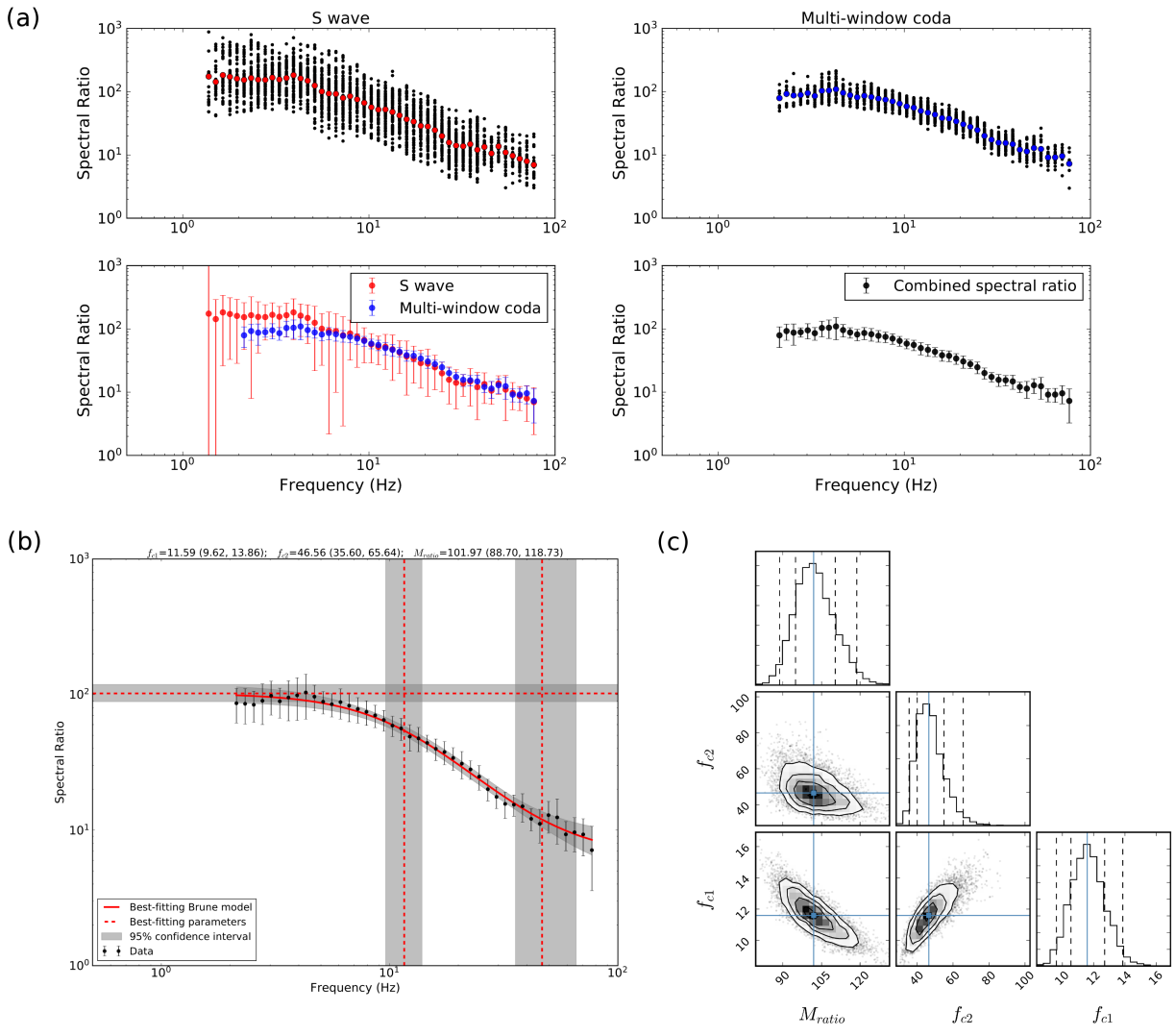

Figure 4.5: Same as Figure 4.3 but for the aftershock-aftershock pair shown in Figure 4.4.

4.3.3 Corner frequency estimates

We fit the stacked multi-window spectral ratios to estimate corner frequencies for the large (f_{c1}) and small (f_{c2}) events, as well as the seismic moment ratio of the two events assuming the Brune source spectral model (Brune, 1970, 1971),

$$\frac{u_1(f)}{u_2(f)} = \frac{M_{01}}{M_{02}} \left(\frac{1 + \left(\frac{f}{f_{c2}} \right)^2}{1 + \left(\frac{f}{f_{c1}} \right)^2} \right) = M_{ratio} \left(\frac{1 + \left(\frac{f}{f_{c2}} \right)^2}{1 + \left(\frac{f}{f_{c1}} \right)^2} \right) \tag{4.3}$$

where $M_{ratio}(M_{01}/M_{02})$ is the seismic moment ratio of the large and small events, and f_{c1} and f_{c2} are the corner frequencies of the large and small events, respectively. We tested both Brune (1970, 1971) and Boatwright (1980) source models, and found that the Brune model generally fits our data slightly better.

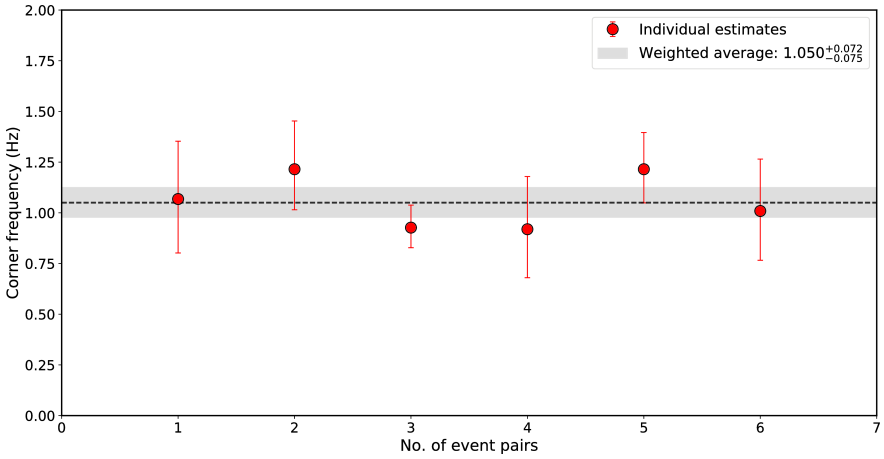

Figure 4.6: Six individual estimates of the mainshock corner frequency from six different EGF events. The filled circles with error-bars denote best-estimates with 95% confidence intervals. The horizontal dashed line represents the weighted-average corner frequency. The shaded area shows the weighted uncertainty estimate.

We use a Bayesian approach to fit the spectral ratios with the Brune model to determine the two corner frequencies f_{c1}, f_{c2} and the M_{ratio} simultaneously. A Markov chain Monte Carlo (MCMC) algorithm employed through the Python package PyMC3 (Salvatier et al., 2016) is used to sample the posterior distribution of the model parameters $(f_{c1}, f_{c2}, M_{ratio})$. Uncertainty estimates are derived from the posterior probability distribution, which we computed from the prior information on model parameters and the likelihood function according to Bayes theorem. We assume a log-normal distribution of the prior probability for the model parameters, and a normal distribution for the likelihood function following Godano et al. (2015) and Garcia-Aristizabal et al. (2016). The best estimates and uncertainties can be determined using the samples drawn from the posterior distributions (Fig. 4.3c). This approach has the advantage that the trade-offs between model parameters are fully accounted for such that the estimated uncertainties are more realistic compared to commonly used non-linear least-squares fitting methods. Figure 4.3b shows the best-fitting Brune source model with best estimates of $f_{c1}, f_{c2}, M_{ratio}$ and their 95% confidence intervals. Figure 4.3c shows the posterior distributions of model parameters from which the confidence intervals are drawn. We are able to find several EGF events to form event pairs for the mainshock and some large aftershocks. In such cases, we calculate the weighted mean of the corner frequencies from individual estimates, in which the weights are the inverse of corresponding errors (Abercrombie, 2014). This calculation is also conducted in logarithmic space. Figure 4.6 summarizes the six individual estimates of the mainshock corner frequency using different EGF events. While individual estimates fall into a small range, the weighted average gives the final estimate of the mainshock corner frequency $1.05(+0.072/-0.075)$ Hz, which is consistent with the direct observation from a triggered strong-motion recording at the

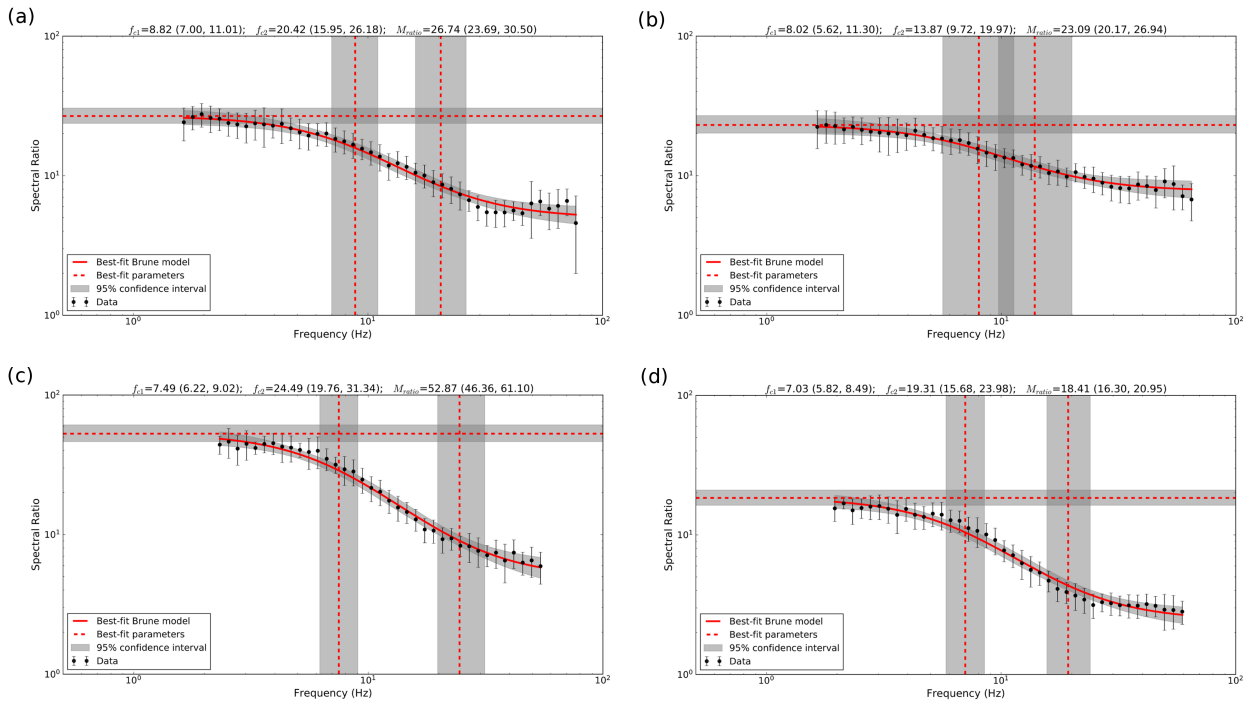

Figure 4.7: Another four examples of event pairs. (a) event 14 (M_W 3.36) versus event 9 (M_W 2.60); (b) event 14 (M_W 3.36) versus event 10 (M_W 2.78); (c) event 36 (M_W 3.17) versus event 11 (M_W 2.29); (d) event 36 (M_W 3.36) versus event 31 (M_W 2.33). The events were selected to show that very similar corner frequencies are obtained using different EGF events ((a) and (b); (c) and (d)).

Dominion Inc. North Anna Power Station, 23 km from the epicenter (Chapman, 2015).

4.4 Results

Figure 4.7 shows another 4 spectral ratios along with best-fitting parameters for different event pairs. The observed source spectral ratios are well-explained by the omega-square source model and reliable estimates of the corner frequencies can be made.

Assuming a circular crack model, we calculate the Brune stress drop (hereafter stress drop)

$\Delta\sigma$ from seismic moment M_0 and corner frequency f_c (Eshelby, 1957; Brune, 1970, 1971):

$$\Delta\sigma = \frac{7}{16}\frac{M_0}{r^3} = \frac{7M_0}{16}\left(\frac{f_c}{\kappa\beta}\right)^3, \qquad r = \frac{\kappa\beta}{f_c} \tag{4.4}$$

where r is the source radius, β is the shear-wave velocity at the source, and κ is a constant depending on assumed source model. We use an appropriate S-wave velocity of 3.5 km/s according to Chapman (2013) and Davenport et al. (2015). For commonly used models, $\kappa = 0.372$ for the Brune model (Brune, 1970, 1971) and $\kappa = 0.21$ for S-waves in the Madariaga model (Madariaga, 1976). For the same corner frequency value, the Madariaga stress drop is ~5.6 times larger than the Brune stress drop. This difference in κ is important when comparing stress drop estimates determined from studies using different source models.

We plot the corner frequency against seismic moment for all 46 earthquakes in Figure 4.8. The stress drops span a wide range of ~0.1-100 MPa, with all of the aftershocks showing smaller stress drops than that of the mainshock. The corner frequencies of earthquakes with M_W 2 and greater are generally better constrained than the smaller earthquakes. The stress drop of the mainshock is calculated to be 86 MPa with a 95% confidence interval 70 to 107 MPa, which is unusually high even for ENA (Shi et al., 1998; Viegas et al., 2010; Boatwright et al., 2011). The inferred source radius from equation (4.5) is 1.24 km (95% confidence interval 1.16 - 1.33 km) which is consistent with the compact rupture of the mainshock determined by previous studies (Chapman, 2013; Hartzell et al., 2013; Motazedian and Ma, 2014). The largest aftershock (M_W 4.16) also has a high stress drop of 79 MPa (60-

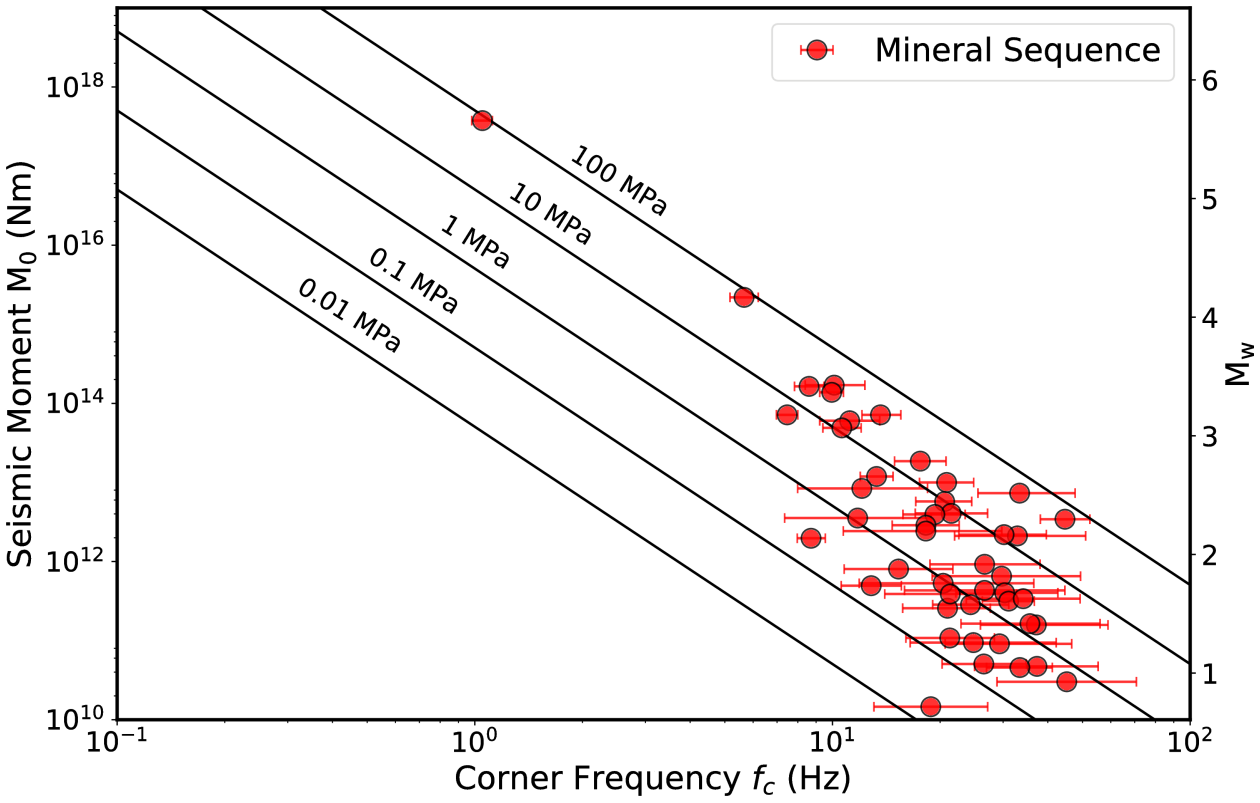

Figure 4.8: Seismic moment versus corner frequency. The solid diagonal lines mark lines of constant stress drops of 0.01, 0.1, 1, 10, and 100 MPa. The filled circles show best-estimate corner frequencies with 95% confidence intervals indicated by the error-bars.

103 MPa). This aftershock is significantly shallower (~3 km depth) than the mainshock and has a different focal mechanism (Herrmann, 2011). The stress drop measurements appear to decrease systematically with decreasing magnitude, for events with magnitude less than approximately M_W 2.5, suggesting a possible breakdown of self-similarity at small magnitudes. We will discuss this observation further in the following section. Stress drop estimates for large earthquakes (M_W 2 and greater) range from ~1-100 MPa, whereas those of the small ones (less than M_W 2) are on the order of 0.1 to 4 MPa.

4.5 Discussion

4.5.1 Magnitude dependence

We plot stress drop versus moment magnitude in Figure 4.9a and source radius versus moment magnitude in Figure 4.9b. Taken at face value, these results imply a change from constant stress drop scaling for earthquakes with M_W greater than approximately 2.5 to constant source radius scaling for smaller earthquakes. However, several studies (e.g., Hough, 1996; Ide and Beroza, 2001; Ide et al., 2003) have shown that some cases of reported magnitude dependence of stress drop can be attributed to limited data bandwidth. Figure 4.9a shows the upper limits of stress drop resolution of our dataset, based on 80%, 70% and 60% of the Nyquist frequency (80, 70 and 60 Hz). It appears that most of our stress drop estimates lie well within the resolvable range, with few observations near the limit of resolution. Shi et al. (1998) also found an apparent dependence of stress drop on seismic moment below a threshold magnitude of about 2.8, which they interpreted as a consequence of a nearly constant rupture radius for small earthquakes (Dysart et al., 1988; Scholz, 1988, 1990). However, we could not measure corner frequencies for many earthquakes with magnitudes less than 2.0 because of either poor SNR at very high frequencies or lack of available event pairs satisfying our strict selection criteria. This introduces a possible sampling bias that may give rise to an apparent deviation from constant stress drop scaling. On the other hand, if constant stress drop scaling actually applies throughout the magnitude range of our dataset, it clearly requires an increase in the variation of stress drop for the smaller events. While the uncertainty of our stress drop measurements does increase with decreasing magnitude, our error estimates for the small shocks (error-bars in Fig. 4.9) are not so large that a breakdown in

constant stress drop scaling can be ruled out. Nevertheless, we are mainly concerned about the larger earthquakes, like the Mineral mainshock, that contribute to seismic hazard. The stress drops for all events are between 0.02 MPa and 86 MPa with a median stress drop of 3 MPa. The median stress drop is 13 MPa for earthquakes with magnitude greater than 2.0. The median stress drop of the smaller events (less than M_W 2.0) is 0.7 MPa. An average stress drop of ~10 MPa agrees with previous studies in ENA (Shi et al., 1998; Viegas et al., 2010; Boatwright et al., 2011) and is consistent with typical values used for ground-motion prediction in ENA (e.g., Atkinson and Boore, 2006). The stress drops determined here for the Mineral mainshock and the largest aftershock (86 MPa and 79 MPa, respectively) are some of the highest determined for ENA. For comparison, we plot in Figure 4.10 the results from some recent studies in ENA. Those results were converted to the Brune source model using shear-wave velocities suggested by individual studies (Shi et al., 1998; Viegas et al., 2010; Boatwright et al., 2011; Viegas, 2012; Boyd et al., 2017). The Boyd et al. (2017) results shown in Figure 4.10 are for the Mineral mainshock and six aftershocks. Those estimates are somewhat smaller than the corresponding stress drop estimates determined in this study. Eight of the eleven stress drop estimates for $M_W > 4.0$ (Fig. 4.10) are greater than 10 MPa. The high stress drops for these events indicate high frictional strength of the faults. Possible mechanisms that could contribute to higher fault strength for intraplate earthquakes are lower slip rates, smaller cumulative fault offsets, and shorter total fault lengths (Scholz et al. 1986). Our results for the Mineral mainshock and some of the aftershocks are consistent with the suggestion of Ellsworth et al. (2012) that those events are examples of near complete stress drop.

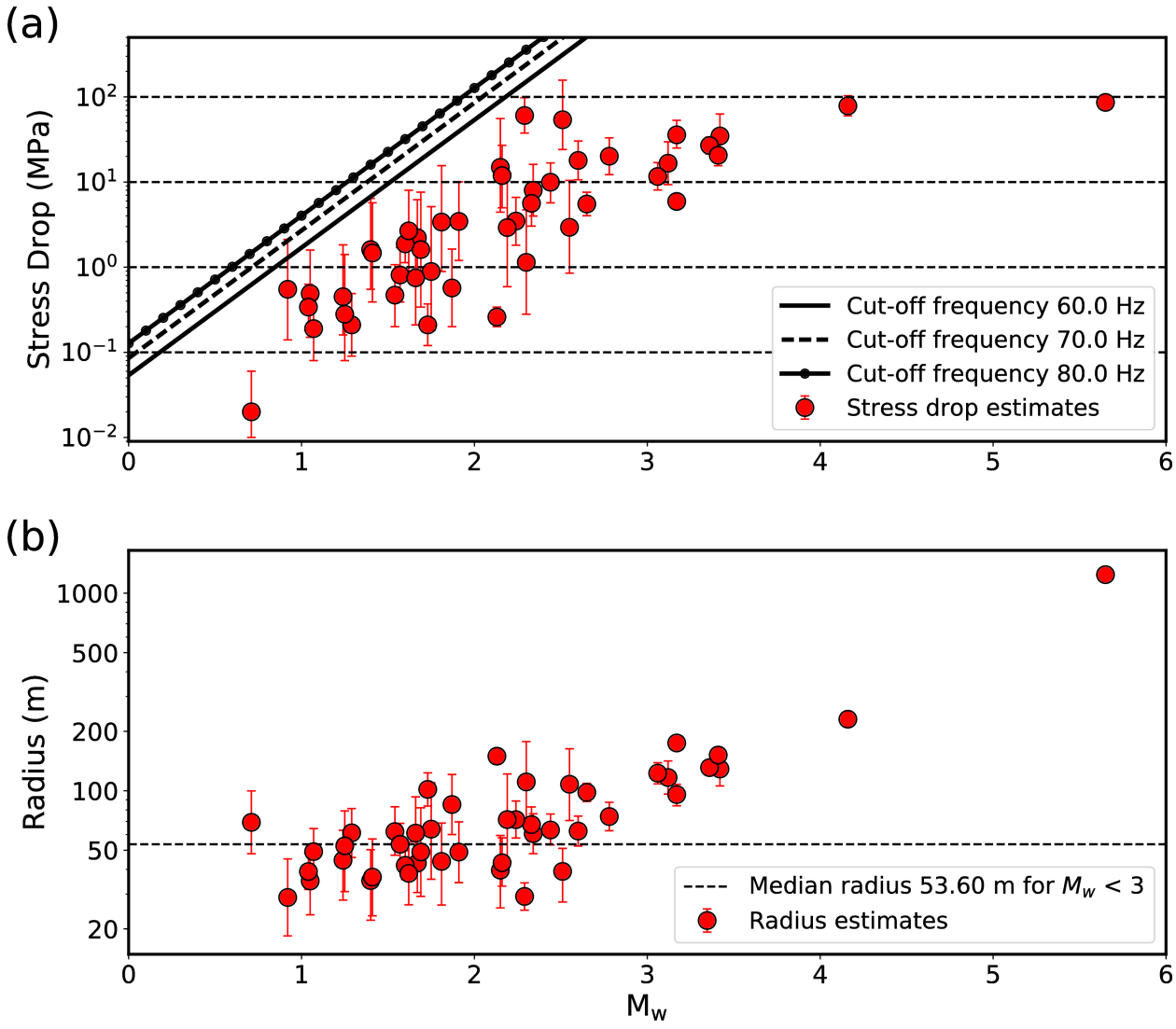

Figure 4.9: (a) Stress drop versus moment magnitude M_W, assuming the Brune (1970,1971) model. The error-bars denote the 95% confidence interval of stress drop estimates. The three oblique lines show possible cut-off frequencies of 60 Hz (solid), 70 Hz (dashed), and 80 Hz (dotted solid). Note that most of the estimates lie well within the resolvable frequency range. (b). Source radii and 95% confidence intervals. The dashed line shows the median source radius for $M_W < 3$.

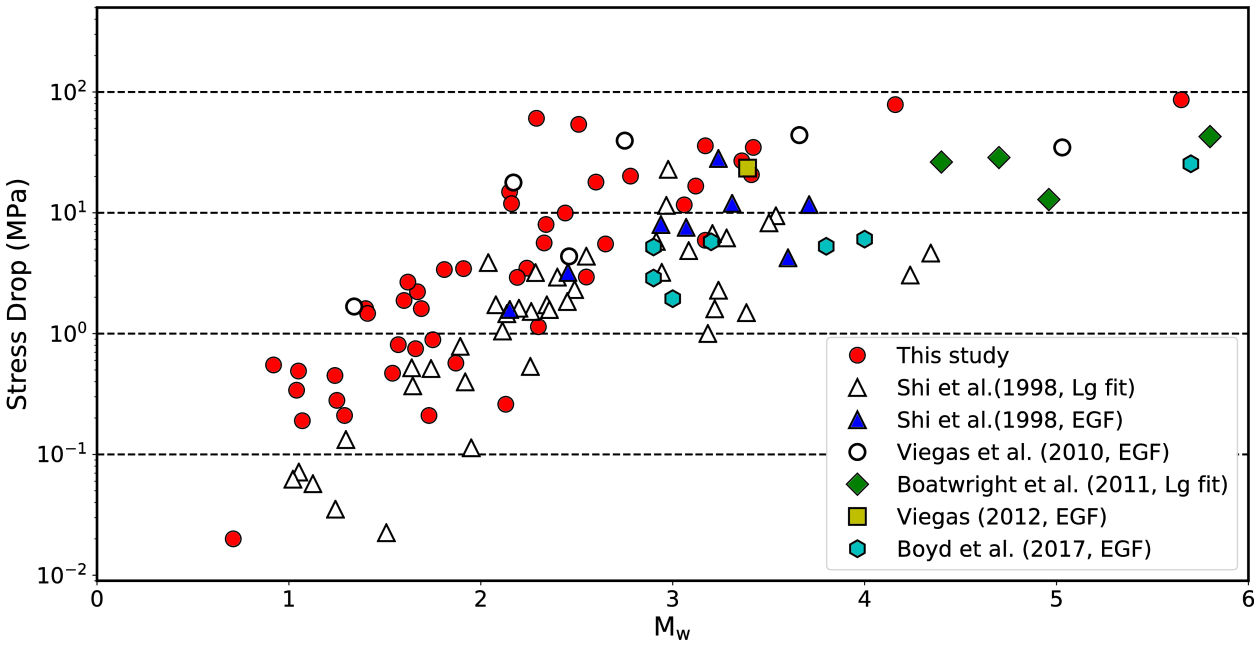

Figure 4.10: Comparison of stress drop results in this study with previous studies in ENA. All results from previous studies (Shi et al., 1998; Viegas et al., 2010; Boatwright et al., 2011; Viegas 2012) were converted to the Brune source model using shear-wave velocities suggested in the individual studies.

4.5.2 Depth dependence

Hough (2014) suggested that stress drops of injection-induced earthquakes in the CEUS are systematically lower than tectonic earthquakes and attributed this discrepancy to the shallow focal depth of the induced earthquakes. We examine the depth dependence of stress drops for the Mineral sequence (Fig. 4.11), even though there is only a very limited range of focal depths (~1.2-8 km) in our dataset. No obvious depth dependence is observed, and the variation of stress drops appears to be controlled by magnitude (Fig. 4.11). Considering the very similar depth range of the Mineral sequence and induced earthquakes in Oklahoma, a comparative study of the stress drops of those induced earthquakes and the Mineral sequence

would be useful.

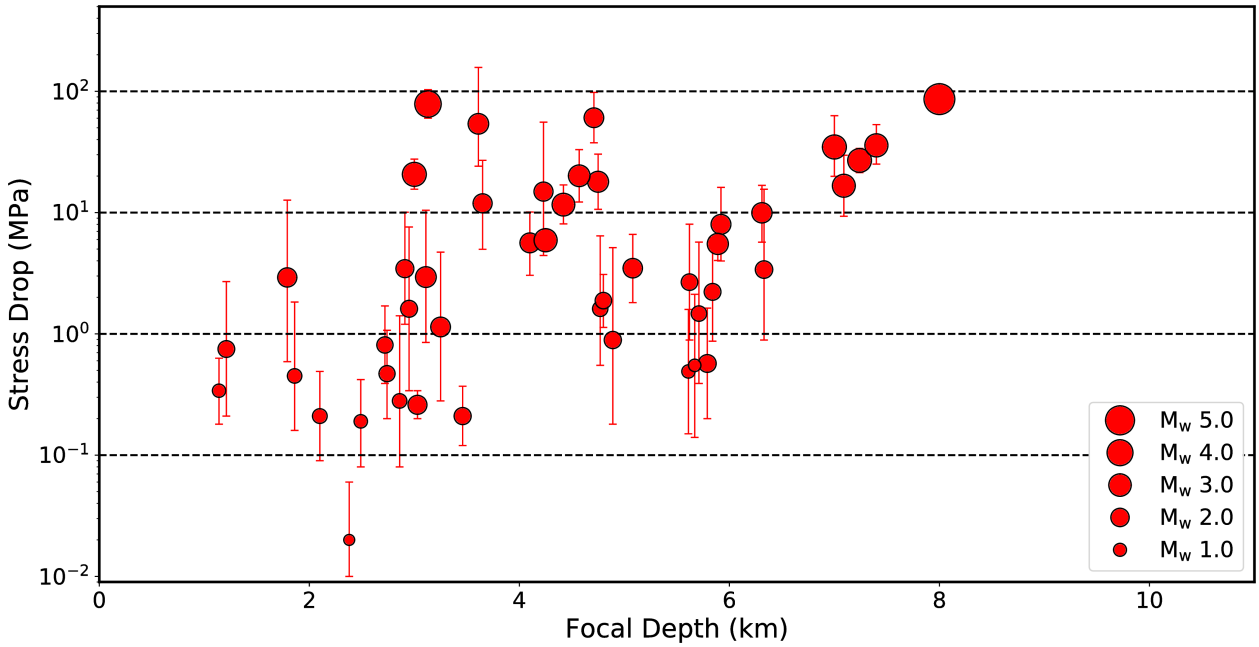

Figure 4.11: Stress drop versus focal depth. The error-bars denote 95% confidence intervals of the stress drop estimates. The symbol sizes are proportional to the earthquake magnitudes.

4.5.3 Temporal and Spatial Variation

We examined the temporal and spatial distributions of stress drops in an effort to understand the large range of values we determined. In Figure 4.12, we show the stress drop estimates as a function of time. The times are converted to decimal days after 00:00:00 UTC on 23 August 2011 and plotted in a log scale to spread out the data points to aid visualization. At a first glance, the stress drops appear to decay through time up to around day 70. However, taking into account the magnitudes, we find that this apparent trend coincides with the distribution of the earthquake magnitudes: more large aftershocks occur in the early stage of an aftershock sequence as predicted by the Gutenberg-Richer relation (Gutenberg and

Richter, 1944) and Omori law (Utsu et al., 1995). The high stress drops of the two M_W 3 aftershocks that occurred in 2012 (day 162 and 219 in Fig. 4.12) validate this interpretation.

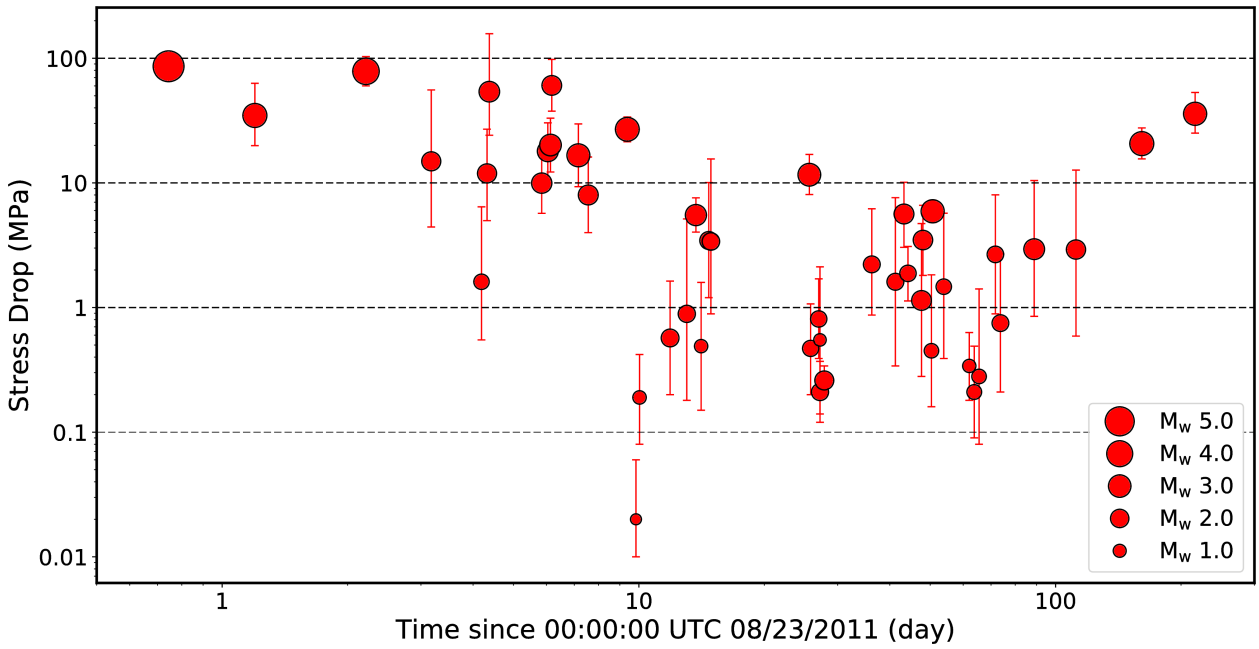

Figure 4.12: Temporal variation of stress drop estimates. The times were converted to decimal days starting from 00:00:00 UTC, 23 August, 2011 to aid visualization. The error-bars denote 95% confidence intervals of stress drop estimates. The symbol sizes are proportional to the earthquake magnitudes.

Figure 4.13 shows the spatial distribution of stress drops in map view and two cross-section views. The two profiles are selected to be approximately parallel (BB, N30°E) and perpendicular (AA, N120°E) to the strike direction of the tabular main aftershock cluster (Wu et al., 2015). The shallow aftershocks that occurred 10-20 km to the northeast of the mainshock (east of longitude -77.9°) are interpreted to have been triggered by positive Coulomb stress transfer from the mainshock on the order of ~0.2 bar (0.02 MPa) (Wu et al., 2015). Stress drops of earthquakes in the main aftershock cluster exhibit no clear spatial pattern and again

the magnitude seems to be the dominant factor of the stress drop variation. Interestingly, 11 aftershocks in the northeastern cluster show outstandingly low stress drops (< 1 MPa) even considering the fact that they are small (M_W 0.7-2.1). Those aftershocks are shallow (< 4 km depth) and have consistent focal mechanism nodal planes striking ~N20°W, different from the orientation of the mainshock fault plane (N28°E) (Herrmann, 2011; Chapman, 2013; Wu et al., 2015). Wu et al. (2015) suggest that the northwest-trending faults at shallow depth were in a near-critical stress condition prior to the mainshock. Our recent examination of Lidar images finds a strong correlation of the N20°W nodal plane strike direction of shallow aftershocks in the study region with a set of very prominent Lidar lineaments (Chapman et al., 2017; Horton et al., 2017). Those lineaments have a strong influence on the landscape in the study area, largely controlling the drainage pattern. The low stress drops that we have obtained for some of those shallow earthquakes that appear to be spatially associated with the Lidar lineaments suggest that those earthquakes may represent faulting on pre-existing joint planes.

4.6 Conclusions

We determine corner frequencies and stress drops for the 2011 M_W 5.65 Mineral, Virginia mainshock and 45 aftershocks (M_W 0.71-4.16). We apply a multi-window coda spectral ratio method and a Bayesian approach to estimate corner frequencies and associated uncertainties. In the process, we define quantitative criteria to select event pairs to ensure quality results. We estimated an unusually high stress drop of 86 MPa for the Mineral mainshock. Long healing times, high fault strength and low strain rates in an intraplate tectonic setting

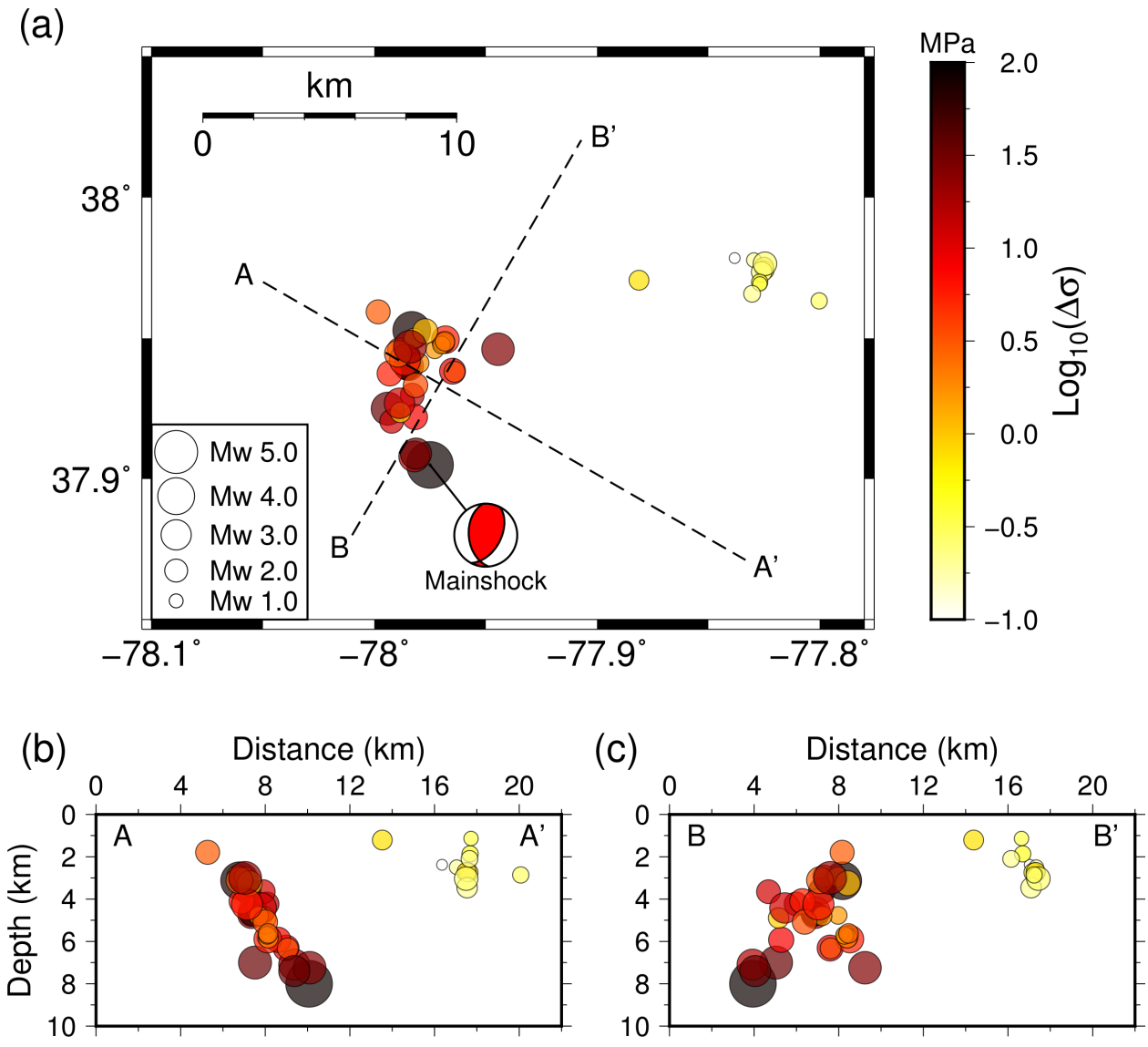

Figure 4.13: Spatial variation of stress drop estimates. (a) Mapview. The symbol sizes are proportional to the earthquake magnitudes. The two profiles (AA' and BB') are selected to be perpendicular and parallel, respectively, to the main aftershock cluster strike direction. (b). Cross-section view along profile A-A'. (c) Cross-section view along profile B-B'. Note the significantly lower stress drops for events to the northeast of the mainshock.

may be responsible for the high stress drop of the mainshock. Careful examination of the estimated stress drops for 46 earthquakes indicates a possible breakdown in self-similarity (constant-stress drop scaling with earthquake size) for small earthquakes below a certain size (~ M_W 2.5). For big earthquakes (M_W 3 and above), the stress drop values lie in a relatively small range of ~10-100 MPa. The estimated stress drops show no evidence of either depth dependence or temporal and spatial patterns. A group of small shallow earthquakes ~20 km away from the mainshock have anomalously low stress drops, possibly reflecting low fault strength (rupture along pre-existing joints) and/or a heterogeneous stress condition in our study area.

References

Abercrombie, R. E. (2013). Comparison of direct and coda wave stress drop measurements for the Wells, Nevada, earthquake sequence, *J. Geophys. Res.* **118**, no. 4, 1458-1470.

Abercrombie, R. E. (2014). Stress drops of repeating earthquakes on the San Andreas Fault at Parkfield, *Geophys. Res. Lett.* **41**, 8784-8791, doi:10.1002/2014GL062079.

Aki, K. (1967). Scaling law of seismic spectrum, *J. Geophys. Res.* **72(4)**, 1217-1231, doi:10.1029/JZ072i004p01217.

Aki, K., and B. Chouet (1975). Origin of coda waves: Source, attenuation, and scattering effects, *J. Geophys. Res.* **80**, no. 23, 3322-3342.

Allmann, B. P., and P. M. Shearer (2009). Global variations of stress drop for moderate to

large earthquakes, *J. Geophys. Res.* **114**, B01310, doi:10.1029/2008JB005821.

Atkinson, G. M. and D. M. Boore (2006). Earthquake ground motion prediction equations for eastern North America, *Bull. Seismol. Soc. Am.* **96**, 2181-2205.

Baltay, A., S. Ide, G. Prieto, and G. Beroza (2011). Variability in earthquake stress drop and apparent stress, *Geophys. Res. Lett.* **38**, L06303, doi: 10.1029/2011GL046698.

Beyreuther, M., Barsch, R., Krischer, L., Megies, T., Behr, Y., and J. Wassermann (2010). ObsPy: A Python toolbox for seismology, *Seismol. Res. Lett.* **81**, 530-533.

Boatwright, J. (1980). A spectral theory for circular seismic sources: simple estimates of source duration, dynamic stress drop, and radiated energy, *Bull. Seismol. Soc. Am.* **70**, 1-28.

Boatwright, J., and L. Seekins (2011). Regional spectral analysis of three moderate earthquakes in northeastern North America, *Bull. Seismol. Soc. Am.* **101**, 1769-1782.

Boore, D. M. (1983). Stochastic simulation of high-frequency ground motions based on seismological models of the radiated spectra, *Bull. Seismol. Soc. Am.* **73**, 1865-1894.

Boyd, O. S., D. E. McNamara, S. Hartzell, and G. Choy (2017). Comparison of earthquake stress drops in North America, *Bull. Seis. Soc. Am.* **107**, no.2, doi: 10.1785/0120160219

Brune, J. (1970). Tectonic stress and the spectra of seismic shear waves from earthquakes, *J. Geophys. Res.* **75(26)**, 4997-5009.

Brune, J. N. (1971). Correction, *J. Geophys. Res.* **76**, 5002.

Chapman, M. C. (2013). On the rupture process of the 23 August 2011 Virginia earthquake, *Bull. Seismol. Soc. Am.* **103**, 613-628.

Chapman, M. C. (2015). Magnitude, recurrence interval, and near-source ground-motion modeling of the Mineral, Virginia, earthquake of 23 August 2011, in *The 2011 Mineral, Virginia, Earthquake and its Significance for Seismic Hazards in Eastern North America*, Horton, J.W., Jr., Chapman, M.C., and Green, R.A., (Editors), Geological Society of America Special Paper 509, doi:10.1130/2015.2509(02), 27-46.

Chapman, M.C., Qimin Wu, J.N. Beale and A.C. Hardy (2017). Mineral, Virginia, 2011 and Charleston, South Carolina, 1886: Similar aftershock sequences and the dominant role of Coulomb stress transfer, *Seism. Res. Lett.* **88**, p. 244.

Davenport, K. K., J. A. Hole, D. A. Quiros, L. D. Brown, M. C. Chapman, L. Han, and W. D. Mooney (2015). Aftershock imaging using a dense seismometer array (AIDA) after the 2011 Mineral, Virginia earthquake, in *The 2011 Mineral, Virginia, Earthquake and its Significance for Seismic Hazards in Eastern North America*, Horton, J.W., Jr., Chapman, M.C., and Green, R.A., (Editors), Geological Society of America Special Paper 509, doi:10.1130/2015.2509(15), 273-283.

Dysart, P.S., J.A. Snoke and I.S. Sacks (1988). Source parameters and scaling relations for small earthquakes in the Matsushiro region, southwest Honshu, Japan, *Bull Seismol. Soc. Am.* **78**, 571-589

Ellsworth, W.L., K. Imanishi, J.H. Luetgert and T.L. Pratt (2012). The Mw 5.8 Virginia earthquake of 23 August, 2011: A high stress drop event in a critically stressed crust, *Seismol. Res. Lett.* **83**, 212-213.

Eshelby, J. D. (1957). The determination of the elastic field of an ellipsoidal inclusion and related problems, *Proc. Roy. Soc. Lond.* **241**, 376-396, doi:10.1785/0120020217.

Frankel, A. (2015). Decay of S-wave amplitudes with distance from earthquakes in the Charlevoix, Quebec area: Effects of radiation pattern and directivity, *Bull Seismol. Soc. Am.* **105**, 850-857.

Garcia-Aristizabal, A., M. Caciagli, and J. Selva (2016). Considering uncertainties in the determination of earthquake source parameters from seismic spectra, *Geophys. J. Int.* **207**, 691-701.

Godano, M., P. Bernard, and P. Dublanchet (2015). Bayesian inversion of seismic spectral ratio for source scaling: Application to a persistent multiplet in the western Corinth rift, *J. Geophys. Res.* **120**, 7683-7712, doi:10.1002/2015JB012217.

Gutenberg, R., and C. F. Richter (1944). Frequency of earthquakes in California, *Bull. Seismol. Soc. Am.* **34**, 185-188.

Hanks, T., and H. Kanamori (1979). A moment magnitude scale, *J. Geophys. Res.* **84(B5)**, 2348-2350.

Hanks, T., and A. Johnston (1992). Common features of the excitation and propagation of strong ground motion for North American earthquakes, *Bull. Seismol. Soc. Am.* **82**, 1-23.

Hartzell, S., C. Mendoza, and Y. Zeng (2013). Rupture model of the 2011 Virginia, earthquake from teleseismic and regional waveforms, *Geophys. Res. Lett.* **40**, 5665-5670.

Herrmann, R.B. (2011). St. Louis University Earthquake Center website: `http://www.eas.slu.edu/eqc/eqc20110823.html` (last accessed March, 2017).

Horton, J. Wright, Jr., M.W. Carter, M.C. Chapman, Q. Wu, A.K. Shah, and A.C. Witt (2017). Studying the influence of rock units and joints on shallow aftershocks of the 2011 Mineral, Virginia earthquake, *Seism. Res. Lett.* **88**, p. 250.

Hough, S. E. (1996). Observational constraints on earthquake source scaling: understanding the limits in resolution, *Tectonophysics* **261**, 83-95.

Hough, S. E. (1997). Empirical Greens function analysis: taking the next step, *J. Geophys. Res.* **102**, 5369-5380.

Hough, S. E. (2014). Shaking from injection-induced earthquakes in the central and eastern United States, *Bull. Seismol. Soc. Am.* **104**, no. 5, 2619-2626.

Hough, S. E., and D. Dreger (1995). Source parameters of the 23 April 1992 M 6.1 Joshua Tree, California, earthquake and its aftershocks; empirical Greens function analysis of GEOS and TERRAscope data, *Bull. Seismol. Soc. Am.* **85**, 1576-1590.

Huang, Y., G. C. Beroza and W. L. Ellsworth (2016).Stress drop estimates of potentially induced earthquakes in the Guy-Greenbrier sequence, *J. Geophys. Res.* **121**, 6597-6607, doi:10.1002/2016JB013067.

Hunter, J. D. (2007). Matplotlib: A 2D graphics environment, *Computing in Science & Engineering* **9(3)**, 90-95.

Ide, S., and G. C. Beroza (2001), Does apparent stress vary with earthquake size?, *Geophys. Res. Lett.* **28(17)**, 3349-3352, doi:10.1029/2001GL013106.

Ide, S., G. C. Beroza, S. G. Prejean, and W. L. Ellsworth (2003). Apparent break in earthquake scaling due to path and site effects on deep borehole recordings, *J. Geophys. Res.* **108(B5)**, 13 pp., 2271, doi:10.1029/2001JB001617.

Imanishi, K., and W. L. Ellsworth (2006). Source scaling relationships of microearthquakes at Parkfield, CA, determined using the SAFOD Pilot Hole seismic array, in *Earthquakes: Radiated Energy and the Physics of Faulting*, R. Abercrombie, A. McGarr, G. D. Toro, and H. Kanamori (Editors), American Geophysical Union, Washington, D.C., 81-90.

Madariaga, R. (1976). Dynamics of an expanding circular crack, *Bull. Seismol. Soc. Am.* **66**, 639-666.

Malagnini, L., and K. Mayeda (2008). High-stress strike-slip faults in the Apennines: An example from the 2002 San Giuliano earthquakes (southern Italy), *Geophys. Res. Lett.* **35**, L12302, doi 10.1029/2008GL034024.

Mayeda, K., L. Malagnini, and W. R.Walter (2007). A new spectral ratio method using narrow band coda envelopes: Evidence for nonself-similarity in the Hector Mine sequence, *Geophys. Res. Lett.* **34**, no. 11, 1-5.

McNamara, D. E., Benz, H. M., Herrmann, R. B., Bergman, E. A., Earle, P., Meltzer,

A., Withers, M., and M. Chapman (2014). The Mw 5.8 Mineral, Virginia, earthquake of August 2011 and aftershock sequence: constraints on earthquake source parameters and fault geometry, *Bull. Seismol. Soc. Am.* **104**, 40-54.

Motazedian D., S. Ma (2014). A review study of the source parameters of the August 2011 Mw 5.7 Virginia earthquake, *Bull. Seismol. Soc. Am.* **104**, 2611-2618.

Oth, A., D. Bindi, S. Parolai, and D. Di Giacomo (2010). Earthquake scaling characteristics and the scale-(in)dependence of seismic energy-to-moment ratio: Insights from KiK-net data in Japan, *Geophys. Res. Lett.* **37**, L19304, doi 10.1029/2010GL044572.

Prieto, G. A., R. L. Parker, and F. L. Vernon (2009). A Fortran 90 library for multitaper spectrum analysis, *Comput. Geosci.* **35**, 1701-1710.

Rautian, T. G., and V. I. Khalturin (1978). The use of coda for determination of the earthquake source spectrum, *Bull. Seismol. Soc. Am.* **68**, 923-948.

Salvatier J., T. V. Wiecki, and C. Fonnesbeck (2016). Probabilistic programming in Python using PyMC3, *PeerJ Computer Science* **2:e55** `https://doi.org/10.7717/peerj-cs.55`.

Sato, H., M. Fehler, and T. Maeda (2012). Phenomenological study of coda waves, in *Seismic Wave Propagation and Scattering in the Heterogeneous Earth*, Second Ed., Springer, Berlin/Heidelberg, Germany, 1-492, doi: 10.1007/978-3-642-23029-5_3.

Scholz, C. H. (1988). The critical slip distance for seismic faulting, *Nature* **336**, 761-763.

Scholz, C. H. (1990). *The mechanics of earthquakes and faulting*, Cambridge U. Press, New

York, 441 pp.

Scholz, C. H., C. Aviles, and S. Wesnousky (1986). Scaling differences between large interplate and intraplate earthquakes, *Bull. Seismol. Soc. Am.* **76**, 65-70.

Shi, J., W. Y. Kim, and P. Richards (1998). The corner frequency and stress drops of intraplate earthquakes in the northeastern United States, *Bull. Seismol. Soc. Am.* **88**, 531-542.

Somei, K., K. Asano, T. Iwata, and K. Miyakoshi (2014). Source scaling of inland crustal earthquake sequences in Japan using the S-wave coda spectral ratio method, *Pure Appl. Geophys.* **171**, no. 10, 2747-2766.

Utsu, T., Y. Ogata, and R. S. Matsuura (1995). The centenary of the Omori formula for a decay law of aftershock activity, *J. Phys. Earth* **43**, 1-33.

Viegas, G., R. Abercrombie, and W. Y. Kim (2010). The 2002M 5 Au Sable Forks, NY, earthquake sequence: Source scaling relationships and energy budget, *J. Geophys. Res.* **115**, no. B0, 7310, doi: 10.1029/2009JB006799.

Viegas, G. (2012). Source parameters of the 16 July 2010 Mw 3.4 Germantown, Maryland, earthquake, *Seismol. Res. Lett.* **83**, no. 5, doi: 10.1785/0220110056.

Wells, D., J. A. Egan, D. G. Murphy and T. P. Paret (2015). Ground shaking and structural response of the Washington Monument during the 2011 Mineral, Virginia, earthquake, in *The 2011 Mineral, Virginia, Earthquake and its Significance for Seismic Hazards in Eastern North America*, Horton, J.W., Jr., Chapman, M.C., and Green, R.A., (Editors), Geological

Society of America Special Paper 509, doi:10.1130/2015.2509(12), 199-234.

Wessel, P., W. H. F. Smith, R. Scharroo, J. F. Luis, and F. Wobbe (2013). Generic Mapping Tools: Improved version released, *Eos Trans. AGU* **94**, 409-410.

Wu, Q., M. C. Chapman, and J. N. Beale (2015). The aftershock sequence of the 2011 Mineral, Virginia, earthquake: temporal and spatial distribution, focal mechanisms, regional stress, and the role of Coulomb stress transfer, *Bull. Seismol. Soc. Am.* **105**, 2521-2537.

Wu, Q., M. C. Chapman, J. N. Beale and S. Shamsalsadati (2016). Near-source geometrical spreading in the central Virginia seismic zone determined from the aftershocks of the 2011 Mineral, Virginia, earthquake, *Bull. Seismol. Soc. Am.* **106**, 943-955.

Yoo, S.-H., J. Rhie, H.-S. Choi, and K. Mayeda (2010). Evidence for non-self-similarity and transitional increment of scaled energy in the 2005 west off Fukuoka seismic sequence, *J. Geophys. Res.* **115**, no. B08308, doi 10.1029/2009JB007169

Chapter 5

Stress Drop Variations of Induced Earthquakes in Oklahoma †

†**Note:** A revised version of this chapter will be submitted for publication as : **Wu, Q.,** and M. C. Chapman (2017). Stress Drop Variations of Induced Earthquakes in Oklahoma, *Bull. Seismol. Soc. Am.* (**to be submitted**).

5.1 Abstract

We calculate corner frequencies and stress drops for 201 earthquakes in four earthquake sequences that are potentially induced by waste-water injection in Oklahoma. Specifically, we determined stress drops for 35 events in the 2011 Mw 5.6 Prague sequence, 40 events in the 2016 Mw 5.1 Fairview sequence, 73 events in the 2016 Mw 5.8 Pawnee sequence, and 53 events in the 2016 Mw 5.0 Cushing sequence. Although the stress drop estimates show large scatter for each sequence, with one important exception, we found high stress drops for 3 of the 4 Mw 5+ mainshocks (20-30 MPa) and lower stress drops for aftershocks in each individual sequences. The exception is the 2011 Prague sequence, which has stress drops ranging between 0.02 and 228 MPa and the mainshock has a low stress drop of 2.8 MPa. Compared to the other three sequences, the 2016 Fairview sequence exhibits more constant stress drop estimates, with a 2-3 times higher median stress drop. We observed that in all cases, the earthquakes with high and low stress drops appear to occur in separate, distinct clusters spatially. This may reflect strong fault heterogeneity, which in the case of induced earthquakes may be influenced by the injection of fluids into the subsurface. Alternatively, low stress drop events may be those aftershocks that re-ruptured the mainshock slip patches that have not completely healed. Future examination of the spatial correlation between the stress drops and mainshock rupture slip patches and/or injection well data may help explain this observation.

5.2 Introduction

The seismicity rate in the central United States (CUS) has dramatically increased since 2009 and has been linked to waste-water disposal in unconventional oil and gas recovery (Ellsworth, 2013). In Oklahoma, the link between waste-water injection and seismicity is well documented (Keranen et al., 2014; Walsh and Zoback, 2015) and includes many notable earthquake sequences (McNamara et al., 2015; Yeck et al., 2016). For example, the 2011 M_W 5.6 Prague earthquake, one of the largest historical earthquakes in Oklahoma, resulted in structural damage and was attributed to nearby waste-water disposal (Keranen et al., 2013; Sumy et al., 2014; McNamara et al., 2015). The February 2016 M_W 5.1 Fairview sequence, consisting of several $M_W \geq 4$ foreshocks and aftershocks, was interpreted to have been induced by clustered, high-rate injection wells 12-20 km from the sequence through far-field pressurization (Yeck et al., 2016).

However, it remains difficult to determine conclusively whether a given earthquake is linked to waste-water injection, because fluid does not seem to be the sole or even a necessary requirement for inducing earthquakes (Kim , 2013; Gobel, 2015). Dahm et al. (2013) suggested three approaches to discriminate between induced and natural earthquakes: a physics-based probabilistic model, a statistics-based seismicity model, and a source-parameter approach. Evidences such as proximity to injection wells, correlation between production/injection activities and seismicity are also used for evaluating the likelihood of earthquakes being induced (Davis and Frohlich, 1993; Frohlich et al., 2016). Zhang et al. (2016) calculated full moment tensor solutions for induced earthquakes in the Western Canadian Sedimentary Basin and found that most induced events exhibit significant non-double-couple components. Some

previous studies suggest that source parameters, such as stress drops, may provide more direct evidence of induced earthquakes (Goertz-Allman et al., 2011; Chen and Shearer, 2011; 2012; Sumy et al., 2017).

Hough (2014) observed low felt intensities for potentially induced earthquakes in the central and eastern United States (CEUS) and interpreted them to be a result of low stress drops compared to tectonic earthquakes. Studies of induced events in geothermal fields show that stress drops are lowest near the injection wells and increase with distance from the wells (Goertz-Allman et al., 2011; Chen and Shearer, 2011; 2012). Boyd et al. (2017) found that potentially induced earthquakes in the CUS have stress drops that are a factor of 2 lower than earthquakes in the western US and a factor of 6 lower than earthquakes in the eastern US. Sumy et al. (2017) obtained a median stress drop (Brune stress drop) of 0.2 MPa for 87 aftershocks in the 2011 Prague sequence, which is significantly lower than that of typical eastern United States tectonic earthquakes. However, Huang et al. (2016, 2017) found that the value of range of stress drops of potentially induced earthquakes are comparable to tectonic earthquakes in the CEUS. Clerc et al. (2016) studied a sequence of induced earthquakes near Crooked Lake, Alberta and observed that the stress drops of those events fall within the high side of the typical reported range of tectonic earthquakes. Zhang et al. (2016) also obtained stress drops that fall within typical range for tectonic earthquakes by studying eight induced earthquakes in the Western Canadian Sedimentary Basin.

Stress drop estimates rely on accurate measurement of corner frequencies for small-to-moderate size earthquakes. This requires the effective removal of path and site effects to obtain the source spectrum of earthquakes. Imperfect separation of path and site effects,

particularly for small earthquakes, may lead to large uncertainties in corner frequency measurements and therefore results in large uncertainties in stress drop estimates. Among the various ways to measure corner frequencies, the empirical Greens function (EGF) method or the spectral ratio method is preferred because it effectively removes the propagation and site effects for co-located earthquakes with similar focal mechanism (e.g., Hough, 1997; Abercrombie, 2015; Huang et al., 2016). Imanishi and Ellsworth (2006) proposed a multi-window spectral ratio method to obtain stable spectral ratios by stacking spectral ratios measured from moving windows following the direct arrivals. Mayeda et al. (2007) and Somei et al. (2014) showed that the use of S-wave coda considerably reduces the scatter of spectral ratios compared to the use of direct S-waves. Wu et al. (2017) extended the multi-window spectral ratio method on S-wave coda and obtained stable spectral ratios for the 2011 Mineral, Virginia mainshock and aftershocks.

In this study, we follow the multi-window coda spectral ratio method of Wu et al. (2017) to estimate corner frequencies and stress drops for four earthquake sequences occurred in Oklahoma since 2011, including the 2011 M_W 5.6 Prague sequence, the 2016 M_W 5.1 Fairview sequence, the 2016 M_W 5.8 Pawnee sequence, and the 2016 M_W 5.0 Cushing sequence. In the following sections, we first briefly describe dataset we used and the multi-window coda spectral ratio method, and then present the results obtained for each individual earthquake sequence. We discuss the stress drop variations by examining the possible dependence of stress drops on earthquake size and focal depth, as well as temporal and spatial distributions of stress drop estimates.

5.3 Dataset

The earthquake catalogs used in this study involves published earthquake relocations for the 2011 Prague sequence (Sumy et al., 2014) and the 2016 Farview sequence (Chen et al., 2016), and the USGS catalogs for the 2016 Pawnee sequence and the 2016 Cushing sequence. All the earthquake sequences were well recorded by permanent and temporary networks. We use waveform data from all broadband stations within 200 km of the mainshocks of individual sequences (Fig 5.1). Those stations were sampled at 40, 100 or 200 sample/s, providing broad enough bandwidth to measure the corner frequency of most events. The pre-processing steps involve retrieving waveform data from the Incorporated Research Institutions for Seismology (IRIS) Data Management Center, instrument response correction to velocity records, rotation to radial, transverse, and vertical components followed by mean and trend removal of seismograms. Those potentially induced earthquakes are shallow, with most of them occurred at depths less than 10 km. Seismic moment (or moment magnitude M_W) is also a crucial parameter in calculating stress drops. While the moment magnitude of moderate-size earthquakes are usually well-contrained by moment tensor inversion techniques, slight discrepancies still exist among values reported by different groups. These slight discrepancies in M_W give rise to considerably large differences in stress drop calculation. With this consideration, we use seismic moment estimates of relatively large events ($M_W \geq 4.0$) from Herrmann (2017), which were determined consistently using regional moment tensor inversion. Seismic moments of smaller events are estimated from the spectral ratio analysis at low frequencies as described in a later section.

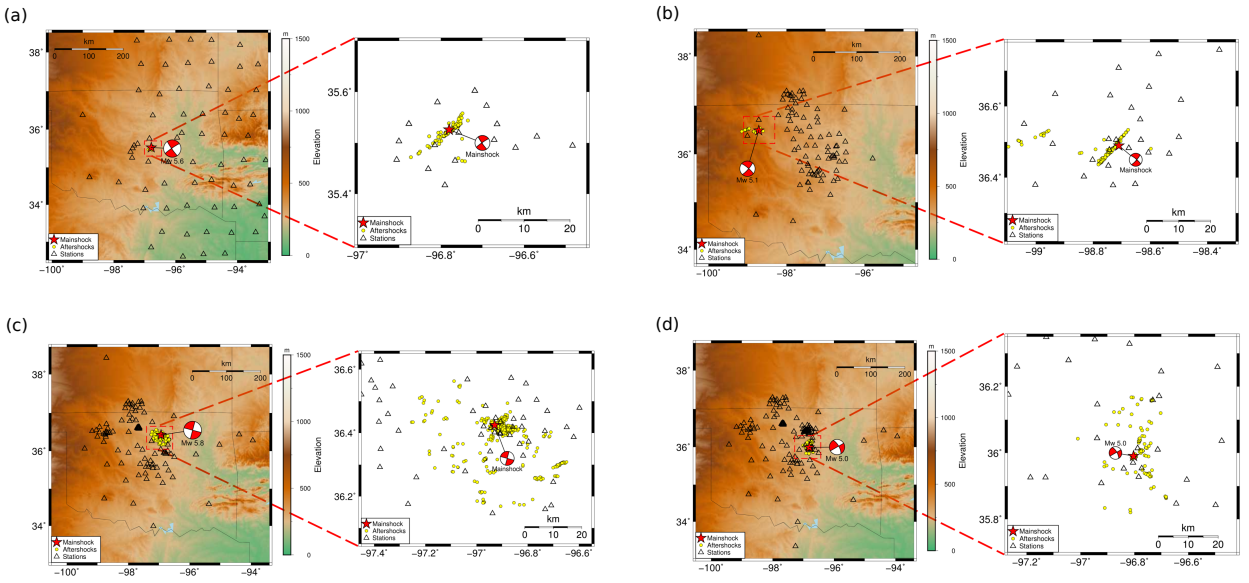

Figure 5.1: Earthquake epicenters and stations used in this study. (a) The 2011 M_W 5.6 Prague, Oklahoma earthquake sequence; (b) The 2016 M_W 5.1 Fairview, Oklahoma earthquake sequence; (c) The 2016 M_W 5.8 Pawnee, Oklahoma earthquake sequence; (d) The 2016 M_W 5.0 Cushing, Oklahoma earthquake sequence;

5.4 Multi-window Coda Spectral Ratio Method

We follow the multi-window coda spectral ratio proposed by Wu et al. (2017) to measure corner frequencies accurately. Compared to direct S-waves, coda waves are less sensitive to source radiation pattern and rupture complexities such as directivity effects due to the fact that the coda, being made up of scattered S-waves, homogenizes the source energy spatially (Mayeda et al., 2007; Sato et al., 2012; Somei et al., 2014; Wu et al., 2017). Starting at lapse time greater than twice S-wave traveltime, the decay rate of coda amplitude becomes stationary (Aki and Chouet, 1975; Frankel, 2015; Wu et al., 2016). As follows, we briefly describe the method and the data processing steps with one event pair (the M_W 5.1 mainshock and a M_W 3.8 foreshock) taken from the 2016 Fairview earthquake sequence (Fig.

5.2).

We select event pairs that occurred close to each other, with a maximum spatial separation of 5 km and a maximum depth difference of 2 km. The minimum magnitude difference of event pairs is set at 0.6. The entire coda window length is determined to be 30 s and 20 s for event pairs with the master event magnitude $M_W \geq 4.0$ and $M_W < 4.0$ respectively, considering the stability of coda and good enough signal-to-noise ratio (SNR). A minimum SNR of 3 is required for all events considered. The long coda window is then divided into 5 successive sub-windows to make the spectral ratio measurements stable by a stacking procedure. The common decay characteristics of coda of event pairs is examined to ensure similar propagation and site effects for event pairs. We calculate narrow-band coda envelopes in four frequency bands: 1-2 Hz, 2-4 Hz, 4-8 Hz, and 8-16 Hz. The narrow-band envelopes are then smoothed by applying a 10-second moving average operator (Fig. 5.2). In the determined coda window, we calculate the envelope amplitude ratios for the event pair (master event and EGF event) and normalize the ratios by the average value of the entire window. Common decay rate of coda envelope gives normalized envelope amplitude ratios of 1 over the entire coda analysis window. We restrict qualified event pairs with mean and standard deviation of the normalized envelope ratios in the coda window to be 1.0 ± 0.1 and 0.05, respectively, for all evaluated frequency bands.

For selected event pairs with very similar coda decay characteristics, we calculate the spectral ratios of the multiple coda windows on three-component velocity seismograms. The spectra of coda windows and the pre-P noise window are calculated using a multi-taper algorithm (Prieto et al., 2009). The final coda spectral ratio is obtained by stacking the ratios from

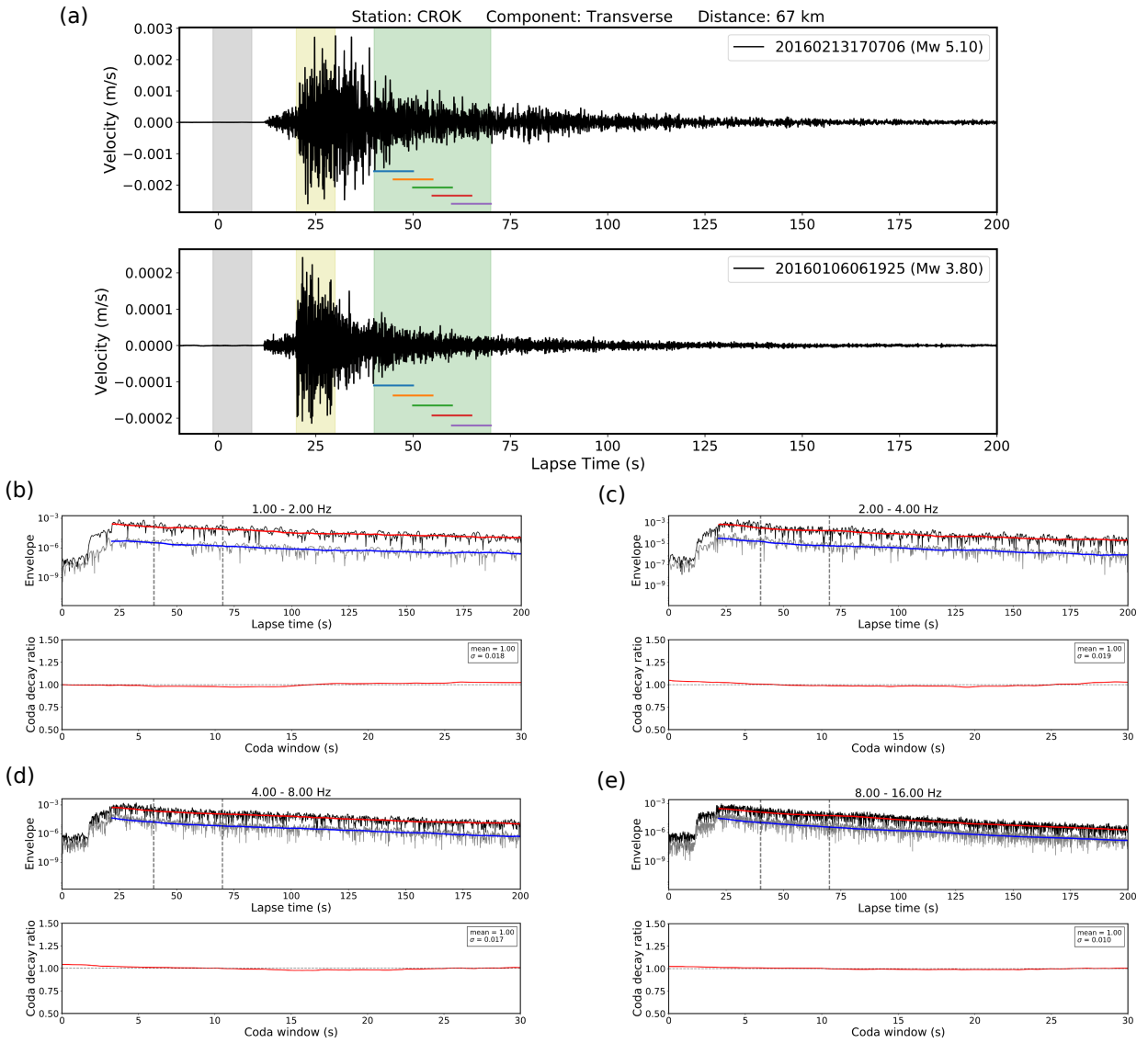

Figure 5.2: The M_W 5.1 Fairview mainshock and an M_W 3.8 foreshock recorded at station CROK at an epicentral distance of 67 km. (a). The transverse-component velocity records of the two events. The shaded areas from left to right denote the pre-signal noise window, the direct S-wave window, and the whole coda window. The short horizontal bars below the seismograms within the coda window mark the placement of 5 sub-divided short coda windows; (b)-(e). Comparison of the coda decay characteristics for the large and small events in four frequency bands: 1-2 Hz (b); 2-4 Hz (c); 4-8 Hz (d) and 8-16 Hz (e). In (b)-(e), the top panels show the narrow-band original and smoothed envelopes. The vertical dashed lines indicate the coda window. The bottom panels show the normalized coda decay ratio for the coda window (see text for details). The mean value and standard deviation of coda decay ratios are shown at the upper-right corner of the bottom panels.

multiple sub-windows in the logarithmic space. We then resample the stacked spectral ratios to 100 points between 0.1 and 100 Hz equally in the logarithmic scale to ensure equal weights over the entire frequency bands in the source model fitting procedure. The maximum usable frequency is set at 80% of the Nyquist frequency to ensure reliable resolution of corner frequencies. The spectral ratios calculated from different stations are finally stacked to generate the spectral ratio of a given event pair. As a reference, the spectral ratios of direct S-waves are also calculated (Fig. 5.2). While the stacked spectral ratios are similar with direct S-waves and coda, the multi-window coda spectral ratios exhibit much lower inter-station scatter (Fig. 5.3). We visually inspected the calculated spectral ratios and only accepted those showing a clear low-frequency plateau and high-frequency asymptote as predicted by the omega-square source model (e.g., Brune model).

Assuming the Brune source spectral model (Brune, 1970, 1971), we fit the stacked multi-window coda spectral ratios to obtain the two corner frequencies (f_{c1} for the master event, and f_{c2} for the EGF event) and the seismic moment ratio of the two events with equation (4.3) presented in Chapter 4.

To obtain best parameters and particularly the associated uncertainties that fit the Brune model, we apply a Markov chain Monte Carlo (MCMC) algorithm in the Bayesian framework (Salvatier et al., 2016) to model the spectral ratios to determine the two corner frequencies f_{c1}, f_{c2} and the M_{ratio} simultaneously. We assume a log-normal distribution of the prior probability for the model parameters (f_{c1}, f_{c2} and M_{ratio}), and a normal distribution for the likelihood function following Godano et al. (2015) and Garcia-Aristizabal et al. (2016). The best estimates and uncertainties are drawn from the posterior distributions (Fig. 5.3c).

Figure 5.3b shows the best-fitting Brune source model with best estimates of f_{c1}, f_{c2} and M_{ratio} and their 95% confidence intervals. Figure 5.3c shows the posterior distributions of model parameters from which the confidence intervals are determined. The best estimates of seismic moment ratios (M_{ratio}) are used to calibrate M_W for small events assuming M_W for larger events ($M_W \geq 4.0$) are well constrained by regional moment tensor inversion (Herrmann, 2017).

5.5 Stress Drop Estimates

For most of the large events (Mw 4 and above), we are able to find multiple EGF events to form event pairs. In such cases, we calculate the weighted mean (in the logarithmic space) of the corner frequencies from individual estimates, in which the weights are the inverse of corresponding errors (Abercrombie, 2014). For the four mainshocks, 3, 10, 11, 21 EGF events are found to produce very consistent corner frequency estimates (Fig. 5.4).

We calculate the Brune stress drop from calibrated seismic moment M0 and measured corner frequency fc , assuming a simple circular crack model (Eshelby, 1957; Brune, 1970, 1971) with equation (4.4) presented in Chapter 4.

5.5.1 The 2011 M_W 5.6 Prague sequence

In November 2011, three M_W 4.8 and greater earthquakes occurred near Prague, Oklahoma with 3 days. Keranen et al. (2013) and Sumy et al. (2014) suggest that the first M_W 4.8 earthquake was induced and set off successive failure along the fault system, including the

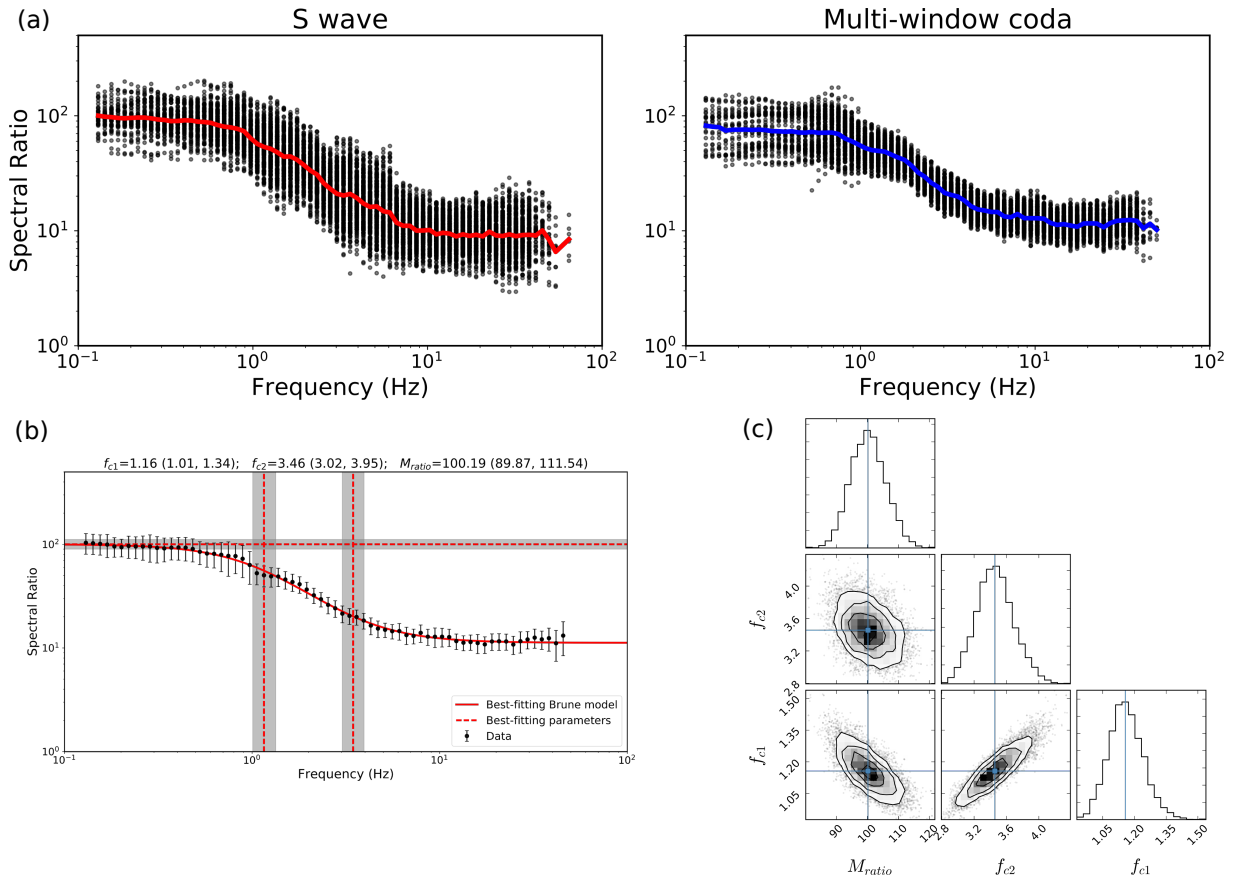

Figure 5.3: The spectral ratios and corner frequency estimates of the mainshock-aftershock pair shown in Figure 5.2. (a).*S*-wave spectral ratios (upper left) and multi-window coda spectral ratios (upper right) measured at all stations. Note the similar stacked spectral ratios for *S*-wave and coda and much reduced inter-station variation for coda above 1 Hz. (b).Bayesian model fitting. The dashed lines show the best-fitting model parameters (f_{c1}, f_{c2}, M_{ratio}). The shaded areas show the 95% confidence intervals of the estimated parameters. The values are shown above the figure. (c).The posterior distributions of the model parameters. The diagonal panels display the posterior probability density function (PDF) of M_{ratio} (top), f_{c2} (middle), and f_{c1} (bottom). The off-diagonal panels show the two-dimensional projections of the posterior samples (gray dots) of the Markov chain Monte Carlo simulations, in which the contours represent 0.5, 1, 1.5, and 2 standard deviations.

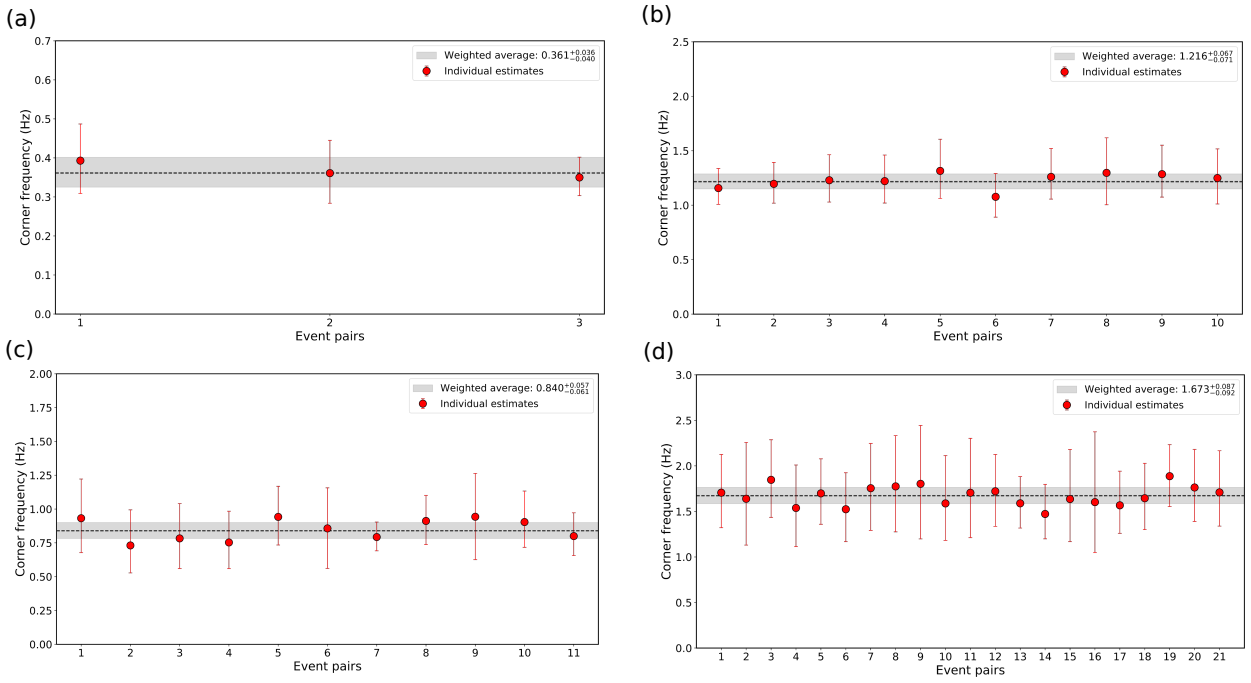

Figure 5.4: Estimates of the mainshock corner frequencies from multiple different EGF events. The filled circles with error-bars denote best-estimates with 95% confidence intervals. The horizontal dashed line represents the weighted-average corner frequency. The shaded area shows the weighted uncertainty estimate. (a).The M_W 5.6 Prague mainshock; (b).The M_W 5.1 Fairview mainshock; (c).The M_W 5.8 Pawnee mainshock; (d).The M_W 5.0 Cushing mainshock

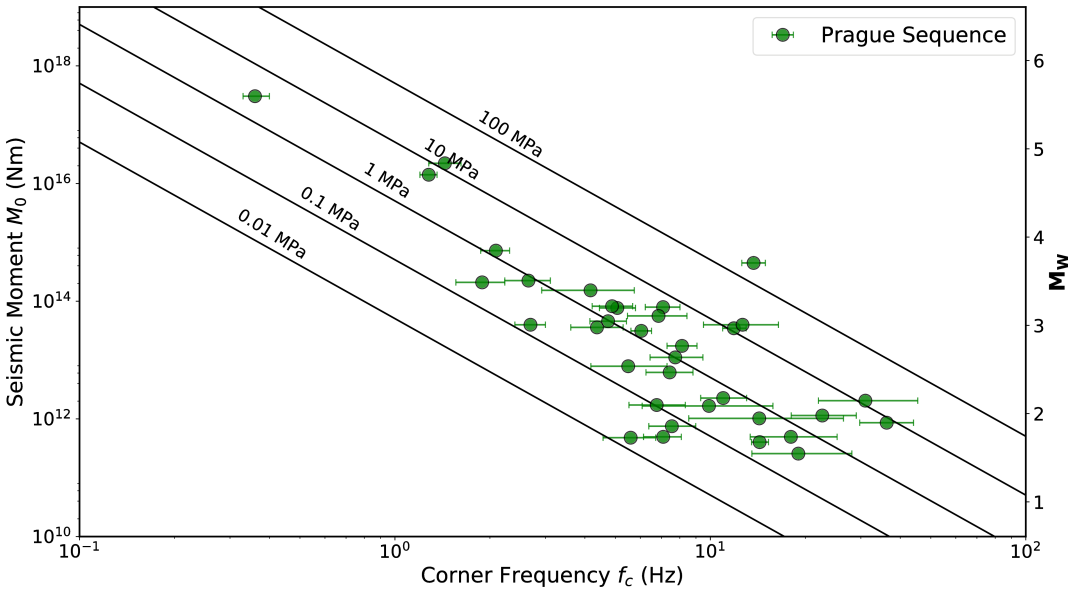

Figure 5.5: Seismic moment versus corner frequency for the Prague sequence. The solid diagonal lines mark lines of constant stress drops of 0.01, 0.1, 1, 10, and 100 MPa. The filled circles show best-estimate corner frequencies with 95% confidence intervals indicated by the error-bars.

M_W 5.6 mainshock and the largest M_W 4.8 aftershock. Sun and Hartzell (2014) determined a finite-fault slip model for the mainshock, and found that the average Brune stress drop for the largest slip patch near the mainshock hypocenter was 9 MPa and the stress drop averaged over all areas of slip was 1.6 MPa. Sumy et al. (2017) obtained stress drops for 87 aftershocks with M_W 1.83-3.51 by fitting individual spectra with a H/V correction for site effects. They found a range of stress drops between 0.005 and 4.8 MPa with a median value of 0.2 MPa, which is significantly lower than typical CEUS tectonic earthquake (~10 MPa).

In this study, we calculated stress drops for 35 events (M_W 1.54-5.6) in the Prague sequence including the M_W 5.6 mainshock and the two M_W 4.8 events. We obtained a wide range of stress drop estimates between 0.02 and 228.12 MPa, with a median value of 1.02 MPa (Fig. 5.5 and 5.6). Stress drops of 5.84 MPa, 2.85 MPa and 13.15 MPa were determined for the

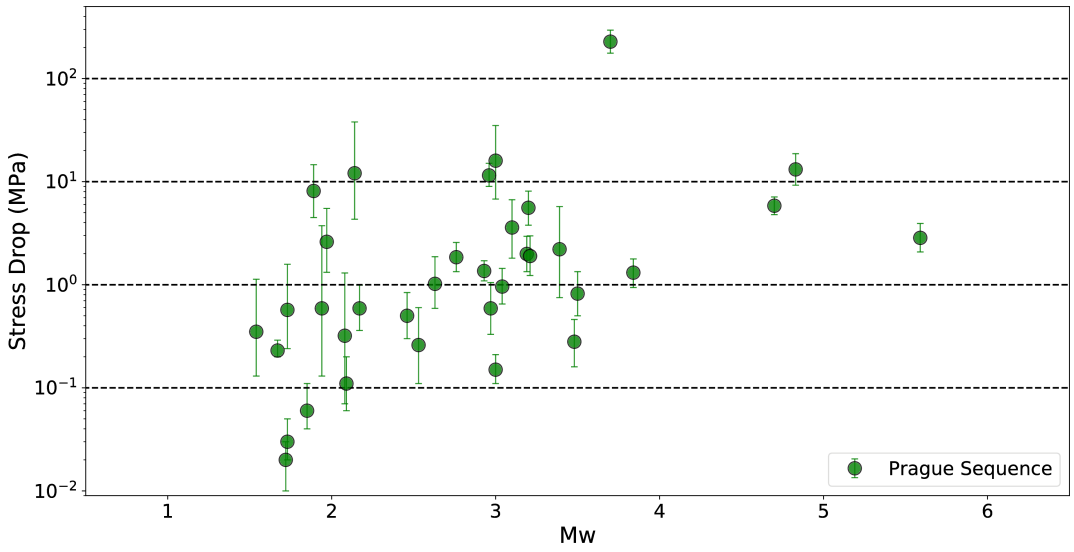

Figure 5.6: Stress drop versus moment magnitude M_W for the Prague sequence, assuming the Brune (1970,1971) model. The error-bars denote the 95% confidence interval of stress drop estimates. The median value is 1.02 MPa.

M_W 4.8 foreshock, the M_W 5.6 mainshock and the M_W 4.8 aftershock, respectively.

To investigate any spatial variation of stress drops, we examine the estimates in map view and two cross-section views (Fig. 5.7). The high and low stress drop events appear to cluster spatially, with a low stress drop cluster of events at the northeast end of the sequence. The events to the southwest exhibit generally higher stress drops. An isolated deep event has an extremely high stress drop of 228 MPa. Figure 5.6 shows no strong evidence of a dependence of stress drop on moment magnitude. We observed no clear relationships between stress drop and time or focal depth.

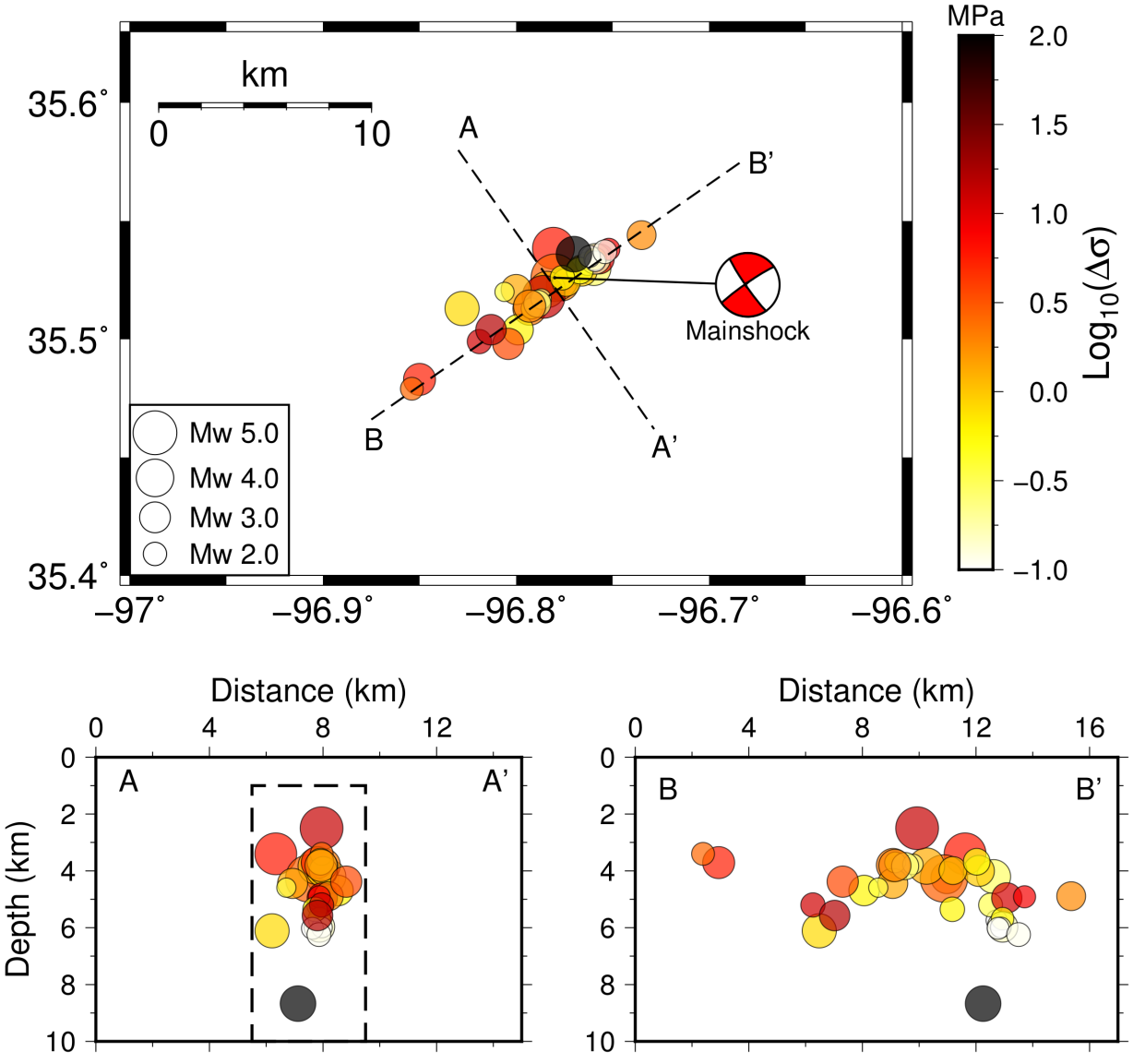

Figure 5.7: Spatial variation of stress drop estimates for the Prague sequence. (a) Mapview. The symbol sizes are proportional to the earthquake magnitudes. The two profiles (AA’ and BB’) are selected to be perpendicular and parallel, respectively, to the main aftershock cluster strike direction. (b). Cross-section view along profile A-A’. (c) Cross-section view along profile B-B’.

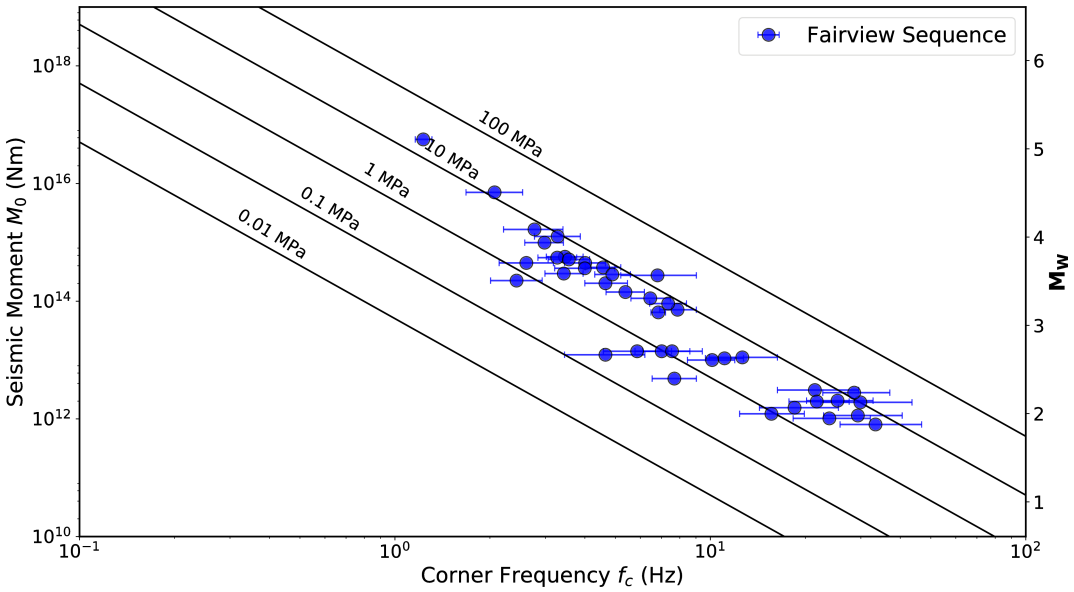

Figure 5.8: Seismic moment versus corner frequency for the Fairview sequence. The solid diagonal lines mark lines of constant stress drops of 0.01, 0.1, 1, 10, and 100 MPa. The filled circles show best-estimate corner frequencies with 95% confidence intervals indicated by the error-bars.

5.5.2 The 2016 M_W 5.1 Fairview sequence

The Fairview earthquake sequence produced five earthquakes with M_W 4.4 or larger, including the M_W 5.1 mainshock on 13 February 2016. Yeck et al. (2016) suggested far-field pressurization from a cluster of high-rate injection wells at distances greater than 12 km induced this sequence, pointing to the critical role that pre-existing faults play in the occurrence of large induced earthquakes.

We calculated stress drops for 40 events with M_W ranging from 1.87 to 5.1 in the Fairview sequence (Fig. 5.8, 5.9 and 5.10). This sequence has a much narrower range of stress drops (0.24-20.79 MPa) and ~4 times higher median stress drop (4.6 MPa) compared to the Prague sequence. The Fairview sequence shows much less variation in stress drop than the Prague

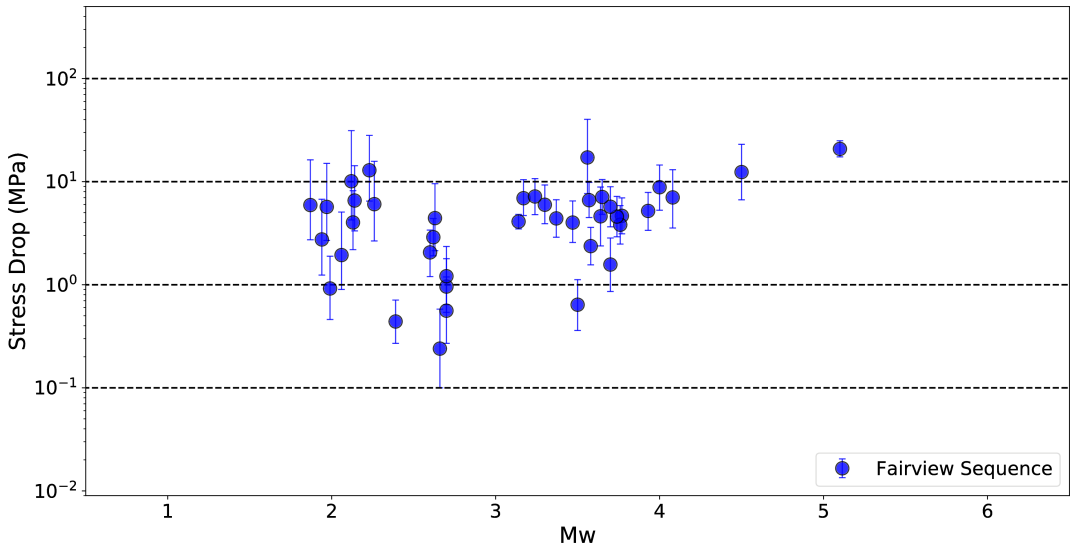

Figure 5.9: Stress drop versus moment magnitude M_W for the Fairview sequence, assuming the Brune (1970,1971) model. The error-bars denote the 95% confidence interval of stress drop estimates. The median value is 4.6 MPa.

sequence, and there appears to be no dependence of stress drop on magnitude, although the mainshock stress drop is slightly higher than some of the aftershocks. Likewise, there is no clear spatial pattern or depth dependence of stress drop in this data set. However, the events with the lowest stress drops occurred shortly after the mainshock.

5.5.3 The 2016 M_W 5.8 Pawnee sequence

The 3 September 2016 M_W 5.8 Pawnee earthquake is the largest since the increase of seismic activity in Oklahoma. The Pawnee mainshock was preceded by a M_W 3.3 foreshock two days before the mainshock. This foreshock behavior is similar to that of the Prague and Fairview sequences, but not quite as strong (Fairview and Prague both had foreshocks of M_W 4+).

The 73 stress drops that were estimated for this sequence range between 0.03 and 42.67

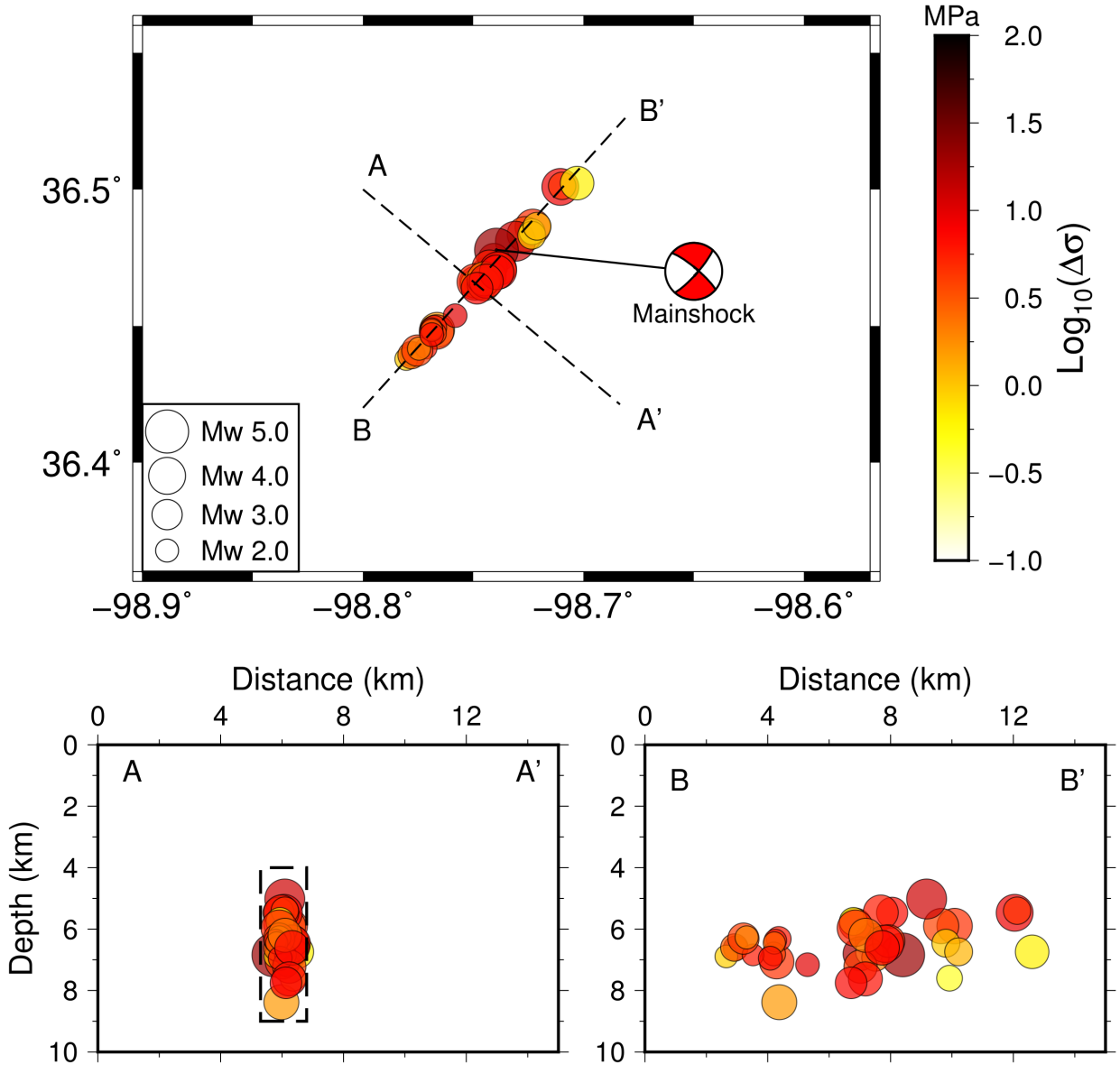

Figure 5.10: Spatial variation of stress drop estimates for the Fairview sequence. (a) Mapview. The symbol sizes are proportional to the earthquake magnitudes. The two profiles (AA' and BB') are selected to be perpendicular and parallel, respectively, to the main aftershock cluster strike direction. (b). Cross-section view along profile A-A'. (c) Cross-section view along profile B-B'.

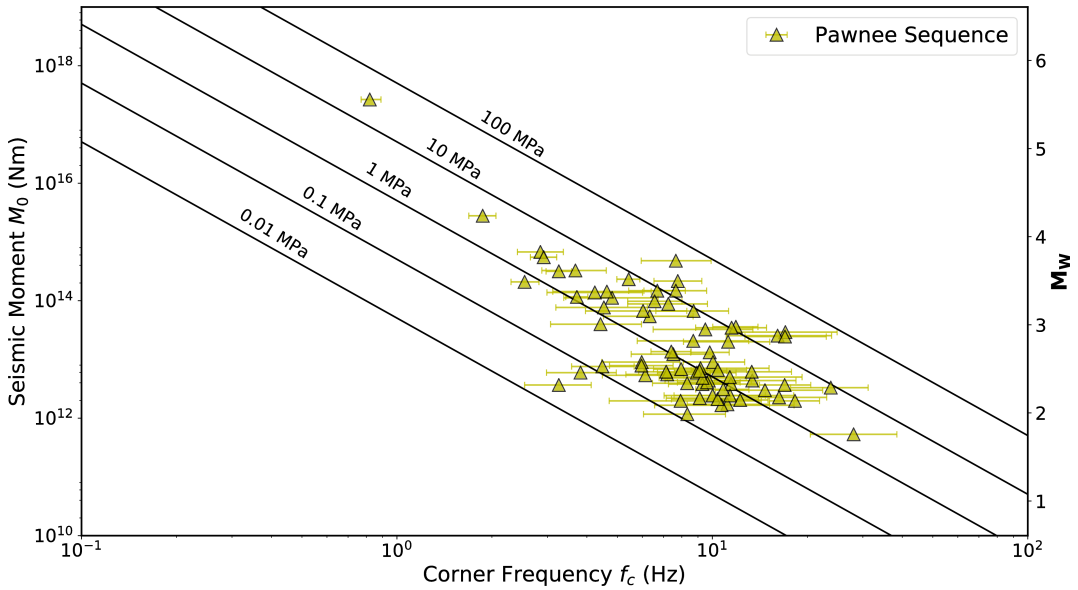

Figure 5.11: Seismic moment versus corner frequency for the Pawnee sequence. The solid diagonal lines mark lines of constant stress drops of 0.01, 0.1, 1, 10, and 100 MPa. The filled circles show best-estimate corner frequencies with 95% confidence intervals indicated by the error-bars.

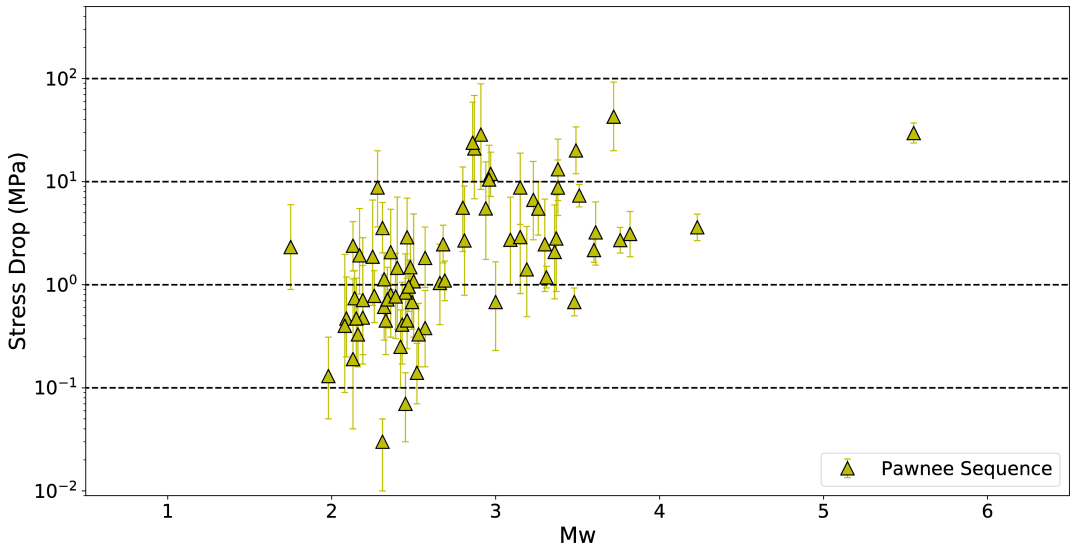

Figure 5.12: Stress drop versus moment magnitude M_W for the Pawnee sequence, assuming the Brune (1970,1971) model. The error-bars denote the 95% confidence interval of stress drop estimates.

MPa, with a median value of 1.82 MPa (Fig. 5.11 and 5.12). The Pawnee sequence is very similar to the Prague sequence in terms of the median values of the stress drop and their scatter about the median. However, the two sequences are very different in terms of the relationship of the mainshock to aftershock stress drop. The Pawnee mainshock has a very high stress drop (29.61 MPa) compared to the median stress drop of the sequence, whereas the Prague mainshock stress drop is very similar to the median stress drop. Both Pawnee and Fairview mainshocks have high stress drops compared to the median values of their respective sequences. In this attribute, Pawnee and Fairview are similar to the Mineral, Virginia sequence. It appears that in the case of the Pawnee aftershocks, like for Prague, the high and low stress drops appear to cluster in space (Fig. 5.13).

5.5.4 The 2016 M_W 5.0 Cushing sequence

We determined stress drops for 53 events since January 2016 in the vicinity of the 7 November 2016 M_W 5.0 Cushing mainshock. They range from 0.04 to 24.41 MPa with a median of 1.36 MPa (Fig. 5.14 and 5.15). The M_W 5.0 mainshock has the highest stress drop of the sequence. This sequence exhibits very similar statistics of stress drop estimates to the Pawnee sequence: similar range of stress drop variation and median stress drop, and high stress drop mainshocks. Also, as observed in the Prague and Pawnee sequences, the Cushing sequence shows spatially concentrated high and low stress drop small clusters: a group of high stress drop events to the south, another group of high stress drop events near the mainshock, and a low stress drop cluster at the north end (Fig. 5.7, 5.13 and 5.16).

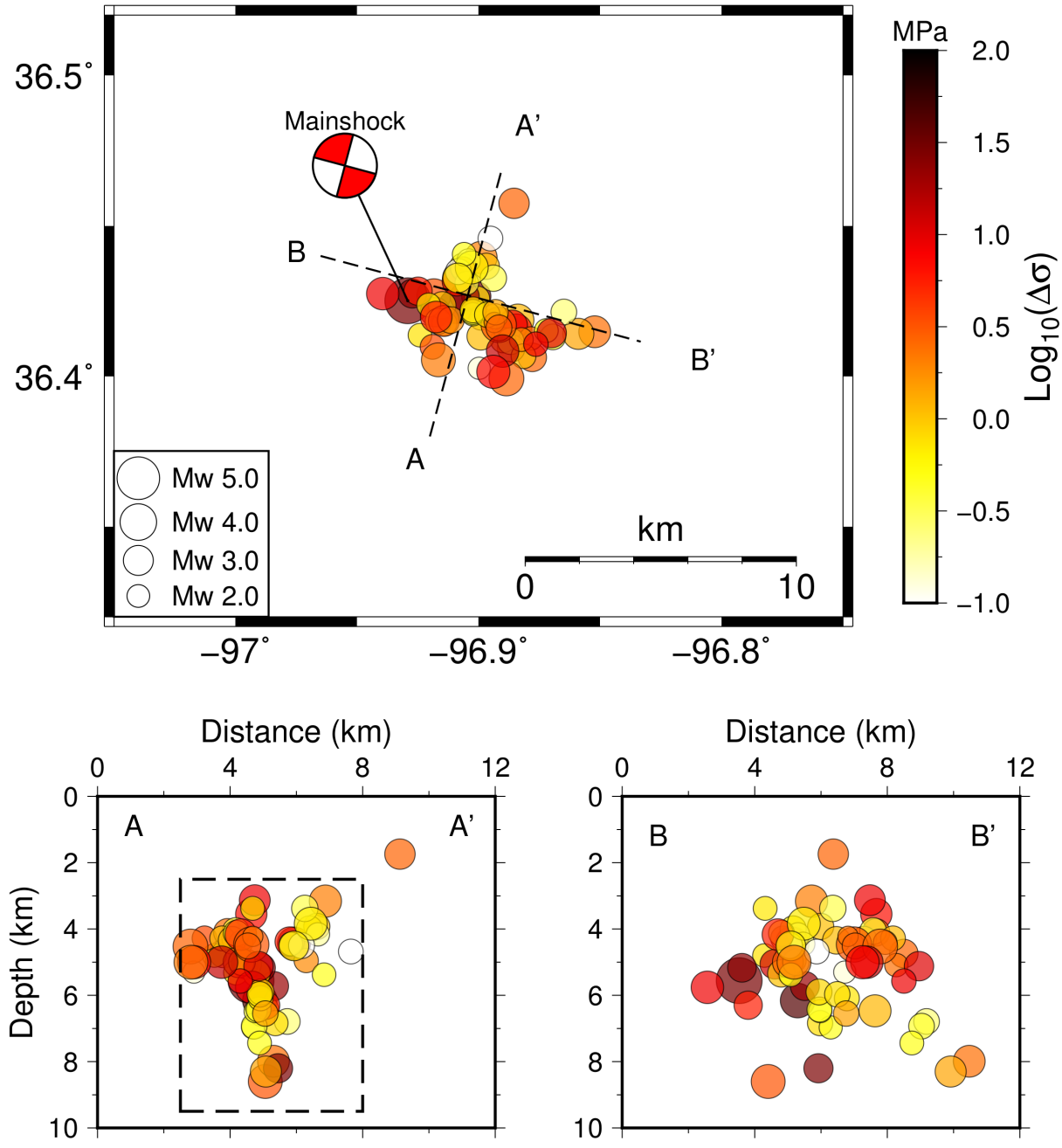

Figure 5.13: Spatial variation of stress drop estimates for the Pawnee sequence. (a) Mapview. The symbol sizes are proportional to the earthquake magnitudes. The two profiles (AA' and BB') are selected to be perpendicular and parallel, respectively, to the main aftershock cluster strike direction. (b). Cross-section view along profile A-A'. (c) Cross-section view along profile B-B'.

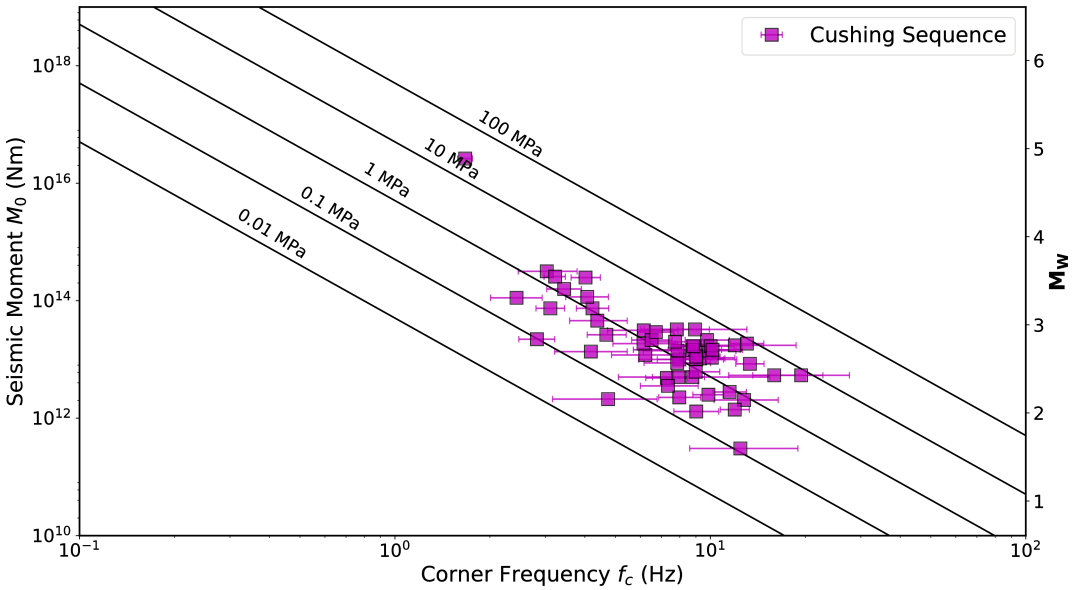

Figure 5.14: Seismic moment versus corner frequency for the Cushing sequence. The solid diagonal lines mark lines of constant stress drops of 0.01, 0.1, 1, 10, and 100 MPa. The filled circles show best-estimate corner frequencies with 95% confidence intervals indicated by the error-bars.

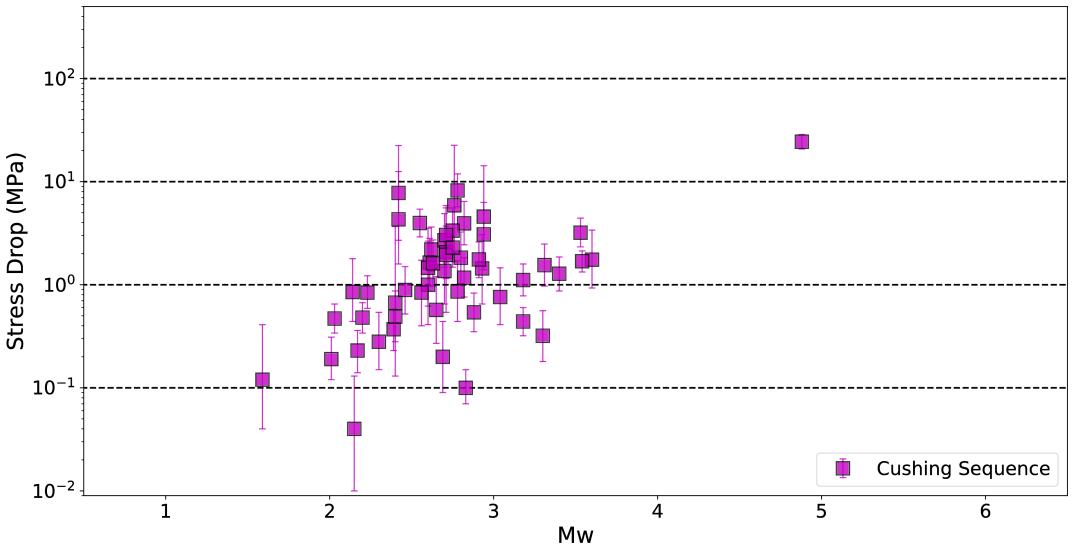

Figure 5.15: Stress drop versus moment magnitude M_W for the Cushing sequence, assuming the Brune (1970,1971) model. The error-bars denote the 95% confidence interval of stress drop estimates.

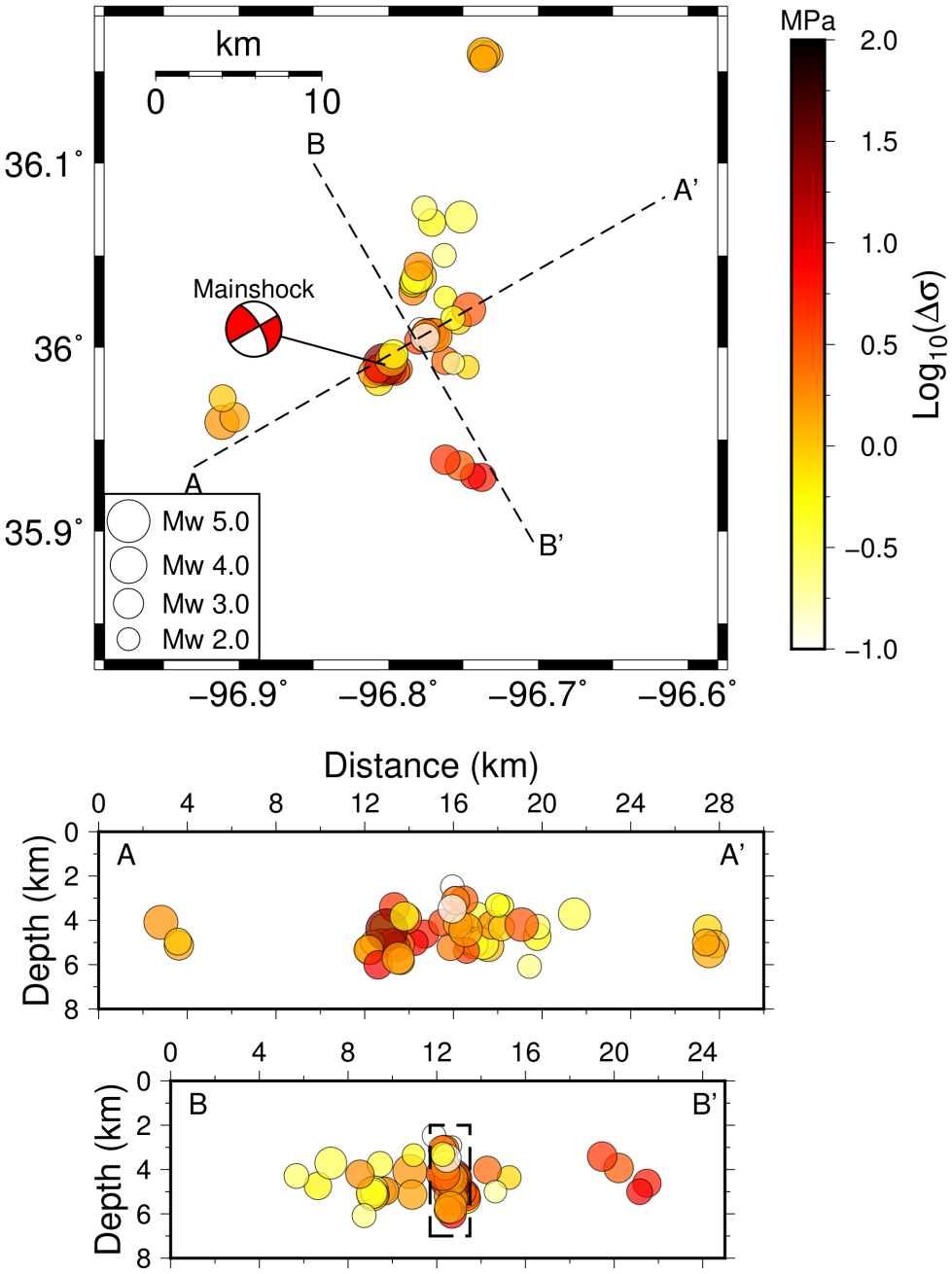

Figure 5.16: Spatial variation of stress drop estimates for the Cushing sequence. (a) Mapview. The symbol sizes are proportional to the earthquake magnitudes. The two profiles (AA' and BB') are selected to be perpendicular and parallel, respectively, to the main aftershock cluster strike direction. (b). Cross-section view along profile A-A'. (c) Cross-section view along profile B-B'.

5.6 Discussion and Conclusions

Figure 5.17 summarizes the stress drop estimates of M_W 2 and above earthquakes for the four earthquake sequences studied along with those for the 2011 M_W 5.7 Mineral, Virginia sequence determined in Wu and Chapman (2017). As the only tectonic earthquake sequence, the Mineral sequence has a significantly higher median stress drop of 13.4 MPa than those potentially induced earthquake sequences in Oklahoma. Among the four Oklahoma earthquake sequences, the Fairview sequence exhibits considerably less scatter of stress drops and a 2-3 times higher median stress drop than the other three. While the Fairview, Pawnee and Cushing mainshocks have very consistent high stress drops between 20 and 30 MPa, the Prague mainshock has a much lower stress drop of 2.85 MPa.

As shown in all sequences, it appears that high and low stress drop events concentrate in space (Fig. 5.7, 5.13 and 5.16). Spatially varying stress drops may reflect strong fault heterogeneity (Fehler and Phillips, 1991), which in the case of induced earthquakes may be influenced by the injection of fluids into the subsurface (Sumy et al., 2017). Alternatively, low stress drop events may be those aftershocks that re-ruptured the mainshock slip patches that have not completely healed (Vidale et al., 1994; Shaw et al., 2015). Future examination of the spatial correlation between the stress drops and mainshock rupture slip concentrations may help explain this observation. Also, it would be worth investigating the correlation between the stress drop variations and the parameters associated with nearby large volume injection wells.

In this study, we apply a stable multi-window coda spectral ratio method to determine

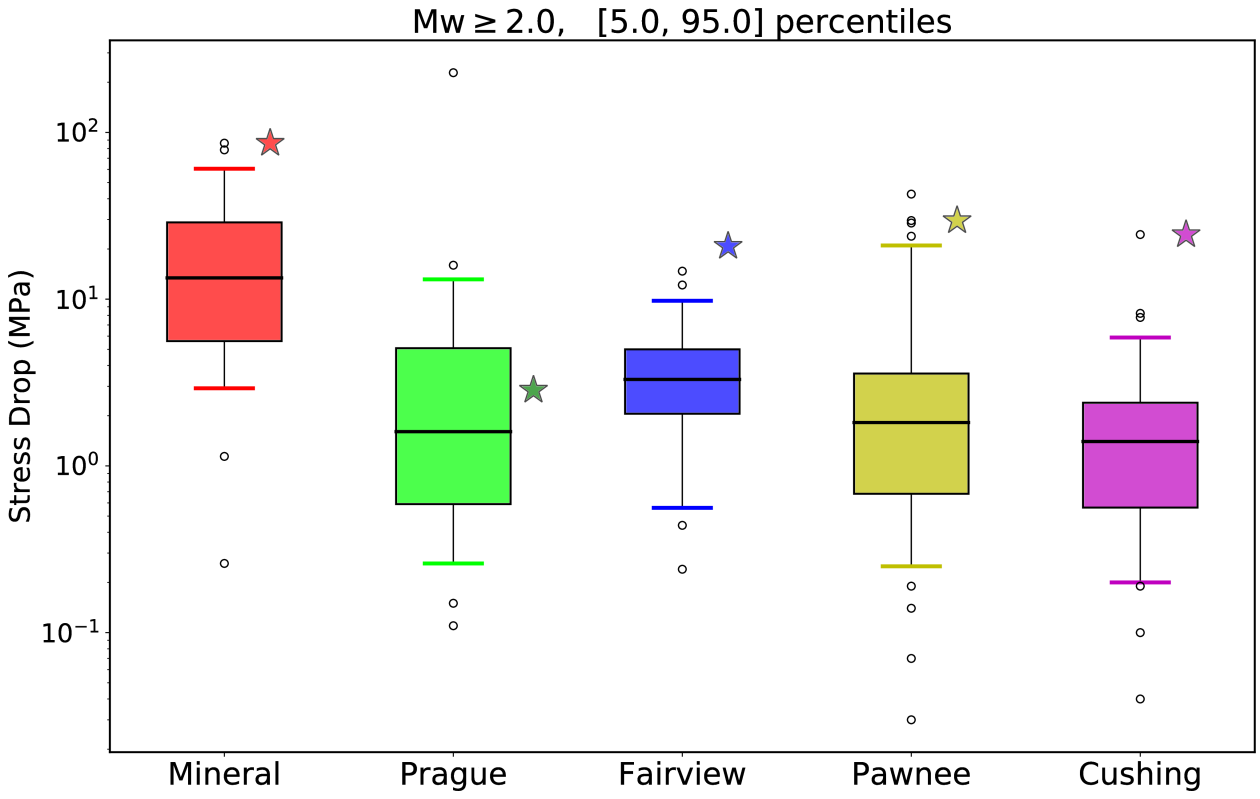

Figure 5.17: Boxplots summarizing the stress drop estimates for five earthquake sequences. The boxes show the 50 percentiles of the stress drop estimates around the median values (the black horizontal lines) for each sequence. The caps stand for 5-95 percentiles of the estimates. The mainshock stress drops are shown as stars.

stress drops of 201 events in four earthquake sequences in Oklahoma. We find that stress drop estimates span a wide range for individual sequences, with the mainshocks having high stress drops (20-30 MPa) except for the 2011 Prague mainshock, which has a much lower stress drop of 2.8 MPa. Compared to the other three sequences, the 2016 Fairview sequence exhibits more constant stress drop estimates, with a 2-3 times higher median stress drop. We observed that in all cases, the earthquakes appear to cluster spatially with high and low stress drops. Future examination of the spatial correlation between the stress drops and mainshock rupture slip patches and/or injection well data may help explain this observation.

References

Abercrombie, R. E. (2013). Comparison of direct and coda wave stress drop measurements for the Wells, Nevada, earthquake sequence, *J. Geophys. Res.* **118**, no. 4, 1458-1470.

Abercrombie, R. E. (2014). Stress drops of repeating earthquakes on the San Andreas Fault at Parkfield, *Geophys. Res. Lett.* **41**, 8784-8791, doi:10.1002/2014GL062079.

Aki, K. (1967). Scaling law of seismic spectrum, *J. Geophys. Res.* **72(4)**, 1217-1231, doi:10.1029/JZ072i004p01217.

Aki, K., and B. Chouet (1975). Origin of coda waves: Source, attenuation, and scattering effects, *J. Geophys. Res.* **80**, no. 23, 3322-3342.

Allmann, B. P., and P. M. Shearer (2009). Global variations of stress drop for moderate to large earthquakes, *J. Geophys. Res.* **114**, B01310, doi:10.1029/2008JB005821.

Atkinson, G. M. and D. M. Boore (2006). Earthquake ground motion prediction equations for eastern North America, *Bull. Seismol. Soc. Am.* **96**, 2181-2205.

Baltay, A., S. Ide, G. Prieto, and G. Beroza (2011). Variability in earthquake stress drop and apparent stress, *Geophys. Res. Lett.* **38**, L06303, doi: 10.1029/2011GL046698.

Beyreuther, M., Barsch, R., Krischer, L., Megies, T., Behr, Y., and J. Wassermann (2010). ObsPy: A Python toolbox for seismology, *Seismol. Res. Lett.* **81**, 530-533.

Boatwright, J. (1980). A spectral theory for circular seismic sources: simple estimates of source duration, dynamic stress drop, and radiated energy, *Bull. Seismol. Soc. Am.* **70**, 1-28.

Boatwright, J., and L. Seekins (2011). Regional spectral analysis of three moderate earthquakes in northeastern North America, *Bull. Seismol. Soc. Am.* **101**, 1769-1782.

Boore, D. M. (1983). Stochastic simulation of high-frequency ground motions based on seismological models of the radiated spectra, *Bull. Seismol. Soc. Am.* **73**, 1865-1894.

Boyd, O. S., D. E. McNamara, S. Hartzell, and G. Choy (2017). Comparison of earthquake stress drops in North America, *Bull. Seis. Soc. Am.* **107**, no.2, doi: 10.1785/0120160219

Brune, J. (1970). Tectonic stress and the spectra of seismic shear waves from earthquakes, *J. Geophys. Res.* **75(26)**, 4997-5009.

Brune, J. N. (1971). Correction, *J. Geophys. Res.* **76**, 5002.

Chen, X., and P. M. Shearer (2011). Comprehensive analysis of earthquake source spectra and swarms in the Salton Trough, California, *J. Geophys. Res.* **116**, doi:10.1029/2011JB008263.

Chen, X., P. M. Shearer, and R. E. Abercrombie (2012). Spatial migration of earthquakes within seismic clusters in Southern California: Evidence for fluid diffusion, *J. Geophys. Res.* **117**, B04301, doi:10.1029/2011JB008973.

Clerc, F., Harrington, R. M., Liu, Y., and Gu, Y. J. (2016). Stress drop estimates and hypocenter relocations of induced seismicity near Crooked Lake, Alberta. *Geophysical Research Letters*, **43**(13), 6942-6951.

Dahm, T., et al. (2013). Recommendation for the discrimination of human-related and natural seismicity, *J. Seismol.* **17(1)**, 197-202.

Davis, S. D., and C. Frohlich (1993). Did (or will) fluid injection cause earthquakes? Criteria for a rational assessment, *Seismol. Res. Lett.* **64**, 207-224.

Ellsworth, W.L. (2013), Injection-Induced Earthquakes, *Science*, **341**, 6142, `doi:10.1126/science.1225942`.

Eshelby, J. D. (1957). The determination of the elastic field of an ellipsoidal inclusion and related problems, *Proc. Roy. Soc. Lond.* **241**, 376-396, doi:10.1785/0120020217.

Frankel, A. (2015). Decay of S-wave amplitudes with distance from earthquakes in the Charlevoix, Quebec area: Effects of radiation pattern and directivity, *Bull Seismol. Soc. Am.* **105**, 850-857.

Frohlich, C., H. DeShon, B. Stump, C. Hayward, M. Hornbach, and J. I. Walter (2016). A historical review of induced earthquakes in Texas, *Seismol. Res. Lett.* **87**, no. 4, 1-17.

Garcia-Aristizabal, A., M. Caciagli, and J. Selva (2016). Considering uncertainties in the determination of earthquake source parameters from seismic spectra, *Geophys. J. Int.* **207**, 691-701.

Göbel, T. (2015). A comparison of seismicity rates and fluid injection operations in Oklahoma and California: Implications for crustal stresses, *The Leading Edge*, **34(6)**, 640-648.

Godano, M., P. Bernard, and P. Dublanchet (2015). Bayesian inversion of seismic spectral ratio for source scaling: Application to a persistent multiplet in the western Corinth rift, *J. Geophys. Res.* **120**, 7683-7712, doi:10.1002/2015JB012217.

Goebel, T. H. W., E. Hauksson, P. M. Shearer, and J. P. Ampuero (2015). Stress-drop heterogeneity within tectonically complex regions: a case study of San Gorgonio Pass, southern California, *Geophys. J. Int.* **202**, 514-528.

Goertz-Allmann, B. P., A. Goertz, and S. Wiemer (2011). Stress drop variations of induced earthquakes at the Basel geothermal site, *Geophys. Res. Lett.* **38**, L09308, `doi:10.1029/2011GL047498`.

Hanks, T., and H. Kanamori (1979). A moment magnitude scale, *J. Geophys. Res.* **84(B5)**, 2348-2350.

Hanks, T., and A. Johnston (1992). Common features of the excitation and propagation of strong ground motion for North American earthquakes, *Bull. Seismol. Soc. Am.* **82**, 1-23.

Herrmann, R.B. (2017). St. Louis University Earthquake Center website: `http://www.eas.slu.edu/eqc/eqc_mt/MECH.NA/` (last accessed March, 2017).

Horton, J. Wright, Jr., M.W. Carter, M.C. Chapman, Q. Wu, A.K. Shah, and A.C. Witt (2017). Studying the influence of rock units and joints on shallow aftershocks of the 2011 Mineral, Virginia earthquake, *Seism. Res. Lett.* **88**, p. 250.

Hough, S. E. (1996). Observational constraints on earthquake source scaling: understanding the limits in resolution, *Tectonophysics* **261**, 83-95.

Hough, S. E. (1997). Empirical Greens function analysis: taking the next step, *J. Geophys. Res.* **102**, 5369-5380.

Hough, S. E. (2014). Shaking from injection-induced earthquakes in the central and eastern United States, *Bull. Seismol. Soc. Am.* **104**, no. 5, 2619-2626.

Hough, S. E., and D. Dreger (1995). Source parameters of the 23 April 1992 M 6.1 Joshua Tree, California, earthquake and its aftershocks; empirical Greens function analysis of GEOS and TERRAscope data, *Bull. Seismol. Soc. Am.* **85**, 1576-1590.

Huang, Y., G. C. Beroza and W. L. Ellsworth (2016).Stress drop estimates of potentially induced earthquakes in the Guy-Greenbrier sequence, *J. Geophys. Res.* **121**, 6597-6607, doi:10.1002/2016JB013067.

Ide, S., and G. C. Beroza (2001), Does apparent stress vary with earthquake size?, *Geophys. Res. Lett.* **28(17)**, 3349-3352, doi:10.1029/2001GL013106.

Ide, S., G. C. Beroza, S. G. Prejean, and W. L. Ellsworth (2003). Apparent break in earthquake scaling due to path and site effects on deep borehole recordings, *J. Geophys. Res.* **108(B5)**, 13 pp., 2271, doi:10.1029/2001JB001617.

Imanishi, K., and W. L. Ellsworth (2006). Source scaling relationships of microearthquakes at Parkfield, CA, determined using the SAFOD Pilot Hole seismic array, in *Earthquakes: Radiated Energy and the Physics of Faulting*, R. Abercrombie, A. McGarr, G. D. Toro, and H. Kanamori (Editors), American Geophysical Union, Washington, D.C., 81-90.

Keranen, K. M, M. Weingarten, G. A. Abers, B. A. Bekins, and S. Ge (2014), Sharp increase since 2008 induced by massive wastewater injection, *Science* **345**, 6195, 448-451.

Madariaga, R. (1976). Dynamics of an expanding circular crack, *Bull. Seismol. Soc. Am.* **66**, 639-666.

Malagnini, L., and K. Mayeda (2008). High-stress strike-slip faults in the Apennines: An example from the 2002 San Giuliano earthquakes (southern Italy), *Geophys. Res. Lett.* **35**, L12302, doi 10.1029/2008GL034024.

Mayeda, K., L. Malagnini, and W. R.Walter (2007). A new spectral ratio method using narrow band coda envelopes: Evidence for nonself-similarity in the Hector Mine sequence, *Geophys. Res. Lett.* **34**, no. 11, 1-5.

McNamara, D. E., H. M. Benz, R. B. Herrmann, E. A. Bergman, P. Earle, A. Holland, R. Baldwin, and A. Gassner (2015). Earthquake hypocenters and focal mechanisms in central Oklahoma reveal a complex system of reactivated subsurface strike-slip faulting, *Geophys.*

Res. Lett. **42**, 2742-2749,

Oth, A., D. Bindi, S. Parolai, and D. Di Giacomo (2010). Earthquake scaling characteristics and the scale-(in)dependence of seismic energy-to-moment ratio: Insights from KiK-net data in Japan, *Geophys. Res. Lett.* **37**, L19304, doi 10.1029/2010GL044572.

Prieto, G. A., R. L. Parker, and F. L. Vernon (2009). A Fortran 90 library for multitaper spectrum analysis, *Comput. Geosci.* **35**, 1701-1710.

Rautian, T. G., and V. I. Khalturin (1978). The use of coda for determination of the earthquake source spectrum, *Bull. Seismol. Soc. Am.* **68**, 923-948.

Rubinstein, J., and A. Babaie Mahani (2015), Myths and facts on wastewater injection, hydraulic fracturing, enhanced oil recovery, and induced seismicity, *Seismol. Res. Lett.* **86**, doi: 10.1785/0220150067.

Salvatier J., T. V. Wiecki, and C. Fonnesbeck (2016). Probabilistic programming in Python using PyMC3, *PeerJ Computer Science* **2:e55** `https://doi.org/10.7717/peerj-cs.55`.

Sato, H., M. Fehler, and T. Maeda (2012). Phenomenological study of coda waves, in *Seismic Wave Propagation and Scattering in the Heterogeneous Earth*, Second Ed., Springer, Berlin/Heidelberg, Germany, 1-492, doi: 10.1007/978-3-642-23029-5_3.

Shaw, B. E., K. Richards-Dinger, and J. H. Dieterich (2015), Deterministic model of earthquake clustering shows reduced stress drops for nearby aftershocks, *Geophys. Res. Lett.* **42**, 9231-9238.

Somei, K., K. Asano, T. Iwata, and K. Miyakoshi (2014). Source scaling of inland crustal earthquake sequences in Japan using the S-wave coda spectral ratio method, *Pure Appl. Geophys.* **171**, no. 10, 2747-2766.

Sumy, D. F., C. J. Neighbors, E. S. Cochran, and K. M. Keranen (2017), Low stress drops observed for aftershocks of the 2011 MW 5.7 Prague, Oklahoma earthquake, *J. Geophys. Res.* **122**, doi:10.1002/2016JB013153.

Sumy, D. F., E. S. Cochran, K. M. Keranen, M. Wei, and G. A. Abers (2014). Observations of static Coulomb stress triggering of the November 2011 M5.7 Oklahoma earthquake sequence, *J. Geophys. Res.* **119**, doi:10.1002/2013JB010612.

Sun, X., and S. Hartzell (2014). Finite-fault slip model of the 2011 M W 5.6 Prague, Oklahoma earthquake from regional waveforms, *Geophys. Res. Lett.* **40**, 4207-4213.

Vidale, J.E., W.L. Ellsworth, A. Cole, and C. Marone (1994). Variations in rupture process with recurrence interval in a repeated small earthquake, *Nature* **368**, 624-626.

Walsh, F. R., and M. D. Zoback (2015). Oklahoma's recent earthquakes and saltwater disposal, *Sci. Adv.* **1**, e1500195, doi: 10.1126/sciadv.1500195.

Wells, D., J. A. Egan, D. G. Murphy and T. P. Paret (2015). Ground shaking and structural response of the Washington Monument during the 2011 Mineral, Virginia, earthquake, in *The 2011 Mineral, Virginia, Earthquake and its Significance for Seismic Hazards in Eastern North America*, Horton, J.W., Jr., Chapman, M.C., and Green, R.A., (Editors), Geological Society of America Special Paper 509, doi:10.1130/2015.2509(12), 199-234.

Wessel, P., W. H. F. Smith, R. Scharroo, J. F. Luis, and F. Wobbe (2013). Generic Mapping Tools: Improved version released, *Eos Trans. AGU* **94**, 409-410.

Wu, Q., M. C. Chapman, J. N. Beale and S. Shamsalsadati (2016). Near-source geometrical spreading in the central Virginia seismic zone determined from the aftershocks of the 2011 Mineral, Virginia, earthquake, *Bull. Seismol. Soc. Am.* **106**, 943-955.

Wu, Q., and M. C. Chapman (2017). Stress drop estimates and source scaling of the 2011 Mineral, Virginia mainshock and aftershocks, *Bull. Seismol. Soc. Am.* (in revision).

Yeck, W. L., M. Weingarten, H. M. Benz, D. E. Mcnamara, E. Bergman, R. B. Herrmann, J. Rubinstein, and P. S. Earle (2016). Far-field pressuri- zation likely caused one of the largest injection induced earthquakes by reactivating a large pre-existing basement fault structure, *Geophys. Res. Lett.* **43**, 10,19810,207.

Yoo, S.-H., J. Rhie, H.-S. Choi, and K. Mayeda (2010). Evidence for non-self-similarity and transitional increment of scaled energy in the 2005 west off Fukuoka seismic sequence, *J. Geophys. Res.* **115**, no. B08308, doi 10.1029/2009JB007169.

Zhang, H., D. Eaton, G. Li, Y. Liu, and R. M. Harrington (2016). Discriminating induced seismicity from natural earthquakes using moment tensors and source spectra, *J. Geophys. Res.* **121**, 972-993.